

Lead-Less Halide Perovskite Solar Cells

*Liam Gollino and Thierry Pauporté**

L. Gollino, Prof. T. Pauporté
Chimie-Paristech, PSL Université, CNRS, Institut de Recherche de Chimie-Paris (IRCP),
UMR8247, 11 rue Pierre et Marie Curie, F-75231 Paris cedex 05, France
E-mail: thierry.pauporte@chimie-paristech.fr
Website: www.pauportegroup.com

Keywords: lead-less, perovskite solar cell, toxicity, stability, d-HPs, hollow

Sol. RRL **2021**, *5*, 2000616 DOI: 10.1002/solr.202000616

Abstract

The rise and commercialization of perovskite solar cells (PSCs) is hindered by the toxicity of lead present in the perovskites employed as the solar light absorber. To counter this problem, Pb can be fully (lead-free) or partially (lead-less) replaced by diverse elements. The former compounds suffer from poor efficiency and poor stability while the later appear more promising. This review offers a survey of the methods reported in the literature to reduce Pb content in PSCs to fabricate "lead-less" (also called "lead-deficient") PSCs. We develop, first, the comparison of Sn and Pb elements and the partial replacement of Pb by Sn. Then, its substitution by either Ge, Sr or other alkaline-earth-metals, transition metals and elements from columns 12, 13 and 15 of the periodic table are detailed. The new families of perovskites based on the insertion of organic cations to replace lead and halogen units, namely the "lead-deficient" and "hollow" halide perovskites are then presented and discussed. Finally, atypical ways to reduce the toxicity of PSCs are presented: perovskite layer thickness reduction via optimization of photon collection, integration of photonic structures and employment of recycled lead. The present achievements and the outlook of those strategies are presented and discussed.

1. Introduction

During the last decade, hybrid halide perovskites (HPs) have attracted great attention from the scientific community worldwide for a large range of optoelectronic applications such as lasers ^[1], LEDs ^[2], photodetectors ^[3,4], scintillation ^[5] and photovoltaic solar cells ^[6–12]. For the latter, they have emerged as very promising substitutes or complements to silicon solar cells by integrating them in mono-junction or multi-junction devices. The first report on the use of hybrid halide perovskite was published in 2009 by Miyasaka et al. ^[13] and related the integration of dispersed perovskite nanocrystals into a mesoporous TiO₂ layer to produce an unstable dye-sensitized solar cell (DSSC) that achieved a maximum power conversion efficiency (PCE) of 3.8%. Since then, after the replacement of the liquid electrolyte by a solid-state hole transporting material (HTM) in 2012 ^[14–16], hybrid halide perovskites have been widely studied thanks to their semiconductor properties such as high absorption coefficient and large wavelength range ^[17], high charge carrier mobility ^[18], long charge carrier diffusion length ^[19] and narrow and tunable bandgap ^[20]. Emergence of solid-state perovskite-based solar cells using solid perovskite films and called perovskite solar cells (PSCs) started with different articles reporting PSCs using CsSnI₃ and MAPbI₃ perovskite absorber and achieving PCE above 10% ^[14–16]. Within a few years, PCE of PSCs have rapidly increased to reach a certified record of 25.5% in 2020 ^[21,22], achieving efficiency values comparable to those of commercially available silicon solar cells. To get such high efficiency, different Pb-based absorber thin films have been developed such as CsPbI₃, MAPbI₃, FAPbI₃ (MA=methylammonium FA=formamidinium) or compounds with mixed-cations and/or mixed-halides ^[23–28]. However, Pb-based perovskites face two main problems: a rather poor stability and high toxicity.

This article must be cited as:

L. Gollino, T. Pauporté, Lead-Less Halide Perovskite Solar Cells

Sol. RRL **2021**, *5*, 2000616 DOI: 10.1002/solr.202000616

WILEY-VCH

Concerning the stability, different strategies have been developed to overcome this problematic: device engineering, use of two-dimensional perovskites (2D or quasi-2D perovskites), of barrier layers, perovskite stabilization by multi-cation integration ^[29–31] and device encapsulation. On the other hand, the toxicity of lead seriously burdens the development, industrialization and large-scale production for PSCs. This toxicity presents risks not only for the human and animals health ^[32,33] with for example death of adenocarcinoma epithelial cells, dopaminergic neuroblastoma cells and murine primary hippocampal neurons ^[34] that can cause tumors etc. or else impact on children's nervous system ^[35] but, also, to the environment. Indeed, lead can spread easily in nature, in plants, in animals and be concentrated in the food chain ^[36] (**Figure S1**) ^[37]. For instance, J. Li et al. found that lead from halide perovskite would be more dangerous than other sources of lead contamination present in the soil. For those reasons, it becomes compulsory to totally eliminate or partially replace lead from PSCs with other less-toxic elements. However, substituting lead by another element remains uneasy and a major concern. It faces important limitations. The substitution element has to be a metal ion that can form a 3D perovskite structure. As a reminder, hybrid halide perovskite has the ABX₃ general formula, where A is an univalent organic/inorganic cation, B is an octahedrally coordinated bivalent metal ion and X is a monoanionic halide (generally Cl, Br or I) ^[27,28]. To be stable, halide as well as oxide perovskites need to respect a tolerance factor. The best-known is called the Goldschmidt tolerance factor (*t*) ^[38]. This parameter is based on geometrical considerations and is calculated using the ionic radius of each ions by the following equation:

$$t = \frac{r_A + r_B}{\sqrt{2}(r_B + r_X)} \quad (1)$$

An octahedral factor μ is also defined:

$$\mu = r_B / r_X \quad (2)$$

where r_A , r_B and r_X are the ionic radii of A, B and X ions, respectively. For hybrid halide perovskites, for $0.8 \leq t \leq 1$, and $0.44 < \mu < 0.90$ a cubic structure is expected. For $t < 0.8$, the perovskite has an orthorhombic structure and for $t > 1$, the structure is hexagonal or low-dimensional^[39]. This tolerance factor is still widely used nowadays even if it suffers from limitations and many exceptions^[40,41]. In 2019, Bartel et al. showed that the Goldschmidt factor distinguishes correctly only 74% of the materials and then they proposed a new tolerance factor T given by the following formula:

$$T = \frac{r_X}{r_B} - n_A \left(n_A - \frac{r_A/r_B}{\ln(r_A/r_B)} \right) \quad (3)$$

where n_A is the A cation's oxidation state. A perovskite structure is formed when $T < 4.18$ ^[42]. According to the authors this new tolerance factor can predict correctly 92% to 94% of the perovskite compounds. Nevertheless, considering only the perspective of ion radius faces certain limitations. Other factors must also be considered such as valence electrons and stable valence state(s) of the substituting element. Indeed, elements with the same number of valence electrons as Pb and stabilized valence state are more likely potential substituents than elements that do not meet these requirements. However, exceptions can still be observed such as Sb or Bi that has three valence electrons. The important point is that metal ions to fully replace lead in hybrid halide perovskite solar cells are restricted to a very few numbers of elements, especially tin (Sn). The large development of Sn-based lead-free PSCs until 2019 has been well-summarized in the recent review by Ke et al.^[43] It makes Sn first choice to develop lead-less PSCs. Other materials such as group 2, 13, 14 and 15 elements and transition-metal elements are also promising candidates for partial substitution of lead in PSCs^[44–48].

In PSCs, the perovskite layer is sandwiched between two selective contact layers. On one side, the electron transporting layer (ETL) collects and transports the photogenerated electrons and blocks the photogenerated holes^[11]. On the other side, the hole transporting layer

(HTL) collects and transports holes and blocks the transfer of electrons. Depending on the position of these two layers in the cell and on the structure of the ETL layer, one can distinguish three main PSC architectures that we will encounter throughout this review and which are presented in **Figure 1**: mesoscopic, normal planar and inverted planar PSCs.

Many great reviews have been published the last years on the lead-free PSCs, i.e. PSCs with zero lead within ^[49–53], sometimes with a section on lead-less PSCs ^[54–56], but, to the best of our knowledge, no extensive review dedicated to lead-less PSCs has been published yet.

In this review, we present the different strategies developed to fabricate lead-less PSCs of various architectures. We especially develop the progress made in the partial substitution of lead with other elements and provide an overview of the works on this field. Other emerging strategies include the use of organic cations to replace mixed lead and halide (iodide) units. The thinning of the HP layer and the integration of photonic structures to optimize the light harvesting is also promising. First, we introduce Sn-based PSCs before to pursue with the properties of the Sn-based lead-less PSCs and their recent development through the studies of additives, deposition method and charge transport layers. Secondly, we describe the development of Sr-based lead-less PSCs. We continue with the presentation of lead-less halide perovskite solar cells made by partially substituting lead by other elements belonging to the 2, 13, 14 and 15 groups of the periodic table, as well as transition elements (see Figure 2). Then, we depict the strategies aiming at stabilizing the perovskite structure by partially replacing lead and halide motifs by large organic molecules. Following this route, we explain the origin and nature of the recent family of the lead-deficient halide perovskites (d-HP). We develop their properties and achievements in devices. We subsequently unveil “Hollow” perovskites and we describe their applications in lead-less PSCs. We present then some other innovative approaches that could help to reduce lead content in PSCs and produce less-polluting PSCs

without impacting too strongly their performances. Finally, we give a short conclusion and an outlook for these various strategies.

2. Sn-Pb based lead-less PSCs

2.1. The replacement of lead by tin

Compared to lead-free PSCs, lead-less solar cells based on tin are rather recent. The first study of Sn-based hybrid halide perovskite was carried out in 1974 by Fischer et al. who made and characterized CsSnX_3 with X being Cl, Br and I [57]. Later, different groups pursued the investigation of those materials to determine their nature, even with dimension reduction [58] until it was verified that they are indeed semiconductors with self-p-type doping tendency caused by Sn^{2+} oxidation to Sn^{4+} [59–61]. In the 1990 decade, Mitzi conducted a lot of pioneering researches on Sn-based perovskites [62–64]. Sn-based hybrid halide compounds being well-defined; their first use in photovoltaic devices was done in 2012 by Chung et al.. The Sn-based perovskite was then employed as a HTL and absorbing material in an all-solid-state dye-sensitized solar cell (DSSC). The N719 dye was the main absorbing material and the cells achieved a high efficiency of 10.2% [14]. The same year, a Schottky solar cell based on CsSnI_3 thin film was prepared by Chen et al. and achieved an efficiency of 0.9%, limited by the unwanted self-p-doping of CsSnI_3 film and the series and shunt resistances [65]. One year later, Stoumpos et al. revealed that MASnI_3 and FASnI_3 perovskites could be good candidates as light absorber materials thanks to their electronic and optical properties such as carrier mobilities, tunable direct-bandgap, strong photoluminescence in the same way than their lead peers [18]. After this work, first reports on Sn-based PSCs were published, unveiling MASnI_3 and MASnIBr_2 devices reaching PCEs of 5.23% and 5.73% respectively [66]. At the same time, MASnI_3 -based PSC was achieved with an efficiency of 6.4% [67]. These first results led the scientific community to increase the research effort on this topic. Different approaches have

been then developed: perovskite layers deposited by methods such as dripping^[68], one-step method^[66,67], vapor-assisted method^[69–73], incorporation of additives such as SnF₂^[74–82] or dimensional reduction of the perovskite material^[83–87] leading now to efficiencies around 10%. Atypical structures have been also tested, for instance double perovskite structure such as Cs₂SnI₆^[60,88–90], CsAgBiBr₆^[91–93], RbGeSnI₃^[94] or Ag/Bi-based PSCs^[95,96] but those materials lead to lower efficiencies than classic Sn-based lead-free PSCs with PCE < 4%. According to the theoretical study by Mandadapu et al. published in 2017, MASnI₃ PSCs with a ZnO:Al/TiO₂/MASnI₃/ CuI/Au normal planar architecture have the potential to reach a theoretical maximum efficiency of 24.82%^[97], thus encouraging the community to overcome the current bottlenecks and to achieve higher efficiencies.

Recently, different groups reported Sn-based solar cells with an efficiency approaching 10%. Jokar et al. introduced guanidinium (GA⁺) in FASnI₃ perovskite^[98]. By introducing 20% of GA in a FASnI₃ perovskite and doping with 1% ethylenediammonium diiodide, their ITO/PEDOT:PSS/GA_{0.2}FA_{0.8}SnI₃/C₆₀/ Bathocuproine (BCP)/Ag solar cell achieved a PCE of 9.6%. The same year, Ran and co-workers published the addition of 3-phenyl-2-propen-1-amine (PPA), a large-volume amine (LVA), in FASnI₃ perovskite^[99]. 15% of PPA in FASnI₃ perovskite solution led, after deposition of the perovskite by a dripping method, to an enlarged grain size, a reduced trap states density, a preferential orientation, an efficient charge extraction and an enhanced stability. A PCE up to 9.61% was reached by ITO/PEDOT:PSS/FASnI₃ (PPA)/C₆₀/BCP/Ag devices that retained 92% and 60% of their initial PCE after 1440 h of storage in a N₂-filled glovebox and after 10h in air with a relative humidity of 60%, respectively. In 2020, Wu and his group described the effect of 2-cyano-3-[5-[4-(diphenylamino)phenyl]-2-thienyl]-propenoic acid (CDTA) on FASnI₃ perovskite film and solar cells^[100]. CDTA introduction in the perovskite precursor solution was proved to form a stable intermediate adduct and optimized the crystallization process that allowed the formation of a compact and

uniform perovskite film with a preferential orientation. A large increase in carrier lifetime and a retarded permeation of moisture into perovskite crystals were found with the addition of CDTA. These benefits contributed to an ITO/PEDOT:PSS/ FASnI₃/C₆₀/BCP/Ag solar cell with a PCE of 10.1% thanks to enhanced V_{OC} and FF. These devices retained 94% of their original PCE after a storage of 1000h in air with a relative humidity (RH) of 30%. This pretty high efficiency for a Sn-based solar cell, is not the current record. A paper published in March 2020 by Jiang et al. reported an ITO/PEDOT/PEA_{0.15}FA_{0.85}SnI₃/ICBA/BCP/Ag solar cell that achieved an astonishing efficiency of 12.4% with an extremely high V_{OC} of 0.94V via the use of indene-C₆₀ bisadduct (ICBA) as ETL, PEA insertion and NH₄SCN doping in FASnI₃ perovskite^[101]. The authors showed that ICBA suppresses the charge carrier accumulation at the perovskite/ETL interface caused by remote iodide doping. The shallower LUMO level of ICBA compared to PCBM reduced the interface carrier recombination. On the other hand, NH₄SCN doping of the perovskite contributes to the diminution of defect states density inside the bandgap and then to the diminution of recombination within the perovskite layer. Once the final solar cells encapsulated, they were stored inside a N₂-filled glovebox and retained 90% of their PCE after 4000h. This stability test is not a reliable indicator of the device stability due to both encapsulation and friendly storage environment provided by the glovebox^[102]. This report, with a lead-free PSC above 10% is very encouraging for the future of lead-free PSCs. However, the performances of Sn-based perovskite solar cells remain much lower than that of their Pb-based counterparts.

Aside from their lower efficiency, lead-free Sn-based PSCs suffer from severe intrinsically low stability^[79,103,104]. The main issue is the low redox potential of Sn²⁺. Indeed, after exposure to ambient air, Sn²⁺ tends to oxidize to Sn⁴⁺ very easily, a behavior which is accelerated by heating^[105]. This oxidation causes a progressive loss of opacity of the perovskite film and an absorbance reduction. It is also responsible for the low efficiency of the cells

causing a strong p-type doping leading to high dark-carrier concentration and photocarrier recombination.

Thanks to the limitations in lead-free Sn-based hybrid halide perovskite solar cells, lead-less Sn-Pb-based PSCs started to be investigated with the expectation of getting more stable and efficient devices. In the following sections, we discuss the theory of these materials as well as their properties and their progress through optimization of the deposition method (one-step method, two-step method, dripping method and vapor-assisted method), the incorporation of additives, and the study of different charge transport layers.

2.2. Fundamental properties and theory of Sn-Pb-based PSCs

Partial replacement of Pb by Sn in order to make lead-less PSCs influences the optoelectronic properties of the final device compared to pure Sn-based PSCs or Pb-based PSCs even if Sn and Pb belong to the same group 14 in the periodic table and then have similar chemical properties. The first study on the optoelectronic properties of Sn-Pb mixed hybrid halide perovskites was published by Ogomi and co-workers in 2014. They depicted the influence of Sn percentage on $\text{MAPb}_{1-x}\text{Sn}_x\text{I}_3$ optical properties and performances of the final device^[106]. By increasing the Sn content, the optical bandgap was decreased (from 1.51 eV for MAPbI_3 to 1.1 eV for MASnI_3) and the absorption onset was increased up to 1060 nm for 70% of Sn, corresponding to a 260 nm red shift compared to MAPbI_3 perovskite (Figure S2). By changing HTL for P3HT to match correctly the energy levels, an efficiency of 4.18% was achieved. The same year, Zuo et al. reported the effect of Sn^{2+} substitution on perovskite films deposited by solution-cast method onto PEDOT: PSS layer^[107]. The additions of 15% Sn in $\text{MAPb}_{1-x}\text{Sn}_x\text{X}$ was found to markedly increase the crystallinity of the perovskite film and to offer a dynamic morphological modulation allowing a 97% coverage of the perovskite film with excellent continuity and large crystal domains onto the PEDOT: PSS layer. It suppressed

the charge recombination centers and improved the charge transport. With this method, they achieved a promising efficiency of 10.1% with a J_{sc} as high as 19.5 mA/cm². In 2015, a theoretical study was carried out by Mosconi and co-workers on the electronic and optical properties of Sn-Pb lead-less PSCs ^[108]. This study showed that with a continuous increase of Sn percentage comes a continuous red-shift and an increase in optical absorption according to the Vegard's law along with an increase of energy level and transport properties, which are in good agreement with experimental studies ^[109]. Also, it was demonstrated that 50:50 at.% Sn:Pb compounds retain the best transport properties of each material (MAPbI₃ being predicted a better electron transporter and MASnI₃ a better hole transporter), thus allowing excellent balanced charge transport properties. MASn_{0.5}Pb_{0.5}I₃ should also be more resistant to oxidation. The Sn:Pb ratio is not the only parameter that affects the optical properties of lead-less perovskite solar cells, A cations also influence it, especially the perovskite bandgap. In 2017, Prasanna et al. revealed the possibility to tune the bandgap of Sn-Pb hybrid perovskite via A cations engineering ^[110]. Two competing mechanisms were unveiled. The first was the tilting of MX₆ octahedra when substituting FA cation by Cs, causing an increase of the bandgap. The second was the lattice contraction upon partial substitution of FA by Cs, leading to a progressive decrease of the band gap. The first occurred for Pb perovskite and the second for Sn perovskite. By controlling the A cation composition, the bandgap tuning of Sn-Pb lead-less PSCs was then possible (See Figure 3).

2D Sn-Pb lead-less PSCs properties were investigated as well. In 2016, Mao et al. reported the role of organic counterion by studying two different organic spacers: histammonium (HA) and benzylammonium (BZA) that formed (HA)Pb_{1-x}Sn_xI₄ and (BZA)₂Pb_{1-x}Sn_xI₄ perovskites, respectively ^[111]. Depending on the organic counterion employed, the systems exhibited varying band gaps trends due to the geometric distortion of the layers. BZA induces an important distortion in the system leading to lower bandgaps than pure Sn (between

1.82eV for $x=0.75$ to 1.89eV for $x=1$). On the other hand, HA induces small distortion and bandgap value for intermediate composition varying between pure Pb and pure Sn. Devices with (HA)Pb_{1-x}Sn_xI₄ were fabricated and the champion PCE was 1.13% with a high V_{OC} of 0.91V but J_{SC} lower than 3 mA/cm².

Recently, in 2020, Liu et al. reported the effects of halogen substitutions on the properties of MASn_{0.5}Pb_{0.5}I_{3-y}X_y (X=Br or Cl) perovskites based on density functional theory (DFT) [112]. They calculated that I⁻ substitution by Cl⁻ or Br⁻ enlarges the bandgap, with Cl⁻ having a greater impact compared to Br⁻. However, they also calculated that I⁻ substitution with Cl⁻ or Br⁻ decreases the carrier mobility and then the performance of the devices. Besides, the calculated spectra showed a blue-shift with Cl⁻ and Br⁻ substitution with a decreased absorption intensity with increasing y . By calculating O₂ and H₂O adsorption energies, they revealed that Br⁻ or Cl⁻ substitution do not change the stability of the perovskite in wet environment: O₂ will still adsorb preferentially on Sn and H₂O on Pb. Based on the above properties and results, Sn-Pb lead-less PSCs are good candidates to equalize classical Pb-based PSCs while reducing lead content in the meantime. Nevertheless, to do so, the main limiting factor is the large V_{OC} loss, calculated as:

$$V_{OC,loss} = E_g/q - V_{OC}, \quad (4)$$

where E_g and q are the optical bandgap of the perovskite and the elementary charge respectively. It is caused by high trap density of the perovskite layer and improper energy level matching between the different layers [113,114].

2.3. Deposition methods

Different techniques are commonly used for the deposition of hybrid halide films for perovskite solar cells. The main of them are one-step solution method, two-step solution method,

dripping/quenching method and vapor deposition method. Those techniques are employed for either lead-free PSCs or lead-less PSCs.

2.3.1. One-step method

The one-step method consists in dropping the perovskite precursor solution onto the substrate prior to spin-coat it and finally anneal the substrate to form the perovskite layer. Different parameters can be changed such as the solution and the substrate temperature.

In 2017, the fabrication of a $\text{MAPb}_{1-x}\text{Sn}_x$ film on a PEDOT:PSS/NiOx bilayer via a one-step combined to a hot casting method was reported^[115]. This method consisted in heating the precursor solution at 60°C, dropping it onto the substrate heated at 180°C, starting the spinning and finally annealing the perovskite layer at 100°C for 10 min (See Figure S3a). By this technique, large micron-sized grains with an excellent coverage were formed (See Figure S3b). After optimization of the Sn percentage, the devices achieved a PCE of 10% with a high V_{oc} of 0.767 V, approaching the prediction of their S-Q model thanks to the micron-sized grains. However, the stability was quite poor, the PCE being reduced by 10% - 9% in only 50 min (the storage condition was not precised).

2.3.2. Two-step method

In this technique, a $\text{PbI}_2/\text{SnI}_2$ solution is first spin-coated on the substrate and dried. Then, the solution containing the cation and halide, such as MAI, CsI etc, is dropped onto the previous layer. The classical annealing for the perovskite growth is finally performed.

In 2016, Li et al. published a paper explaining how to fabricate high-quality $\text{MASn}_{0.5}\text{Pb}_{0.5}\text{I}_3$ film perovskite films via a two-step a method onto a PEDOT:PSS layer to finally make an ITO/PEDOT:PSS/ $\text{MASn}_{0.5}\text{Pb}_{0.5}\text{I}_3/\text{C}_{60}/\text{BCP}/\text{Ag}$ device^[116]. It consisted in spinning the hot precursor solution right after its deposition and let it dry naturally for 1h inside a N_2 -filled

glovebox. After this, MAI in isopropanol solution was dropped onto the film which was then annealed to form the final perovskite film. With this technique, a compact film with low roughness (around 15 nm) and good coverage was formed compared to a $\text{MASn}_{0.5}\text{Pb}_{0.5}\text{I}_3$ layer made by one-step method. The cells showed up an average PCE of 12.3% with a champion cell reaching 13.6% with a very high mean J_{sc} of 24.9 mA/cm^2 . Regarding the stability, cells kept inside a N_2 -filled glovebox retained more than 90% of their initial PCE after 120h. The same year, Liu et al. reported the key role of dimethyl sulfoxide (DMSO) while fabricating $\text{MAPb}_{(1-x)}\text{Sn}_x\text{I}_3$ perovskite thin films via a two-step method ^[117]. They revealed that the natural evaporation after the spin-coating of the $\text{PbI}_2/\text{SnI}_2$ precursor solution is extremely important to form an amorphous mirror-like final layer. During this evaporation step (of 10 minutes in the article) the formation of $\text{PbI}_2/\text{SnI}_2 \cdot \text{DMSO}$ complexes occurs. Competition between SnI_2 and PbI_2 take place during this process due to the difference in activation energy, that of SnI_2 being the highest, it should govern the process. Once this evaporation is done, MAI in isopropanol is dropped as usual with this method. MAI having a better affinity with PbI_2 and SnI_2 than DMSO, the final compact $\text{MAPb}_{(1-x)}\text{Sn}_x\text{I}_3$ was formed with an excellent coverage. A schematic representation of the process is shown in Figure S4. By using FTO/PEDOT:PSS/ $\text{MAPb}_{0.75}\text{Sn}_{0.25}\text{I}_3$ /PCBM/BCP/Ag architecture, they achieved an average efficiency of 12.63% with a champion cell at 13.93%. The year after, Liang and co-workers fabricated an all-inorganic $\text{CsPb}_{0.9}\text{Sn}_{0.1}\text{IBr}_2$ -based perovskite solar cell ^[118] via a two-step deposition method. First, the precursor solution (PbBr_2 and SnBr_2 mixture) was spin-coated and dried. After this, the film was dipped in a methanol solution of CsI salt, rinsed with isopropanol and finally heated on a hotplate at 350°C. By using this solution-phase process, they achieved a high PCE of 11.33% and a very high V_{oc} of 1.26V explained by the excellent energy band positions and a correct bandgap of 1.76eV. Despite being a full inorganic perovskite-based device, the cells had a very good stability thanks to the use of a carbon electrode that allow the cells, once

encapsulated, to retain 100% of their initial efficiency after more than 3 months of storage at room temperature and for more than 2 weeks at 100°C. This is very promising for the future of all-inorganic perovskite-based devices which usually suffer from their lower efficiency and stability compared to their hybrid organic-inorganic peers even if for the lead-less applications, the substitutions ratio is quite low.

2.3.3. Dripping/Quenching method

This method consists in dropping an antisolvent during the spin-coating of the perovskite precursor solution to form the perovskite or a perovskite precursor structure. The antisolvent, when mixed with the solvent, reduces the precursor solubility and produce its precipitation. The film is then annealed to allow the grains growth and generate the final perovskite film.

In 2016, Liao and co-workers reported the fabrication of PSCs using $(\text{FASnI}_3)_{1-x}(\text{MAPbI}_3)_x$ absorber^[119]. They spin-coated the precursor solution constituted of FASnI_3 and MAPbI_3 mixed with different molar ratios and dripped diethyl ether during the spin-coating and annealed the perovskite thin films. With a $x=0.4$, they got a fully covering perovskite layer made of small grains but with an uniform distribution and with a low bandgap of 1.2eV. Using an ITO/PEDOT:PSS/ $(\text{FASnI}_3)_{0.6}(\text{MAPbI}_3)_{0.4}/\text{C}_{60}/\text{BCP}/\text{Ag}$ solar cell architecture, they reached a best efficiency of 15.08% with a high J_{SC} of 26.86 mA/cm², a V_{OC} of 0.795V and a fill factor (FF) of 70.6%. More recently, in 2018, Wang et al. compared a two-step method with a dripping method on different HTL in inverted devices for making high quality $\text{FA}_{0.7}\text{MA}_{0.3}\text{Pb}_{0.7}\text{Sn}_{0.3}\text{I}_3$ thin films^[120]. They first compared the grain size of the perovskite polycrystalline films. Onto a PEDOT:PSS layer, just by switching from the dripping method to the two-step one, the average grain size increased from 200nm to 300nm. However, by changing the HTL by poly[bis(4-phenyl) (2,4,6-trimethylphenyl)amine] (PTAA), large grains with 1µm diameter and vertically aligned grain boundaries were achieved. A better crystallinity of the perovskite films

was also found for this HTL. By measuring V_{OC} values under various light power densities (I), the authors calculated the ideality factor (n_{ID}) of each perovskite fabricated using the following equation:

$$qV_{OC} = E_g + n_{ID}kT \ln(I/I_0) \quad (5)$$

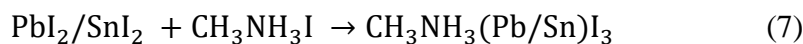
with q the elementary charge, k the Boltzmann constant, T the absolute temperature and I_0 a constant with the same unit as I . They always found that the two-step method gives a lower n_{ID} , indicating less Shockley-Read-Hall recombinations. A n_{ID} as low as 1.2 was obtained with PTAA, proving lower trap density and so better film quality in this case. Device scheme and associated J - V and external quantum efficiency (EQE) curves are shown in Figure S5. Devices made using a two-step method exhibited better performance than the one made with a dripping method. The former combined with PTAA HTM gave an efficiency of 13.6%. This device retains 80% of its original PCE after 30 days of storage in a N_2 -filled glovebox, which is a quite poor stability regarding the friendly storage environment employed. This study is one of the rare cases in which dripping method achieved lower efficiencies than the two-step one.

2.3.4. Vapor deposition methods

Vapor deposition is possible for perovskite materials due to their low melting point. The main advantages of the vapor deposition methods are their scalability and harmlessness for the underlying layers. Two techniques have been widely employed for vapor deposition: vapor-assisted method and thermal evaporation. They both allow the formation of compact, uniform and smooth films and can lead to devices with high efficiencies.

In 2016, Zhu et al. developed a vapor-assisted method using DMSO vapor during annealing to control the morphology of the Pb-Sn perovskite layer^[121]. As explained above in section 2.3.2, first, $MA\text{Sn}_x\text{Pb}_{1-x}\text{I}_3$ perovskite was deposited and then the substrates underwent a specific annealing treatment. It consisted in a first annealing for 1h at 100°C followed by a 1h long

second one at 100°C during which the substrate was covered by a glass petri dish. At the beginning of this second annealing treatment, a drop of DMSO was added onto the hotplate to create a DMSO saturated vapor atmosphere inside the petri dish and then realize the solvent vapor-assisted method. Figure 4 shows XRD measurement as well as SEM cross-sectional and top views of the $\text{MA}\text{Sn}_x\text{Pb}_{1-x}\text{I}_3$ films with and without DMSO vapor-assisted annealing. The XRD patterns showed no clear change so the DMSO-vapor method did not change the crystallinity of the perovskite film. However, it changed drastically the morphology as shown in Figure 4(A2) to 4(B5). The perovskite film had larger grains with no apparent surface defects (See Figure 4(A6) and 4(B6)), with no pinholes and some grains going through the entire thickness of the layer. These differences are due to the interaction between DMSO molecules and the Sn-Pb perovskite. The authors conjectured a preferential attachment of DMSO to Sn, leading to a breaking of Sn-I bonds, creating PbI_6^{4-} octahedra causing the rearrangement of Sn and Pb-centered octahedra and grains growth (See Figure 4C). They even suspected DMSO to act as a surfactant, promoting the grains formation with no surface defects. Using this technique, they achieved an average efficiency of 9.95% with a record cell reaching 10.25%, then improving the performance by more than 3% absolute compared to the classic annealing technique without DMSO. More recently, the fabrication of large-grains $\text{MAPb}_{1-x}\text{Sn}_x\text{I}_3$ perovskite solar cells using both thermal evaporation and chemical vapor deposition (CVD) techniques was reported^[122]. First, Pb/Sn materials were thermally evaporated on a TiO_2 -coated ITO glass. Then after, the substrates were transferred into a tubular CVD furnace in which MAI powder was spread so reaction between Sn-Pb and MAI occurred, and the perovskite film was formed. This process was shown to take place at 185°C. During this step, a yellow $(\text{Pb/Sn})\text{I}_2$ intermediate phase formed about 20 minutes before to react once again with MAI to produce the final $\text{CH}_3\text{NH}_3\text{Pb}_{1-x}\text{Sn}_x\text{I}_3$ perovskite film. The process is summarized by the following reactions:



Once the reactions were over, the perovskite layer surface was treated with isopropanol containing poly(4-vinylpyridine) (PVP) by spin-coating inside a N₂-filled glovebox to passivate the perovskite surface. With this unique method, high-quality films of Sn-Pb mixed perovskite with large grains over 5 μm were fabricated. It is important to note that mixed perovskite prepared by this method exhibited a better crystallinity than Pb-pure or Sn-pure perovskite. By changing the Sn-Pb mixture ratio, optoelectronic properties such as absorbance, photoluminescence and charge carrier lifetime were greatly affected like in conventional solution-based method. After optimization of the Pb:Sn ratio to 38:62 (wt%), the best cell exhibited an efficiency of 14.04% with a high J_{sc} and fill factor of 25.5 mA/cm² and 69.2% respectively. The reproducibility with this metal alloying technique was good and promising since the mean efficiency was 13.62%, a value comparable to the Pb-pure device. The light stability of the devices was tested, and the lead-less PSC retained 90% of its original PCE after 100 h of continuous illumination, an encouraging result for this technology. This year, Igual-Muñoz et al. developed a full evaporation process to fabricate Sn-Pb-based perovskite solar cells with an ITO/MoO₃/m-MTDATA/MA_{0.9}CS_{0.1}Sn_{0.25}Pb_{0.75}I₃/C₆₀/BCP/Ag architecture ^[123]. The perovskite layer was deposited via co-evaporation. A low champion PCE of 8.9% was obtained due important bulk recombination within the perovskite layer which resulted in low FF and V_{OC} (53% and 0.677V respectively). Even if the attained efficiency was low, it is still important to know that a solvent-free process for the preparation of Sn-Pb PSCs exist

2.4. Use of additives in Sn-Pb mixed PSCs

One of the main techniques to enhance the performances of solar cells is to employ additives in the precursor solution. Common additives are elements for halogen substitutions. In 2016, Tsai and co-workers reported the effect of tin chloride in $\text{MASn}_y\text{Pb}_{1-y}\text{I}_{3-x}\text{Cl}_x$ -based mesoscopic solar cells^[124]. They found that SnCl_2 participated in the crystallization of the perovskite at large concentration, modified the crystal structures by decreasing the symmetry and reduced the unit cell and also altered the optical and electronic properties. For example, they found anomalous evolution of bandgap and energy level with SnCl_2 incorporation. Consequently, the best energy level matching between the perovskite and charge transport layers was obtained for $y = 0.75$. After optimization with a SnF_2 doping that is a very common doping for Sn-based PSCs^[74–82] in order to suppress Sn oxidation and after the insertion of a NiO_x layer between the $\text{MASn}_{0.75}\text{Pb}_{0.25}\text{I}_{3-x}\text{Cl}_x$ film and the carbon electrode, the device achieved a champion PCE of 5.13%. Other halogen elements were tested such as bromide. In 2017, Lee et al. studied the effects of Br on $\text{MASn}_{0.6}\text{Pb}_{0.4}\text{I}_{(1-x)}\text{Br}_x$ morphology and performance of devices^[125] for a future integration in a full perovskite tandem cell. To foster slow crystallization and then get big grains, they chose a low annealing temperature of 80°C, which is lower than the one reported in other studies, typically 100–130°C^[116,120,126]. With the increase of Br content, they found an improved intensity of the XRD peaks without any additional peaks. It revealed an enhancement of the crystallinity and also the introduction of Br within the framework of perovskite, as found in classic MAPbI_3 perovskite^[127]. Br incorporation causes also a blue-shift of the absorption spectra. The bandgap of the perovskite increased from 1.24 eV to 1.32 eV for a Br content, x , varying from 0.2 to 0.8. These perovskites were tested in device and exhibited, for the perovskite with a Br content of 40%, a boosted efficiency of 12.1% which is a great improvement compared to the MAPbI_3 perovskite that achieved only 9.2% in this study. This upgrade is due to the remarkable increase of the V_{OC} and FF . Later, Li and co-workers studied

Br incorporation in $(\text{FASnI}_3)_{0.6}(\text{MAPbI}_3)_{0.4}$ in order to reduce the saturation current by passivating the grain boundaries (GB) ^[128]. The open-circuit voltage can be described by the diode equation (5) ^[129]. Based on this equation, it is clear that by decreasing J_0 , that can be done by reducing the dark charge carrier recombination in the cell, the V_{OC} , and then the overall efficiency of the cell, can be greatly enhanced. However, the major part of recombinations in the cell occurs at the grain boundaries. Li et al. found that by incorporating 6% of bromide, then forming $(\text{FASnI}_3)_{0.6}(\text{MAPbI}_3)_{0.34}(\text{MAPbBr}_3)_{0.06}$ perovskite, the J_0 was lowered by 4 orders of magnitude, passing from 10^{-5} to 10^{-9} mA.cm⁻² and reflecting an efficient grain boundary passivation with Br addition. An enhancement in crystallinity and grain size was also found with Br addition. Nevertheless, Br addition affects hole concentration and mobility with a clear decrease in concentration with increasing Br content and an increase in mobility with an increasing Br content. Photovoltaic performances of ITO/PEDOT:PSS/ $(\text{FASnI}_3)_{0.6}(\text{MAPbI}_3)_{0.4-x}(\text{MAPbBr}_3)_x/\text{C}_{60}/\text{BCP}/\text{Ag}$ solar cells are shown in Figure S6 with different Br concentrations. By looking at Figure S6a and Figure S6f, grain boundaries effective passivation with Br can clearly be seen, with a maximum at 6% Br percentage. At this concentration, a PCE of 19.03% was reached with a high V_{OC} and FF of 0.888V and 74.6% respectively which is a considerable raise of the efficiency compared to the pristine cell which achieved a PCE of 17.03%.

Halogen elements are not the only ones able to positively impact Sn-based lead-less perovskite solar cells. In 2017, Liu et al. detailed the use of C_{60} to assist the crystallization of $\text{MAPb}_{0.75}\text{Sn}_{0.25}\text{I}_3$ perovskite film during a two-step method deposition ^[130]. They revealed that by incorporating C_{60} in $\text{PbI}_2/\text{SnI}_2$ precursor solution, C_{60} wrapped itself around DMSO molecules due to the binding energy between both and then created a solvent shell, tuning the crystallization process and leading to thin films with a decreased pinholes density. After evaporation of the solvent during the annealing step, C_{60} molecules moved to the grain

boundaries with a uniform distribution and passivated them. As a result of this passivation, the final devices had higher bulk and surface recombination lifetimes and a decreased charge trap-state density. Once the C₆₀ additive concentration was optimized at 0.05 mg/mL, solar cells achieved a mean efficiency of 13.7% with enhanced J_{SC} and FF owed to improved crystallization while the V_{OC} was slightly decreased due to the deeper HOMO level caused by C₆₀ introduction. These devices exhibited quite good stability with 100% of their initial PCE retained after 7 days of storage in ambient environment with a relative humidity (RH) of 30-50% and a temperature between 20-25°C. It was assigned to the low solubility of C₆₀ in water and its resistance to oxidation at room temperature, preserving the grain boundaries and then the overall device. The same year, Xu et al. studied the effect of ascorbic acid incorporation in MASn_{0.5}Pb_{0.5}I₃ compared to SnF₂ [131]. Ascorbic acid was added to the precursor solution and found to retard Sn oxidation while modulating the perovskite crystallization by forming a complex. Using 10 mol% of ascorbic acid, the photogenerated carrier lifetime in the perovskite was increased, leading to a max efficiency of the final device of 14.01% with increased J_{SC} , V_{OC} and FF . As said above, ascorbic acid delays Sn oxidation, allowing a better stability for the device with 99% of the initial PCE value retained after 1-month long storage in a N₂-filled glovebox. As a comparison, with SnF₂ additive, only 63% of the initial PCE was retained.

Another well-known additive in perovskite solar cell field is thiocyanate (SCN). Many papers have reported bigger grains and improved film morphology with the introduction of SCN in lead-less [132] or pure-Pb based PSCs [133,134]. Recently, Lian et al. reported the introduction of methylammonium thiocyanate (MASCN) as a bifunctional additive to produce high-quality FAPb_{0.7}Sn_{0.3}I₃ film via a two-step method [135]. By introducing the optimized amount of MASCN (0.25), perovskite films with larger grains, high crystallinity and low trap-density were made by suppressing the crystallization of metal iodide film thanks to the strong coordination between SCN⁻ and metal iodide leading to a better charge transport and decreased non-radiative

recombination. MASCN was also found to prevent oxidation of Sn, then providing a way to stabilize the precursor solution (it is stable for 120 days) and for solar cells treated with it. These devices exhibited an average PCE of 15.81% and a champion PCE of 16.26% with enhanced J_{SC} and FF of 26.46 mA/cm² and 79% respectively, synonym of an increased of J_{SC} and FF of 2.96 mA/cm² and 6%, respectively. Owing to the prevented oxidation of Sn, MASCN-treated devices retained 100% of their performances after 30 days of storage in a N₂-filled glovebox but retained only 40% of their initial PCE after 14 days in air with a RH=25%, which is, even if better than devices without MASCN, a quite poor stability. Tong et al. studied the impact of guanidinium thiocyanate (GuaSCN) addition in (FASnI₃)_{0.6}(MAPbI₃)_{0.4} to realize high-efficiency cells to integrate it in an all-perovskite tandem solar cell ^[136]. GuaSCN was directly added to the perovskite precursor solution. This solution was spin-coated at 5000 rpm for 30s with a dripping of toluene onto the spinning substrates. It was demonstrated that GuaSCN, with an optimized content of 7%, improves the film morphology by forming bigger grains, reducing pinholes density, making more compact layers (See Figure S7a and Figure S7b), reducing defect states in bulk, surface of grains and grain boundaries. Figure S7c shows a high-resolution transmission electron microscope (HRTEM) image of GB with 7% GuaSCN addition. A 2D structure created by the addition of GuaSCN can be seen and is confirmed by the time-of-flight secondary ion mass spectroscopy (TOF-SIMS) tomography presented in Figure S7, revealing that GuaSCN tends to segregate to GB. Such 2D structure passivates the GB with its wider bandgap, blocks diffusion of Sn out of grains, suppresses the formation of excessive Sn vacancies and reduces oxygen diffusion into grains. All of this allowed a stunning enhancement of the carrier lifetime from 139 ns for the pristine devices to 1232 ns for devices with GuaSCN, the carrier lifetime was increased by about 10 times due to GuaSCN addition. A high charge diffusion length of 2.5 μm was also achieved. The resulting (FASnI₃)_{0.6}(MAPbI₃)_{0.4} films

enabled the inverted solar cells to achieve a PCE up to 20.2% with J_{SC} , V_{OC} and FF equal to 30.5 mA/cm², 0.83V and 80%, respectively.

In 2020, a new record of 20.63% was achieved by Zhou and co-workers by using guanidinium bromide (GABr) additive ^[137]. By leading XRD measurements, the authors found a slight shift of the reflection peaks at low angle, synonym of an expansion of the unit cell volume, proving the introduction of GABr within the lattice. At a precise concentration of GABr, they found an increased grain size, higher charge carrier concentrations and reduced trap state densities. It was also proved that GABr plays a role in defect passivation, thus reducing the V_{OC} deficit to 0.33V which is a record for Sn-Pb based PSCs. Photovoltaic performances and stability measurements of solar cells based on ITO/EMIC-PEDOT:PSS (PEDOT:PSS solution with 1.5 wt% EMIC [1-ethyl-3-methylimidazolium chloride])/FA_{0.7}MA_{0.3}Pb_{0.7}Sn_{0.3}I₃/C₆₀/BCP/Ag are detailed in Figure 5. It is important to precise here that the perovskite layer containing GABr dopant was made by a dripping method using chlorobenzene and that after the annealing, S-acetylthiocholine in isopropanol was spin-coated on top of it. All the photovoltaic parameters skyrocketed with the use of 12% GABr dopant, leading to an efficiency up to 20.63% with good reproducibility and an extremely high $V_{OC} > 1V$ that is to compare to the 16.71% achieved without GABr. The certified PCE attained 19.8%. Furthermore, the environmental and thermal stabilities were largely improved with the introduction of GABr in PSCs: 85% of the initial PCE was retained after 1000h in air with relative humidity around 50-60% and 90% of the initial PCE after 24h in air at 80°C. This study offers a great hope for the future of Sn-Pb based PSCs showing that they can deliver a high efficiency with good stability.

2.5. Influence of the charge transport layers (CTL)

As said above in section 2.2, mismatching between the energy levels of CTLs and perovskite layers can cause large V_{OC} deficit and a decrease in the efficiencies of the

photovoltaic devices. The interface between these layers is also a crucial point. Different factors highly depend on it, such as density of recombination centres, charge transport mobilities and extraction, perovskite crystallization and growth if the studied layer is the one above the perovskite film etc. It is then vital to understand the effect of each material usable as electron transport layer (ETL) or hole transport layer (HTL) to have a final optimized solar cell.

2.5.1. ETL

The ETL, is an important component of classical lead-PSCs^[11]. For the direct structure, TiO₂ is the most popular one^[12,138] along with the SnO₂ one^[139]. Sn-Pb lead-less PSCs are usually fabricated in an inverted structure (See Figure 1) as it can be seen in Table 1. Therefore, ETL is not as studied as perovskite layer engineering and HTLs since it does not influence directly the perovskite growth and thus the possibility to achieve higher PCE just by doing ETL engineering is rather low. However, some groups have obtained interesting results by working on this device component. In 2018, Kapil and co-workers realized a perovskite solar cell with a spike structure, i.e. a conduction band offset (CBO) between the perovskite layer and the ETL by inserting an intermediate layer, in order to achieve higher efficiency through a higher V_{OC} ^[140]. Such a structure was already used in Cu(In,Ga)Se₂ (CIGS)-based solar cells^[141,142] and was theoretically proved to work in PSCs in 2015 by Minemoto^[143] et al. and applied by others^[144]. Here, they inserted a thin PCBM layer (5 mg/mL in o-dichlorobenzene) between the FA_{0.5}MA_{0.5}Sn_{0.5}Pb_{0.5}I₃ layer and the C₆₀ layer that led to a CBO of 0.15 eV and resulted in an enlargement of the V_{OC} from 0.67V to 0.75 V for an overall efficiency of 17.59% (compared to 14.18% for solar cells without PCBM layer). More recently, Liu et al. developed a method to reduce the V_{OC} loss by introducing a zinc oxide (ZnO) layer by spin-coating between the PCBM ETL and the Ag electrode to suppress silver diffusion^[114]. Scanning transmission electron

microscope (STEM) and energy dispersive spectrometer (EDS) images of Figure 6 proved the suppression of Ag diffusion within the perovskite layer. No trace of silver was found in the perovskite layer with the insertion of ZnO, preventing silver ions to degrade the perovskite layer and to reduce the efficiency of the solar cell. The authors found a reduced trap density value for the film without Ag diffusion as well as a faster charge extraction since Ag diffusion caused a downshift of the conduction band (CB) of the perovskite, hindering electron transfer. All these benefits conducted to a boost of 0.2 V in V_{OC} and 14.7% in FF, leading to a champion efficiency of 18.1%, which is to compare to the 11% PCE achieved without ZnO. A slight improvement of the stability was also obtained with the ZnO interlayer, but the devices were still highly unstable as 20% of the initial PCE was lost after only 30 days of storage inside a N_2 -filled glovebox.

2.5.2. HTL

The hole transporting layer (HTL) is very important in PSCs for hole extraction and transport as well as for the blocking of electrons^[145–148]. This layer has attracted most attention from the community of lead-less PSCs since it does not only affect the charge extraction but it also affects the perovskite crystallization and thus the perovskite optoelectronic properties since it is usually the bottom layer due to the inverted structure employed to fabricate Sn-Pb lead-less PSCs (Figure 1). The common HTL present in Sn-Pb PSCs with inverted structure is PEDOT:PSS^[116,120,128] but, due to its strong acidity, it degrades the anode interface^[149]. Also, its work function (~5.1 eV) does not match perfectly with the valence band of the Sn-Pb perovskites, causing a diminution of the V_{OC} of the device. These intrinsic problems of PEDOT:PSS could be reduced with the use of additives such as EMIC (see section 2.4) that allowed Zhou et al. to achieve the record efficiency of 20.63%^[137]. Indeed, EMIC was proved

to effectively reduce the charge trap density, to extend the charge carrier recombination lifetime, to increase the electrical conductivity and to lower the work function of PEDOT:PSS layer ^[150]. Instead of using additives to improve PEDOT:PSS, other groups replaced it by other materials. In 2018, Shao and co-workers reported the use of PCP-Na, a neutral pH anionic conjugated polymer with alkylsulfonate side group as HTM which was deposited by spin-coating ^[151]. Numbers of interesting beneficial properties were found: (i) a slightly higher electrical conductivity and higher crystallinity than PEDOT:PSS, allowing a better charge extraction. (ii) A higher transparency in the 420-530nm range, reducing the photon loss for the perovskite layer. (iii) A pinhole free perovskite film on top of PCP-Na layer leading to a lower leakage current, a better built-in potential and a decreased interfacial and bulk recombination. These advantages conducted to an enhancement of V_{OC} and J_{SC} of 0.3V and 2 mA/cm², respectively, and to achieve a PCE up to 16.27%. In 2020, Song et al. developed a CuI/PEDOT:PSS double hole-transporting layer for (FASnI₃)_{0.6}(MAPbI₃)_{0.4}-based PSCs ^[152]. The authors revealed a faster charge extraction and more efficient charge transport with the double HTL than with PEDOT:PSS and CuI layers alone. It was assigned to the cascading energy alignment together with the high charge mobility of CuI. PEDOT:PSS/CuI double HTL was less interesting due to the roughness of the CuI layer causing a bad interface contact with the perovskite layer. On the other hand, PEDOT:PSS surface was smooth, ensuring a good HTL/perovskite interface contact and reduced charge recombination. Different CuI concentrations were tested, synonym of different CuI layer thickness, to finally form an optimized layer with a concentration of 10 mg/mL. The complete solar cell based on ITO/CuI/PEDOT:PSS/(FASnI₃)_{0.6}(MAPbI₃)_{0.4}/C₆₀/BCP/Cu architecture achieved a PCE up to 15.75% with enhanced J_{SC} and FF and maintained to 95% of its initial value after 600h of storage inside a N₂-filled glovebox, which is good but not representative of the stability of the device in a “realistic” environment. The same year, Hamada and co-workers reported the

passivation of the TiO₂ HTL surface by a carboxylic acid fullerene monolayer in a normal architecture^[153]. This report is one of the very rare study on Sn-Pb lead-less PSCs with a normal device structure due to their lower efficiency compared to the one based on an inverted structure. The authors unveil the reason behind this inferior performance using an FTO/c-TiO₂/m-TiO₂/MASn_{0.3}Pb_{0.7}I₃ /spiro-OMeTAD/Au solar cell architecture (c-TiO₂ and m-TiO₂ being compact and mesoporous TiO₂ layers, respectively). They reported that in classical Pb-based PSCs, PbI₂ is adsorbed on the surface of porous TiO₂, leading to Ti-O-Pb bonds that passivated TiO₂ surface and reduced the surface traps which is beneficial. However, in Sn-based and Sn-Pb based PSCs, SnI₂ is adsorbed on the TiO₂ surface forming Ti-O-Sn bonds and passivating TiO₂ surface. This passivation, contrary to the PbI₂ passivation, is detrimental to the device as it increases trap density. Effects of both passivations on photovoltaic parameters are shown in Figure S8. The drastic drop of efficiency caused by the SnI₂ passivation can clearly be seen, thus explaining the low efficiencies obtained for Sn-Pb PSCs with normal architecture and pointing the need for a buffer/passivation layer between TiO₂ and Sn-Pb perovskite. To overcome this problem, the authors inserted a C₆₀-COOH fullerene layer between the TiO₂ and MASn_{0.3}Pb_{0.7}I₃ perovskite layer by dripping the substrates covered with porous TiO₂ with the C₆₀-COOH solution in a N₂-filled glovebox. By doing so, the efficiency of the solar cells increased from 5.14% to 7.92% with an increase of all the photovoltaic parameters (J_{sc}, V_{oc} and FF).

A summary of the results obtained in the literature for Sn-Pb PSCs as a function of Sn at.% is provided in Table 1. From the above discussion, Sn-Pb lead-less PSCs seem very promising for the more environment-friendly perovskites with a recent record efficiency as high as 20.63%. However, it is obvious that these devices are still too air-sensitive and that their degradation is still too fast to be a reliable solution for the future. Even if good progress has been made on this subject, more studies should be implemented to boost the stability of this system.

3. Sr-Pb based lead-less PSCs

Sr is an alkaline-earth-metal belonging to group 2. In 2016, Pazoki et al. studied, via DFT calculations, the possibility for alkaline-earth elements to form a perovskite structure ^[154]. They indicated the potential for these materials to form such a structure and then their potential use in PSCs. In the case of strontium, the ionic radius of Sr²⁺ is very close to Pb²⁺ at 132 pm and 133 pm respectively, and its orbital symmetry allows the same coordination to iodide as Pb²⁺ ^[155]. However, due to their inappropriate bandgap (3.6 eV for MASrI₃), alkaline-earth-metal-based lead-free PSCs are not good candidates as light absorber but more as electron/hole transport materials. On the other hand, the partial substitution of Pb by an alkaline-earth-metal in order to fabricate lead-less PSCs appears as an attractive approach. The most appealing and studied of these elements is Sr.

One of the first report studying Sr substitution in PSCs was published by Kai et al. in 2015 ^[156]. They synthesized a MASr_xPb_{1-x}I₃ perovskite film via a one-step method for an FTO/c-TiO₂/m-TiO₂/MASr_xPb_{1-x}I₃/Spiro-OMeTAD/Ag solar cell. The authors showed that the introduction of Sr resulted in a loss of 71.5% of the original PCE for a 10% Pb substitution. In 2017, Lau and co-workers developed a low-temperature process at 100°C to fabricate CsPb_{1-x}Sr_xI₂Br PSCs via a vapor-assisted deposition method ^[157]. With Sr incorporation, the morphology of the perovskite film was drastically changed. Indeed, for CsPbI₂Br perovskite, the film was composed of densely packed small grains (due to the lower temperature of the process), but with Sr incorporation, the perovskite film was composed of “snowflakes” like structures with smoother and Sr-enriched surfaces (See Figure S9). Sr-substitution was found to enhance the absorption without affecting the absorption onset as long as the Sr percentage was lower than 5%. For Sr percentage being 1 or 2%, a passivation effect was proved leading to a better effective recombination lifetime of the charge carrier. FTO/m-TiO₂/c-

This article must be cited as:

L. Gollino, T. Pauporté, Lead-Less Halide Perovskite Solar Cells
Sol. RRL **2021**, *5*, 2000616 DOI: 10.1002/solr.202000616

WILEY-VCH

TiO₂/CsPb_{0.98}Sr_{0.02}I₂Br/P3HT/Au solar cells achieved a PCE up to 11.2%, corresponding to an increase of 45% compared to CsPbI₂Br-based solar cells with increased J_{SC} , V_{OC} and FF . Encapsulated devices were kept in the dark at 25°C and with a RH<50% and an increase of efficiency was found after 1 week due to P3HT oxidation. After that, the devices remained stable. This stability test is not very demanding in view of the rather short duration time, the friendly environment and the encapsulation. The same year, Shai et al. achieved ITO/c-TiO₂/m-TiO₂/MASr_{0.05}Pb_{0.95}I_{3-x}Cl_x/spiro-OMeTAD/Au solar cells with a high efficiency of 16.3% [45]. By incorporating 5 mol% Sr, an up-shifting of the perovskite conduction band edge energy level was found, that led to an enhanced output voltage; an enhanced exciton binding energy and trap density states, reducing ultimately the J_{SC} of the final devices. Regarding the morphology of the perovskite film, smaller grains with a more compact morphology were observed with Sr incorporation compared to the original pure-Pb perovskite. All these properties led to a device with a PCE of 16.3%, slightly lower than the 16.7% achieved for the pure-Pb PSCs due to a decreased J_{SC} but with a higher V_{OC} of 1.11 V (compared to 1.07V). The authors also proved an enhanced air and thermal stability, but these ones were still low: only 70% of the initial PCE was retained for the encapsulated devices after 120h in a baking box at 80°C and a loss of 5% of the original PCE was observed after only 140h in a N₂-filled glovebox for unencapsulated devices. In 2018, Wu et al. studied the partial replacement of lead in PSCs by different alkaline earth metals [158]. Most experiments were conducted on Ba substitution, but they also studied different Sr doping percentages in FTO/TiO₂/MAPb_{1-x}Sr_xI₃/spiro-OMeTAD/Ag solar cells. Average efficiencies of 10.6%, 6.5%, 4.3% and 1.1% were achieved for x equal 0.01, 0.02, 0.05 and 0.1 respectively, all lower than Pb-based devices. In the meantime, Zhang and co-workers developed lead-less mesoscopic PSCs with enhanced performance by SrCl₂ substitution [159]. Consistently with reports above, reduced grain size with increasing Sr percentage was proved by the authors. Also, a reduction of the excess of PbI₂ in

the perovskite film with Sr incorporation was observed, synonym of a complete reaction of the perovskite with Sr substitution. An optimized content of Sr of 10% was determined, allowing (i) a better absorbance and electron extraction, leading to an enhanced J_{SC} of 19.45 mA/cm² compared to 17.41 mA/cm² for pristine perovskite; (ii) a reduced charge recombination and then an increased V_{OC} and FF (from 1.04V to 1.08V and 72% to 74% respectively). The cells based on FTO/c-TiO₂/m-TiO₂/MAPb_{0.9}Sr_{0.1}I_{2.9}Cl_{0.1}/spiro-OMeTAD/Au architecture achieved a champion PCE of 15.64%, which is an enhancement of 2.49% absolute compared to pure-Pb PSCs. The same year, Zhang et al. reported the effect of SrI₂ substitution on MAPb_{1-x}Sn_xI₃ perovskite formation via dripping and two-step methods in an FTO/c-TiO₂/m-TiO₂/MAPb_{1-x}Sn_xI₃/spiro-OMeTAD/ Au solar cell architecture ^[160]. For the dripping method, the authors tested Sr substitution up to 5 mol%. They revealed a decrease of the perovskite film coverage, an increased pinhole density and defect density with a drastic deterioration of the film with Sr percentage superior to 2%. However, Sr substitution did not change the crystal lattice but improved the crystallinity of the perovskite. For Sr substitution from 1% to 5%, lower efficiencies than pure Pb-based PSCs were achieved with an important decrease for Sr > 2%, which reflected the poor film coverage. For the two-step method, Sr amount from 0 to 20% were tested. Sr percentage was found to strongly impact the perovskite morphology with this deposition method. Dendritic, rods and uniform structures were obtained for Sr amount of 5%, 10-15% and 20% respectively. Contrary to the dripping method, no difference in coverage was observed but smaller grains were obtained. With an optimized substitution level of 10%, defect density and non-radiative recombination were reduced, allowing enhanced V_{OC} and FF , leading to a PCE up to 15.52% instead of 13.57% for the pristine solar cell. In 2020, Li and co-workers developed a specific ETL by fabricating an original TiO₂ nanorod array (TNRA) for high efficiency Sr-Pb lead-less PSCs ^[161]. A similar TNRA was already used in the past by Zhang et al. in 2015 ^[162]. This nanorod array was made by a hydrothermal method, consisting in plunging

This article must be cited as:

L. Gollino, T. Pauporté, Lead-Less Halide Perovskite Solar Cells
Sol. RRL **2021**, *5*, 2000616 DOI: 10.1002/solr.202000616

WILEY-VCH

TiO₂ seed crystals-coated substrates in a mixture of HCl, distilled water and titanium butoxide, placed at 180°C for 80 min, then rinsing with clean water and finally annealing 30 minutes at 500°C. Thanks to its high specific surface area (see Figure 7), the nanorod array ETL provided a direct electron transport channel in the devices. With substitution of PbI₂ by 5 mol.% SrCl₂, recombinations were effectively suppressed and charge transport from the perovskite to the TNRA ETL was facilitated. With these original ETL, PCEs up to 16.08% and 15.09% were achieved for Sr substitution of 5% and 15%, respectively, with encouraging improved air and thermal stability: no loss of PCE was noted after 18 days for unencapsulated devices stored at 20°C in 30% RH. Regarding thermal stability, thermal cycle consisting in 2h of heating at 85°C followed by 1h at room temperature under 15% RH were made and 98.8% of the initial PCE was retained after 16 cycles. Also in 2020, Zhang et al. published a detailed report of the effect of Sr substitution on the humidity and thermal stability of the FTO/c-TiO₂/m-TiO₂/MAPb_{1-x}Sr_xI_{3-y}Cl_y/spiro-OMeTD/Au perovskite solar cells [163]. Lead substitution by 10% SrI₂ and SrCl₂ were studied, the devices being named SI10 and SC10, respectively. For the humidity stability, different storage conditions were tested: 20°C with 5, 30 and 50% RH. On one hand, SI10 devices were found the most sensitive to water as they formed hydrates at grain boundaries that increased series resistance (R_s) and diminished recombination resistance (R_{rec}). On the other hand, SC10 exhibited very good humidity stability with only a slight deterioration in resistances and performances over 21 days due to passivation of grain boundaries by SrCl₂. For both substitutions, the decomposition rate of the perovskite under humidity was slowed down due to a lower formation of Pb⁰. Regarding the thermal stability, thermal cycles of 2h at 85°C with 15% RH followed by a cool down at RT for 1h were done. After 18 cycles, SC10 and SI10 retained more than 90% of their initial PCE versus only 80% for pure Pb-based PSCs. The better thermal stability of Sr-based devices is assigned [163] to a doubled R_{rec}, during the thermal cycles leading to an effective diminution of recombination within the perovskite. With this

report, Zhang et al. proved the benefits of Sr-substitution in PSCs not only regarding the lead-reduction for environmental purpose but also for the enhancement of the devices that we know to be also a major issue.

Diverse reports, using Sr as additive, have also been published these last years and are sometimes depicted as articles on lead-less perovskite solar cells. However, it is important to note that, in these cases, Sr is not a substitute for lead but only an additive. In the following paragraph, we depict some of these works to complete the state-of-the-art of Sr use in PSCs, but we do not mention them as lead-less Sr-Pb PSCs.

In 2016, Pérez-del-Rey and co-workers reported the use of SrI₂ and SrCl₂ as additives in perovskite precursor solution ^[164]. Addition of 2% of SrI₂/SrCl₂ in MAPbI₃ perovskite effectively suppressed charge recombination thanks to the formation of a thin Sr(C₂H₃O₂)₂ film on top of the perovskite layer, resulting in a big increased of the FF parameter. Decreased crystal dimension and roughness as well as a surface Sr²⁺ enrichment and increased work function were also associated to Sr²⁺ addition. Resulting devices with FTO/PEDOT:PSS/MAPbI₃:Sr²⁺/IPH/Ba-Ag solar cell architecture achieved PCE superior to 15%. The year after, Zhang et al. developed an HTL-free fully printable PSCs with SrCl₂ additive ^[165]. By using 10 mol% of SrCl₂, the perovskite crystallization process was tuned to facilitate the formation of a denser film with inhibited defect generation and substantially enhanced optoelectronic properties and performances of the devices. Complete FTO/c-TiO₂/m-TiO₂/MAPbI₃(SrCl₂)_{0.1}/m-Al₂O₃/carbon device reached an enhanced PCE of 15.9%, retained at 90% of its initial value after 1000h of illumination, which is an improvement of 22.3% compared to the efficiency achieved by undoped perovskite-based cells. More recently, Caprioglio et al. published the fabrication of inverted PSCs with Sr addition reaching a high V_{OC} of 1.18V ^[166]. Sr was found to segregate at (Rb_{0.05}(-Cs_{0.05}(MA_{0.17}FA_{0.83})_{0.95})_{0.95})Pb(I_{0.83}Br_{0.17})₃ perovskite surface causing a beneficial drastic reduction of non-radiative recombination at the perovskite/C₆₀ interface. This

reduction resulted from the combination of two effects of Sr addition: a preferential n-doping of the perovskite surface and the formation of a space-charge region combined with a locally larger band gap reducing the access of photogenerated holes to the perovskite surface. The PCE was enhanced from 19.4% to 20.3% with 2% Sr addition for ITO/PTAA/(Rb_{0.05}(-Cs_{0.05}(MA_{0.17}FA_{0.83})_{0.95})_{0.95}) Pb(I_{0.83}Br_{0.17})₃/C₆₀/BCP/Cu solar cells.

In summary, construction of high efficiency Sr-Pb lead-less PSCs with a high rate of Sr substitution appears to be more difficult than Sn-Pb PSCs because Sr affects the perovskite film morphology as soon as Sr percentage exceeds 5 to 10%, depending on the architecture and the deposition method. However, Sr substitution seems to be a good way to enhance the stability of PSCs, making Sr an interesting material. More attention should be devoted to deposition method and transport layers to counter the undesired effects of Sr on perovskite morphology. Developing ternary systems with Sr, Pb and another compatible element could also be an interesting approach for the development of Sr-Pb lead-less PSCs. All the literature results on the substitution of Pb by Sr are summarized in Table.2.

4. Other substitutions for lead-less PSCs

4.1. Other group 2 elements (Ba and Ca)

Sr²⁺ is not the only alkaline-earth-metal available to partially replace lead in PSCs (See Figure 2). Ba and Ca cations have the same valence as Pb²⁺ and an ionic radius of 149 pm and 114 pm (133 pm for Pb²⁺), respectively. They meet the requirements regarding the tolerance and octahedral factors to form a perovskite structure. In this subsection, Ba and Ca substitutions in PSCs are discussed.

An interesting paper detailing the crystal structure, stability and optoelectronic properties of lead-free CH₃NH₃BaI₃ was published in 2016 by Kumar et al. showing the effect of Ba on the perovskite material ^[167]. However, it will not be detailed in this review as our focus

is lead-less perovskites. In 2017, Chan et al. reported the effect of diverse alkaline- earth-metal cations on PSCs optoelectronic properties with a focus on Ba^{2+} substitution ^[168]. They tested Mg^{2+} , Ca^{2+} and Sr^{2+} cations with a substitution level up to 10% but all the resulting devices showed lower or equivalent (for the best) efficiencies. They noticed interesting properties for Ba^{2+} -based PSCs. For a Ba^{2+} concentration of 3%, the authors found an improved coverage, along with an improved crystallinity and a decreased roughness of the perovskite film. These morphological improvements resulted in an enhanced absorption, charge transport to the TiO_2 ETL and consequently a reduced recombination of the charge carriers. Absorbance and absorbance onset were also improved with Ba^{2+} substitution, causing notably a slight change in the bandgap of the perovskite from 1.62 eV to 1.59 eV. The complete FTO/ TiO_2 /MAPb_{0.97}Ba_{0.03}I₃/spiro-OMeTAD/Au devices achieved a champion PCE of 14,9%, representing an enhancement of 3.1% compared to the unsubstituted perovskite-based devices. When the cells were stored in a N_2 -filled glovebox with the purification system turned off allowing a RH of 1%, they retained 75% of their initial PCE after 700h, against only 40% for the pure-Pb-based devices (See Figure S10), which represent a great improvement. The year after, Wu and co-workers studied the effect of strontium and barium substitution in a FTO/ TiO_2 /MAPb_{1-x}(Ba_x/Sr_x)I₃/spiro-OMeTAD/ Au solar cell ^[169]. As already reported ^[168], a decreasing bandgap with increasing Ba^{2+} amount was observed. They also found a poor coverage with a too high Ba concentration. Nevertheless, contrary to the report above, Ba and Sr substitution was found to decrease the efficiency of the cells. More recently, Xiang et al. developed a lead-less solar cell based on CsPb_{1-x}Ba_xI₂Br perovskite ^[170]. Due to the larger ionic radius of Ba^{2+} , an expansion of the unit cell was found by XRD. The authors found that Ba did not incorporate into the perovskite lattice through Pb substitution but segregated into Ba-based non-perovskite phase which changed the I/Br ratio in the perovskite phase, leading to a better film quality. Inhibition of non-radiative recombination was proved upon Ba^{2+} addition,

allowing a higher output voltage of the final device. After optimization of the amount of Ba²⁺ to 20%, solar cells with an FTO/c-TiO₂/m-TiO₂/CsPb_{0.8}Ba_{0.2}I₂Br/spiro-OMeTAD/Au architecture reached a PCE of 14% with an overall improvement of photovoltaic parameters compared to the pure-Pb device that achieved only a 11.1% PCE. Other publications, such as the one by Zhang et al. ^[171] used barium as additive in PSCs as there was no substitution the lead-content was not reduced. They will not be detailed here.

Ca is another potentially interesting element but reports, on the use of Ca as a substituent for Pb, employ a very low percentage of Ca ($\leq 5\%$). Moreover, according to the theoretical study by Uribe et al. published in 2016 ^[172], Ca-based perovskites possess low mobility and high bandgap (≈ 3.5 eV), making them unsuitable for PSCs. Nevertheless, it is interesting to describe related works. In 2017, Wu and co-workers replaced PbCl₂ by CaI₂ in MAPbI₃ perovskite ^[173]. With 1 mol% of Ca, the roughness of the perovskite film was decreased and an enhancement of all the photovoltaic parameters (J_{SC} , V_{OC} , FF) was proved, leading to a champion PCE of 12.9%, compared to 10.7% for the pristine PSCs. More recently, Lau et al. reported the influence of Ca²⁺ substitution on fully-inorganic CsPbI₃ PSCs ^[174]. They proved the stabilization of the CsPbI₃ phase with Ca²⁺. A reduction of colloids in the precursor solution led to a more uniform distribution, larger grains and smoother films and consequently to a higher V_{OC} and FF . In addition, a Ca oxide layer was formed at the surface of the perovskite film, having a passivation effect and causing an improvement of the carrier lifetime with the better morphology of the perovskite film. After adjusting the Ca concentration to 5%, the resulting FTO/c-TiO₂/m-TiO₂/CsPb_{0.95}Ca_{0.05}I₃/P3HT/Au achieved a PCE up to 12.6%, which represented an improvement of 18.9% compared to the pristine cell. With the addition of a MgF₂ anti-reflection coating on top of the cell, the PCE reached 13.5%.

Based on the aforementioned results, alkaline-earth-metal cations influence mainly the morphology of the perovskite layer, but these effects are beneficial only for low amount of

substitution. To be a reliable possibility for the future, further work still needs to be done on these materials.

4.2. Transition metals (Cu, Co, Ag and Mn)

Transition metals are very abundant materials on earth. It looks like that some of them, with ionic radii smaller than Pb, can form perovskite structures such as copper (87 pm), cobalt (88 pm), silver (108 pm) or manganese (97 pm) (See Figure 2). Due to their stable valence states and same number of valence electrons as Pb, these transition metals are good candidates for lead substitution. From these observations, some researchers tried to incorporate them in PSCs.

In 2016, Jahandar et al. reported the use of CuBr₂ in the precursor solution to form MA(PbI₂)_{1-x}(CuBr₂)_x perovskite via a dripping method [46]. CuBr₂ with DMSO formed a CuBr₂-DMSO adduct in the perovskite precursor film under the dripping which was flowable during the annealing treatment, facilitating the reproducible formation of larger crystal grains in the perovskite film. Also, Cu doping was proved to increase the charge carrier density within the film and then improve the conductivity of the perovskite. An optimum concentration of 5 mol% was determined which improved the efficiency of the devices based on ITO/PEDOT:PSS/MA(PbI₂)_{1-x}(CuBr₂)_x/PCBM/LiF/Al solar cell architecture from 13.18% to 17.09%, with consistent increase of J_{SC} and FF . In 2017, Klug and co-workers studied the effects of Co substitution on MAPbI₃-based PSCs [175]. The authors reported a tuning of Fermi level as well as valence and conduction band edges (VBE and CBE) of the perovskite along Co addition as can be seen in Figure S11. Using PEDOT:PSS as ETL, the optimum Pb:Co molar ratio to have a perfect band alignment between perovskite and PEDOT:PSS was found to be 63:1. Another interesting feature of Co substitution is also the possibility to control the crystal structure transition from cubic to tetragonal at room temperature. Indeed, for Pb:Co ratio from 15:1 to

63:1 the perovskite crystallizes with a tetragonal structure, when for a ratio of 127:1, the perovskite crystallizes in a cubic structure. Finally, with a Pb:Co ratio of 63:1, the authors achieved a champion PCE of 17.2%, better than the pure-Pb PSCs with a PCE of 16.6% due to higher V_{OC} of 1.05V caused by the better band alignment between perovskite and PEDOT:PSS. The same year, Chen and co-workers partially substituted Pb by Ag, leading to a reduced electron recombination, an improved film morphology and a PCE up to 18.4%, which is an increase of 2.4% absolute compared to the pristine PSC^[176]. More recently, Liang et al. doped the all-inorganic CsPbIBr₂ perovskite with Mn^[177]. Various Mn amounts, x, were tested namely, 0.005, 0.01 and 0.02. They measured a decrease of the optical bandgap with increasing x which should improve the light harvesting and thus should be beneficial for the device overall efficiency. However, a strange morphological behaviour was observed by the authors (See Figure 8). For the smallest x (0.005), vertical branches emerged on the perovskite surface. These branches pierced the carbon electrode of the device and increased the contact area, boosting the hole transfer. Nonetheless, when the Mn amount was superior, fewer vertical branches were observed and pinholes were present in the film, leading to an enhancement of the charge recombination and loss in efficiency. The maximum efficiency was reached for an x=0.005 and was equal to 7.36% for a solar cell with an FTO/TiO₂/CsPb_{0.095}Mn_{0.005}I_{1.01}Br_{1.99}/carbon architecture, that is to compare to the 6.14% achieved without Mn. Once encapsulated, the devices retained 100% of their initial PCE after 300 h in ambient atmosphere, which is a tremendous increase compared to the undoped devices that started to decay after only 100h.

The same way as alkaline-earth-metals, transition metals exhibit very interesting and promising properties once substituted to Pb in PSCs, however, for these beneficial effects to occur, their amount must be low. Therefore, further work is still needed on these materials, but they seem promising, maybe not for pure “lead replacement” but for increasing efficiencies. Also, if the stability of PSCs could be drastically increased by small substitution of lead by one

of these metals, then it could still reduce the pollution of PSCs by increasing the lifetimes of the devices and then be a suitable solution for the future of this technology.

4.3. Group 12 to 14 elements (Zn, In, Ge)

Elements from group 12 and 13 (See Figure 2) have also been used for the partial replacement of lead but their ionic radii (88 pm for Zn^{2+} and 94 pm for In^{3+}) are smaller than that of Pb^{2+} . In 2017, Jin et al. developed MAPbI₃ solar cells by partially replacing Pb by Zn [178]. They proved that Zn influences the crystallization process and grains growth and then, depending on the Zn concentration, the film morphology was improved or deteriorated in a dripping process. With increasing Zn%, grains became bigger but too much Zn also caused the appearance of cracks and pinholes in the layer, limiting the doping concentration at 3 at.% maximum. Enhanced absorbance and a slight downshift of the conduction and valence bands were also determined for a Zn amount of 3 at.%. With this optimized concentration, they achieved a PCE up to 18.2% with improved stability. As a comparison, the solar cells without Zn reached a PCE of 16.4%. Figure 9 shows the evolution of the photovoltaic parameters for unencapsulated cells stored in an ambient environment of 25-28°C with 30-55% RH. Interestingly, the proportion of 3 at.% Zn was lately, in 2019, found to be the optimum value for MAPb_{1-x}Zn_xI₃ perovskite according to theoretical calculations [179]. More precisely, an amount of 3.125% should improve the absorbance and decrease the formation energy of the perovskite, thus leading to better photovoltaic performances.

Indium, although it has a trivalent cation In^{3+} , can be used in PSCs to substitute partially lead as reported Wang and co-workers [47]. Their MAPb_{1-x}In_xI_{3-x}Cl_x-based PSCs exhibited high film quality with multiple ordered crystal orientations, which is beneficial for efficient charge transport along different directions within the perovskite layer. These multiple orientations were due to the stronger interaction between MA and inorganic cations. They also proved that

In addition caused a decrease in grain size along with a reduced pinhole density. Those benefits allowed an enhancement of all photovoltaic parameters once the In concentration was optimized at 15 at.%. Complete ITO/PEDOT:PSS/MAPb_{1-x}In_xI_{3-x}Cl_x/PCBM/Bphen/Ag solar cells then exhibited a PCE increase of 39% compared to the unsubstituted devices with a champion PCE of 17.55%.

Germanium belongs to the same group 14 as lead and tin and is thus a possible substituent for lead. First use of Ge were reported in lead-free PSCs around 2015 but with very low efficiency^[180,181]. Some studies continued to be done on this materials but a high efficiency was never reached^[182–184]. Lead-free PSCs based on Ge gave no results due to the too large bandgap resulting in the collection of UV-light alone. Some groups focussed their attention to the Pb-Ge lead-less systems. A complete theoretical study led by Sun et al. in 2016 detailed the optoelectronic properties and structural nature of MAPb_{1-x}Ge_xI₃ perovskite regarding different amount of Ge (from 0% to 100%)^[185]. They showed that the absorption of the perovskite increases with the amount of Ge while the bandgap decreases. In addition, a great improvement in charge transport properties and effective masses was calculated. Hence, mixed Ge/Pb MAPI₃ perovskites could be great candidates for replacing pure Pb perovskites in PSCs. A theoretical maximum PCE of 24.24% was even calculated for MAGE_{0.75}Pb_{0.25}I₃ perovskite. In 2018, Yang et al. fabricated an all-inorganic CsPb_{1-x}Ge_xI₂Br perovskite in ambient air conditions at 50-60% RH with enhanced efficiency and stability^[186]. Upon addition of Ge, the authors observed smaller grains along with an increased cubic phase stability while pure Pb perovskite crystallized in an orthorhombic phase. According to the authors, this enhanced cubic phase stability could be due to two phenomena: the reduced crystal size with Ge substitution that induced lattice strain and the transformation of Ge²⁺ into Ge⁴⁺ that could form a passivation layer and increase the phase stability. Slight increase of absorption onset as Ge content increased was also determined, resulting in a lower bandgap with Ge addition. With an

optimized amount of Ge of 20%, an increased absorption as well as a better effective recombination lifetime were achieved, allowing the final solar cells to reach a really high V_{oc} of 1.27 V and PCE up to 10.8%, which represented an enhancement of more than 100% compared to the pure-Pb ones. The non-doped PSCs short-circuited after only 2h in ambient atmosphere with 50-60% RH but the Ge-doped devices retained the entirety of their PCE after 7h which is a very good improvement even if this small range of time doesn't well-reflect the real stability of the device. A PCE exceeding 10% for lead-less PSCs fabricated under ambient atmosphere is a very promising result for the future of lead-deficient perovskite solar cells. However, one important limitation for Ge-Pb lead-less PSCs is the terribly poor solubility of GeI_2 in solution with organic cations inside. With this observation, in 2020, Kim et al. developed a way to overcome this problem by adding methylammonium chloride (MACl) into the precursor solution with GeI_2 [187]. They found that MACl remarkably increased the solubility of GeI_2 leading to high-quality films by using a dripping method (See Figure S12). With GeI_2 percentage, a decreasing roughness of the perovskite film surface and grain size were found due in part to the passivation caused by the segregation of GeI_2 at GB. An astonishing increase of the carrier lifetime was also obtained with a lifetime of 18846 ns for 3% Ge thanks especially to a more specific orientation of perovskite crystals. Complete FTO/ TiO_2 / SnO_2 / $\text{FA}_{0.87}\text{MA}_{0.13}(\text{Ge}_x\text{Pb}_{1-x})(\text{I}_{0.9}\text{Br}_{0.1})_3$ /spiro-OMeTAD/Au device, with a Ge content of 3%, achieved a champion PCE of 22.09%, retaining 80% of its original value after 1 month at RT with 30-40% RH unencapsulated. This performance has to be compared to the pristine PSCs that achieved a PCE up to 21.27% and retained only 40% of its original value in the same conditions. The same GeI_2 substitution was also conducted in a quadruple cations $\text{K}_{0.03}\text{Cs}_{0.05}(\text{FA}_{0.87}\text{MA}_{0.13})_{0.92}(\text{Ge}_x\text{Pb}_{1-x})(\text{I}_{0.9}\text{Br}_{0.1})_3$ perovskite-based PSCs and a PCE of 22.7% was reached using the same protocol.

Group 12 and 13 elements such as Zn and In seems less interesting for integration in PSCs according the result reported above. Nevertheless, Ge could be a promising solution to partially replace lead in PSCs regarding both efficiency and stability but efforts to increase its content still has to be done to compete with Sn.

4.4. Group 15 elements (Sb, Bi)

Antimony and bismuth, although being trivalent cations (Sb^{3+} and Bi^{3+}), possess the requirements regarding the tolerance (Eq.1) and octahedral (Eq.2) factors, combined with a stable valence state. They can then be considered as substituents in perovskite structures.

Like Sn or Ge, Sb was first use in lead-free PSCs. Some developments were made over the years but the efficiency of Sb-based lead-free PSCS are low ^[188–191]. Some researchers then developed binary Sb-Pb lead-less PSCs. In 2016, Zhang and co-workers studied the effect of Sb substitution on $\text{MAPb}_{1-x}\text{Sb}_{2x/3}\text{I}_3$ PSCs ^[192]. They found a tunable bandgap from 1.55 eV to 2.06 eV for Sb content varying from 0 to 100% due to stronger Sb-I interaction. Interestingly, they noted no change in the crystal lattice size for Sb amount inferior to 10%. In this range, an upshift of the perovskite quasi-fermi level was determined, synonym of an improved electron transfer efficiency with notably a doubled diffusion length for 1% Sb. With this amount, they achieved the best solar cells with a PCE reaching 15.6%, resulting in an improvement of 19% compared to pure MAPbI_3 PSCs. It is important to note that the authors did not precise the method used to fabricate the perovskite film, so the characteristics detailed above must be read carefully. The same year, Oku et al. also reported the influence of Sb on $\text{MAPb}_{1-x}\text{Sb}_x\text{I}_3$ PSCs properties ^[193]. By using a single-step method to form their perovskite film, they proved that Sb substitution increased the perovskite lattice and suppressed excess PbI_2 formation. Contrary to the results by Zhang et al., an optimum concentration of 3% was found to give the best efficiency even if the same FTO/c-TiO₂/m-TiO₂/MAPb_{1-x}Sb_xI₃/spiro-OMeTAD/Au stack was

employed as PSCs. With this Sb concentration and architecture and by using a single-step method for the perovskite layer preparation, a PCE up to 9.07% was achieved, representing an enhancement of 2.51% in absolute compared to the unsubstituted devices. The year after, Chatterjee and co-workers developed a modified two-step method to fabricate efficient ITO/NiO_x/MAPb_{1-x}Sb_xI₃/PCBM/Al PSCs^[44]. In a classic two-step method, MAI is dropped on a dried PbI₂ layer (see section 2.3.2). The authors dropped MAI on a wet PbI₂. They noted a major influence of the loading time, i.e. the time at which the second spin-coating step was started after the MAI dropping onto the wet PbI₂ layer, on the residual PbI₂ content and surface roughness of the final perovskite film. Figure 10 shows the influence of the loading time, noted τ_{load} by the authors, on residual PbI₂ amount and perovskite film surface roughness for a Sb percentage of 8%. The loading time had a major impact on the surface roughness and residual PbI₂ content, influencing the photovoltaic parameters of the final device. An optimized τ_{load} of 40s was found, which allowed the achievement of a PCE of 12.8% for MAPb_{0.92}Sb_{0.08}I₃-based PSCs.

Bismuth was also investigated in lead-free PSCs in double perovskite structures^[91-93] or in Ag/Bi-based PSCs^{[95,96][194]}. Partial lead substitution by Bi was evaluated in lead-less PSCs but few reports are available. An interesting one was published in 2017 by Hu et al.^[195] who studied Bi incorporation in all-inorganic CsPb_{1-x}Bi_xI₃ PSCs. Bi³⁺ was proved by the authors to suppress the formation of the inactive yellow phase in CsPbI₃ perovskite and to decrease the conversion temperature of the black stable phase to 100°C, leading naturally to a better stability of the final devices. By adjusting the Bi concentration at 4 mol%, better absorbance and stunning decrease of charge transport resistance were achieved, leading to a better conductivity. Thanks to all these benefits, an improvement of 5% of the PCE was reached with a champion PCE for FTO/TiO₂/CsPb_{0.96}Bi_{0.04}I₃/CuI/Au solar cells of 13.21%. It retained 68% of its initial

value after 168h of storage at 25°C with a RH of 55% due to the better stabilization of the black phase at room temperature.

In the same way as all the other elements presented in this section, group 15 elements seem interesting but suffer from the same problem: a too low content is needed to obtain beneficial effects. Furthermore, these materials seem to us less interesting than Ge or other materials presented in this review.

4.5. Ternary systems

Due to the numerous possible replacements for lead in PSCs, it is possible to realize ternary systems by mixing lead with two other elements. This kind of system has the advantage to combine diverse properties and counter some negative effects of precise material by mixing it with another one having the opposite effect, leading finally to a better final device. In 2018, Li et al. fabricated an innovative $\text{MAPb}_{0.9}\text{Sn}_{0.05}\text{Cu}_{0.05}\text{I}_{2.9}\text{Br}_{0.1}$ -based PSCs with a planar FTO/TiO₂/perovskite/spiro-OMeTAD/MoO₃/Ag structure ^[196]. By combining the effects of Sn²⁺ and Cu²⁺ substitutions that are respectively (i) a redshift of the absorption onset with a decrease of the perovskite film quality and (ii) an improved morphology and crystallization of the Sn-containing perovskite by passivating trap sites at the crystal boundaries without affecting the absorption, they achieved a PCE up to 21.08%, i.e an improvement of 3.19% absolute compared to pristine MAPbI₃-based solar cells due to a major enhancement of J_{SC} and FF. More recently, Liu and co-workers realized a theoretical study of $\text{MAPb}_{1-x-y}\text{Sn}_x\text{Ge}_y$ -based PSCs in terms of geometric structure, optoelectronic properties and efficiency through DFT calculations ^[197]. According to their calculations, this ternary perovskite should have a better structural stability than classic MAPbI₃ perovskite and also a tunable bandgap that could vary from 0.91 eV for MASnI₃ to 1.77 eV for $\text{MAPb}_{0.75}\text{Ge}_{0.25}\text{I}_3$. After simulating a lot of Pb:Sn:Ge ratio, the authors revealed that the better ratio should be 50:25:25, leading to an efficiency of 23.65%,

This article must be cited as:

L. Gollino, T. Pauporté, Lead-Less Halide Perovskite Solar Cells

Sol. RRL **2021**, *5*, 2000616 DOI: 10.1002/solr.202000616

WILEY-VCH

with a bandgap of 1.37 eV, a J_{sc} of 30.17 mA/cm² and a V_{oc} of 0.87V. The solar cell architecture is yet not indicated, so this report must be read with care.

In brief, a lot of different elements can be used as substituents in order to realize lead-less PSCs with all their intrinsic benefits and drawbacks. Still, transition metals and germanium look more promising than the others according to the reports presented in this review. To further develop lead-less PSCs based on these materials, researchers should focus on compositional engineering with maybe use of dopants and the development of selective contact materials to increase the amount of lead substituted without impacting too much the efficiency of the PSCs. All the results presented in section 3 and 4 are summarized in Table 2.

5. Partial lead and halide replacement by large organic cations

Insertion of medium/big-sized organic cations is a well-known mechanism to achieve 2D perovskites [58,87,198]. Recently, two groups, Prof. N. Mercier's group and Prof. M.G. Kanatzidis' group found that insertion of specific organic cations that do not respect the tolerance factor for the perovskite lattice do not form 2D perovskite but cause the substitutions of (PbI)⁺ entities (Pb²⁺ and I ions) by these organic cations. It leads to the retention of the 3D structure of the perovskite but with (PbI)⁺ deficiencies [199] (See Figure 11b). This new family of perovskites was called d-HPs (for lead and iodide deficient halide perovskite) by Mercier et al. and "hollow" perovskites by Kanatzidis et al.. However, the "Hollow" terminology is not really adequate as (PbI)⁺ entities do not leave a blank space in the perovskite structure but are replaced by organic cations. The main difference between the d-HPs and the "Hollow" perovskites is the cations used to create the vacancies. "Hollow" perovskites are mainly based on the use of ethylenediammonium (en), propylenediammonium (PN) and trimethylenediammonium (TN), while d-HPs have been presently developed with 4 different organic cations : Hydroxyethylammonium (HEA⁺), Thioethylammonium (TEA⁺),

Fluoroethylammonium (FEA⁺) and an expanded dication (Dic²⁺). To be as clear as possible, both names will be used in the rest of the review to distinct the works from Mercier et al. and Kanatzidis et al.. In this section, we will first discuss the d-HPs before to summarize the works on "Hollow" perovskites.

In 2017, Mercier and co-workers developed and patented, in collaboration with our group, a new family of perovskite called the d-HPs [200,201]. d-HPs are created by the insertion of a big-sized organic cations that do not respect the Goldschmidt tolerance factor [202]. This insertion is permitted by the creation of lead and iodide vacancies in the perovskite lattice, which retains the 3D perovskite structure, contrary to the cation's spacer used to form 2D perovskites. All the d-HPs based on HEA⁺, TEA⁺, FEA⁺ and Dic²⁺ were tested in powder, single crystals and thin films [200]. They exhibited an interesting modulation of their optoelectronic properties (absorbance, excitonic energy, electronic structure) via the modification of their vacancies content. For a certain content of organic cations, it was also found that the d-HPs act like a mix of 3D and 2D perovskites, with the possibility to retain the advantages of both structures in a unique one like, for example, a better air stability for all d-HPs cited above for a wisely chosen substituent amount. In 2017, Leblanc et al. reported specifically the optoelectronic properties and efficiencies of PSCs based on the deficient perovskite d-MAPI-HEA⁺ for a HEA⁺ content (x) between 0.1 and 0.2 [203]. In the patent, the general formula for d-HPs is written as follow:

$$[(A)_{1-2.48p-b}(B)_{3.48p+b}]_{\frac{(1+2p-y)}{1+p}}(Pb)_{1-p-m}(M)_m(X^1)_{3-y-q}(X^2)_q \quad (8)$$

where A is a cation among Cs, Rb, MA and FA; B a monovalent organic cation with a R¹-(CH₂)_{1,2,3}-R² formula, X¹ and X² are halogens. Based on this formula, the formula proposed for d-MAPI-HEA⁺ perovskite is (HEA)_{3,48x}(MA)_{1-2,48x}[Pb_{1-x}I_{3-x}], where x is the HEA⁺ content. Figure 11 shows the proposed structure of d-MAPI perovskite with the Pb-I vacancy created in the lattice with HEA⁺ incorporation determined after XRD measurements. The XRD patterns

contained supplementary peaks at low angles (around 5° - 6° 2θ) for powdered d-MAPI. These peaks were attributed by the authors to ordered Pb^{2+} and I vacancies, leading to a different crystalline structure than classic MAPI. The authors revealed that with increasing x , the main band of the absorbance spectra was blue-shifted, and the overall absorbance intensity was decreased, which is in good agreement with the colour of the films (See Figure 11c). The complete devices based on the FTO/c-TiO₂/m-TiO₂/ HEA_{0.348}MA_{0.752}Pb_{0.9}I_{2.9}/spiro-OMeTAD/Ag achieved an efficiency up to 6%. The efficiency is still quite low, but very few optimizations have been implemented to increase the performances and important progress can be expected in the future for this new family of lead-less PSCs. More recently, Mercier and co-workers published a detailed report on d-HP based on FAPbI₃ with HEA⁺ and TEA⁺ called d- α -FAPbI-HEA and d- α -FAPbI-TEA respectively [202]. In this study, HEA⁺ and TEA⁺ amount of 0.13, 0.15 and 0.04, 0.013, respectively, were tested. Thanks to ¹³C NMR (Nuclear Magnetic Resonance) characterizations, it was determined that HEA⁺ and TEA⁺ could possibly occupy 3 different sites within the perovskite lattice (See Figure S13). The same way as for d-MAPI [203], the use of HEA above a certain amount turned the perovskite to an orange/reddish tint leading inevitably to a lowered absorbance. However, for d- α -FAPbI-TEA the films remained black even for an amount of 0.13. The use of TEA⁺ to form d-HP was proven to significantly enhance the stability of the perovskite films compared to classic FAPbI₃ and CsFAPbI₃ perovskites (See Figure S14). Under very humid conditions of 75-90% RH at 25°C, FAPbI₃ and CsFAPbI₃ films were entirely decomposed after only 50h. On the other hand, for TEA⁺ amount of 0.04 and 0.13, the perovskite films were stable and retained a black colour after 170h and 266h, respectively. These systems are under testing in PSCs, and their astonishing stability under high humidity conditions makes them very interesting for the future.

3D "Hollow" perovskites were first discovered for lead-free compounds. They are based on the use of ethylenediammonium ($\{\text{en}\}$), a medium sized cation, as an additive. The first

report mentioning hollow perovskite was published in 2017^[105]. By using {en} in FASnI₃ the authors revealed a retention of the 3D structure of the perovskite despite the important size of {en} which violates the tolerance factor. This retention of the 3D structure was found to be due to the creation of randomly distributed Schottky defects within the perovskite lattice. Such an original structure allowed an important tuning of the bandgap along with an increase of efficiency and stability. Indeed, an improvement of the efficiency from 1.4% to 7.14% with incorporation of 10% {en} was achieved. Moreover, the PCE retained its original value after 1000h of storage in air once the devices were encapsulated. This very encouraging result motivated the authors to investigate further these "hollow" perovskites. The same year, they reported the use of a dopant-free HTL, the tetrakis-triphenylamine (TPE) allowing better performance than PTAA used in their previous report^[204]. Using the same FTO/c-TiO₂/m-TiO₂/ {en}FASnI₃/HTL/Au architecture, a slightly better PCE of 7.23% was reached with TPE as HTL. Even if this enhancement is not significant, it is still interesting to note that higher efficiencies with simpler systems not requiring additives/dopants can be obtained. Such results are interesting in regard of the future industrialization of PSCs that will need to be as simple as possible. In the meantime, Kanatzidis group tested "hollow" {en}MASnI₃ and {en}CsSnI₃ perovskites^[205]. Efficiencies up to 6.63% and 3.79% respectively with better air stability were achieved, representing an important enhancement compared to pristine devices. In 2018, a paper was published to unravel the mechanisms and properties of "hollow" perovskites^[206]. The dication {en} was found to be too large to fit within the perovskite lattice but still fit by partially replacing inorganic ions, i.e. metal (M) and halide (X) ions, thus creating random massive M and X vacancies in the 3D [MX₃] framework (See Figure S15). The general formula (A)_{1-x}{en}_x(M)_{1-0.7x}(X)_{3-0.4x} was then formulated. The authors unveiled that the elimination of the inorganic M and X chunks remarkably modified the band dispersion, resulting in wider bandgaps. For example, {en}FASnI₃^[105] and {en}MASnI₃^[205] bandgaps could be tuned from

1.3 to 1.9 eV and from 1.25 to 1.4 eV respectively by using different amount of {en}. Being able to greatly modify the bandgap by A-cation substitution is an important step forward as it normally results in just a small change in the bandgap due to structural distortion. Other interesting properties of “hollow” perovskites are the reduction of the dark current and the charge carrier trap density as well as the increase of the carrier lifetime. The authors suggest that this reduced dark current is due to the {en} incorporation in combination with the hollow nature (presence of vacancies) that somehow inhibits the Sn⁴⁺ doping. “Hollow” perovskites, with their higher organic content and particular structure were found to slow down the decomposition process of the perovskite and thus improve the air stability of the final devices. More recently, two substitutes of {en} with slightly bigger radius, propylenediammonium (PN) and trimethylenediammonium (TN) were depicted and efficiencies of 5.85% and 5.53% respectively were achieved for content of 10%. More recently, this group tested also “hollow” perovskite in lead-less PSCs. In 2019, Ke et al. reported FTO/PEDOT:PSS/{en}FA_{0.5}MA_{0.5}Pb_{0.5}Sn_{0.5}I₃/PCBM/BCP/Ag PSCs^[207]. {en} content of 5% and 10% were tested, corresponding to a bandgap evolution from 1.27 eV to 1.36 eV. The insertion of {en} was proved, similarly to lead-free PSCs, to reduce the dark current and carrier trap density and also to increase the carrier lifetime, leading to enhanced efficiencies (See Figure 12). Even if the performances were enhanced, the V_{OC} was still low (< 0.8 V), due to numerous recombination within perovskite film and at the interfaces. To solve this problem, they used a MABr overlayer on top of the perovskite film. After spin-coating 5 mg/mL of MABr solution on top of {en}FA_{0.5}MA_{0.5}Pb_{0.5}Sn_{0.5}I₃ layer, a downshift of the VBM and CBM was observed, suggesting a replacement of surface iodide atoms by bromide atoms. The VBM downshift was particularly useful as it permitted an enhanced charge transfer toward the HTL and then a reduction of the recombinations in the device. The combined use of {en} to form the “hollow” perovskite, with MABr to reduce the recombination, resulted in devices that achieved

a champion PCE of 17.04% with enhanced air stability (Figure 12e) which is close to the best efficiency reported for Sn:Pb ratio of 50/50 but with better stability.

In summary, thanks to their structure and properties, the d-HPs and "Hollow" perovskites are very interesting to reduce the lead content in PSCs. The former is a very recent new family of perovskites that deserved more investigation. Other organic cations mentioned above still need to be tested and PSCs with all these d-HPs have to be done to attract more attention of the photovoltaic community. "Hollow" perovskites that have been more studied reached higher efficiencies (17.04%) but exhibited poorer stability than d-HPs. However, given the few researchers presently working on these compounds, progress is slow, but it remains a very interesting axis of development for highly efficient and stable lead-less PSCs.

6. Other ways to fabricate lead-deficient and less polluting PSCs

The strategies detailed so far were based on the chemical replacement of lead by another element or other elements in order to realize lead-less PSCs. However, other approaches have also been considered. In 2019, Zheng et al. reported a theoretical study to reduce lead content in PSCs via a physical method consisting in reducing the thickness of the perovskite layer^[208]. Using the Transfer Matrix Model (TMM), the authors modelled the absorption of the MAPbI₃ perovskite layer for two different structures: normal planar ITO/SnO₂/perovskite/spiro-OMeTAD/Au and inverted ITO/PEDOT:PSS/perovskite/PCBM/Ag. According to their calculations, the photocurrent mainly originates from the first few hundreds nanometers of the perovskite layer (See Figure 13). They calculated that with a thickness of 200 nm and 150 nm, J_{SC} reached 85% of its maximum value for normal and inverted structure, respectively. However, in real cells, the perovskite layers are experimentally around 400-600 nm thick to ensure the full light absorption and avoid optical interferences that could reduce J_{SC} . The

introduction of what the authors call "optical spacers" between the perovskite and the charge transport layers could theoretically reduce optical interferences and allow the diminution of the perovskite layer thickness while retaining a J_{SC} close to its max value. Those optical spacers would be, conforming to the calculations, ZnO nanoparticles (NPs) and MoO₃ inserted at perovskite/ETL and perovskite/HTL interfaces, respectively. With those, the perovskite layer thickness could be reduced to one-third, representing a lead reduction of 70% while the devices would retained 96% of their efficiencies compared to the conventional one. This work being purely theoretical, the results must be considered with care. Experimentally, all the interfaces, contacts, layers etc. should be optimized, making the realization of these ultrathin PSCs difficult. Nevertheless, the possibility to reduce lead content by 70% without impacting severely the efficiency is very attractive and will surely lead to many investigations.

Other researches on what is called light management in PSCs were conducted by different group [209]. This light management is used to reduce the part of light that is reflected at the surface of the cell and to increase the path length of the light within the absorbing material. This engineering is well-studied for silicon solar cells with notably the use of diffuse reflectors [210]. For PSCs, light management is mainly studied through the use of nanoparticles. One of the first report was published by Zhang et al. in 2013 [211]. Nanoparticles were found to potentially enhance the absorption of the perovskite layer [212]. All these properties are very promising for a possible lead-content reduction in PSCs. Indeed, by adding nanoparticles within the perovskite layer and then enhancing its absorption and more generally optimizing the light collection, the reduction of the perovskite layer thickness and then the lead amount in PSCs could be possible.

In order to reduce the toxicity of PSCs, reduction of lead-content is not the only option. Working on the stability to improve the lifetime of PSCs is also a good alternative. Indeed, by fabricating devices with excellent stability of several months or years, the pollution issue would be highly

reduced. In 2019, Wang et al. published a review on the stability of PSCs^[213] in which they reported highly stable systems. Among them, some retained more than 90% of their initial PCE after several months^[214–217]. In 2016, Bella and co-workers developed a PSC with front and back coating of photocurable fluoropolymers that allowed a huge boost of the stability of the device^[218]. The front-coating was made of a mix of UV-curable chloro-trifluoroethylene vinyl ether fluoropolymer binder, a dimethacrylic perfluoropolyether oligomer and a fluorescent organic dye Lumogen F Violet 570 by BASF. The back-coating was just a moisture-resistant fluoropolymeric layer. Thanks to the coatings, the final devices retained 100% of their original PCE after 6 months under continuous UV light irradiation, separated in 3 months under Ar atmosphere and 3 months in air with 50% RH. Such a stability is excellent for PSCs but is still low compared to the commercialized Si-based solar panels. In the future, if PSCs achieve stability that can be counted in years, the lead toxicity concern will be greatly reduced, and the industrialization will be possible for this technology.

Another way to reduce the toxicity of perovskite solar cells is to work on the recycling of the lead element. This topic is out of the scope of the present review but the main interesting insights are summarized in **Section A** of the Supporting Information. Instead of directly substituting Pb to reduce its amount in PSCs, other methods were developed and are currently studied to reduce the pollution and toxicity linked to PSCs. Whether via physical reduction, improvement of the stability of the devices, or recycling lead directly from PSCs or other sources to fabricates recycled devices, all these approaches are interesting and promising to combat the toxicity of the lead-perovskite technologies.

7. Conclusion and outlooks

Lead toxicity hinders the development of PSCs at an industrial scale. In this review, we have depicted all the strategies reported up to now to reduce the lead content in these devices and lessen their toxicity. Either lead substitution by various elements, introduction of medium

to big-sized organic cations to create Pb-I vacancies within the perovskite lattice, perovskite layer thickness reduction, stability improvement or lead recycling, are all viable approaches.

Sn substitution is the most studied method for lead reduction. It can not only reduce lead content to a big extent but also modify absorption and bandgap, allowing PSCs to have the ideal bandgap around 1.4eV, making it highly interesting for single junction PSCs [219–222]. All deposition techniques and common additives were tested, leading to a profusion of results about this system. With many groups reached efficiencies above 18% [110,128,136] and a record of 20.63% [137] for an important Sn content of 30% has been reported. Another result to point out is a device that reached a 20.2% PCE for a Sn content of 60 mol% [136]. Sn-Pb lead-less PSCs are the most promising for the replacement of pure Pb-based PSCs. However, those systems suffer from a poor stability due to the oxidation of Sn²⁺ to Sn⁴⁺, so big efforts must still be made on this point to render it viable in the near future, through chemical engineering, additive engineering, interfaces and contact engineering and also encapsulation. The latter is a really important facet of the stability of photovoltaic solar cells which was not discussed in this review. Important studies should also be carried out on the effects of Sn decomposition products on the environment to attest the seriousness of those in lead-less PSCs.

Lead substitutions by other elements detailed in this review are also worth considering due to their influence mainly on perovskite film morphology and bandgap. Nevertheless, to achieve efficiencies that can be compared to Sn-Pb or pure-Pb PSCs, the amount of substituent has to be very low (under 10%), the best efficiency reached is 22.09% but for a Ge content of only 3 mol% [187], and yet, the stability is not good since Ge suffers from the same oxidation problem as Sn. Important work needs to be implemented to increase the amount of substituent without impacting dramatically the performances of the devices. Ternary systems may provide the solution to this concern.

New families of perovskites have been discovered the past three years: the d-HPs/ "Hollow" perovskites. They are based on a similar principle, the insertion of an organic cation that do not respect the tolerance factor and cause Pb-I vacancies within the perovskite lattice. On one hand, an "hollow" perovskite reached an efficiency of 17.04% for a 50:50 Sn:Pb-based perovskite with a quite low air stability ^[207]. On the other hand, d-HPs reached lower efficiencies with recent d-MAPI-HEA cells reaching efficiencies superior to 9% (results not published) but exhibited a better stability than their rivals. This research is emerging and a lot of improvement is awaited, not only for the efficiency (only one cation on four was tested in devices) but also regarding the stability.

More atypical ways to reduce the toxicity exist such as physical lead reduction ^[208]. This one seems very interesting to us as it explores a path not studied and according to the calculations could greatly reduce lead content and then toxicity without decreasing much the efficiency. We encourage researchers to explore the experimental part of this study to obtain interesting results that could be combined to lead-less PSCs to further decrease lead content in the devices. Lead recycling is also a very interesting point to study. If, in the near future, PSCs can be recycled to fabricate high-efficiency PSCs again, this technology should have a bright future.

Finally, all the strategies depicted have attractive points. This research field is growing and of high interest since lead reduction in PSCs should render possible the industrialization of this technology and avoid the reluctance of a part of the consumers. Nevertheless, in view of the numerous articles published on this topic, and its growth year after year, there is no doubt that, in the future, lead-less PSCs will play a major role in the energy field.

Supporting Information

This article must be cited as:

L. Gollino, T. Pauporté, Lead-Less Halide Perovskite Solar Cells

Sol. RRL **2021**, *5*, 2000616 DOI: 10.1002/solr.202000616

WILEY-VCH

Supporting Information is available from the Wiley Online Library or from the author.

Acknowledgements

The ANR French Agency of Research is acknowledged for financial support (MORELESS project ANR-18-CE05-0026)

Received: ((will be filled in by the editorial staff))

Revised: ((will be filled in by the editorial staff))

Published online: ((will be filled in by the editorial staff))

References

- [1] Leyden M. R., Terakawa S., Matsushima T., Ruan S., Goushi K., Auffray M., Sandanayaka A. S. D., Qin C., Bencheikh F., Adachi C. *ACS Photonics*, **2019**, *6*, 460–466.
- [2] Wei Y., Cheng Z., Lin J. *Chem. Soc. Rev.*, **2019**, *48*, 310–350.
- [3] Miao J., Zhang F. *J. Mater. Chem. C*, **2019**, *7*, 1741–1791.
- [4] Wang H., Kim D. H. *Chem. Soc. Rev.*, **2017**, *46*, 5204–5236.
- [5] Mykhaylyk V. B., Kraus H., Saliba M. *Mater. Horizons*, **2019**, *6*, 1740–1747.
- [6] Zhang J., Barboux P., Pauporté T. *Adv. Energy Mater.*, **2014**, *4*, 1400932.
- [7] Zhang J., Juárez-Pérez E. J., Mora-Seró I., Viana B., Pauporté T. *J. Mater. Chem. A*, **2015**, *3*, 4909–4915.
- [8] Yoo J. J., Wieghold S., Sponseller M. C., Chua M. R., Bertram S. N., Hartono N. T. P., Tresback J. S., Hansen E. C., Correa-Baena J. P., Bulović V., Buonassisi T., Shin S. S., Bawendi M. G. *Energy Environ. Sci.*, **2019**, *12*, 2192–2199.
- [9] Liu Y., Akin S., Pan L., Uchida R., Arora N., Milić J. V., Hinderhofer A., Schreiber F., Uhl A. R., Zakeeruddin S. M., Hagfeldt A., Ibrahim Dar M., Grätzel M. *Sci. Adv.*, **2019**, *5*, eaaw2543.
- [10] Pitarch-Tena D., Ngo T. T., Vallés-Pelarda M., Pauporté T., Mora-Seró I. *ACS Energy Lett.*, **2018**, *3*, 1044–1048.
- [11] Wang P., Shao Z., Ulfa M., Pauporté T. *J. Phys. Chem. C*, **2017**, *121*, 9131–9141.
- [12] Wang P., Ulfa M., Pauporté T. *J. Phys. Chem. C*, **2018**, *122*, 1973–1981.
- [13] Kojima A., Teshima K., Shirai Y., Miyasaka T. *J. Am. Chem. Soc.*, **2009**, *131*, 6050–6051.
- [14] Chung I., Lee B., He J., Chang R. P. H., Kanatzidis M. G. *Nature*, **2012**, *485*, 486–489.
- [15] Lee M. M., Teuscher J., Miyasaka T., Murakami T. N., Snaith H. J. *Science (80-.)*,

- 2012**, *338*, 643–647.
- [16] Kim H. S., Lee C. R., Im J. H., Lee K. B., Moehl T., Marchioro A., Moon S. J., Humphry-Baker R., Yum J. H., Moser J. E., Grätzel M., Park N. G. *Sci. Rep.*, **2012**, *2*, 591.
- [17] Yin W. J., Shi T., Yan Y. *Adv. Mater.*, **2014**, *26*, 4653–4658.
- [18] Stoumpos C. C., Malliakas C. D., Kanatzidis M. G. *Inorg. Chem.*, **2013**, *52*, 9019–9038.
- [19] Stranks S. D., Eperon G. E., Grancini G., Menelaou C., Alcocer M. J. P., Leijtens T., Herz L. M., Petrozza A., Snaith H. J. *Science (80-.)*, **2013**, *342*, 341–344.
- [20] Sutton R. J., Eperon G. E., Miranda L., Parrott E. S., Kamino B. A., Patel J. B., Hörantner M. T., Johnston M. B., Haghighirad A. A., Moore D. T., Snaith H. J. *Adv. Energy Mater.*, **2016**, *6*, 1502458.
- [21] Nrel-Best Research-Cell Efficiencies (October 2020). <https://www.nrel.gov/pv/cell-efficiency.html>.
- [22] Kim G., Min H., Lee K. S., Lee D. Y., Yoon S. M., Seok S. Il. *Science (80-.)*, **2020**, *370*, 108–112.
- [23] Wang Y., Zhang T., Kan M., Zhao Y. *J. Am. Chem. Soc.*, **2018**, *140*, 12345–12348.
- [24] Heo J. H., Han H. J., Kim D., Ahn T. K., Im S. H. *Energy Environ. Sci.*, **2015**, *8*, 1602–1608.
- [25] Yang W. S., Noh J. H., Jeon N. J., Kim Y. C., Ryu S., Seo J., Seok S. Il. *Science (80-.)*, **2015**, *348*, 1234–1237.
- [26] Yi C., Luo J., Meloni S., Boziki A., Ashari-Astani N., Grätzel C., Zakeeruddin S. M., Röthlisberger U., Grätzel M. *Energy Environ. Sci.*, **2016**, *9*, 656–662.
- [27] Zhu T., Su J., Labat F., Ciofini I., Pauporté T. *ACS Appl. Mater. Interfaces*, **2020**, *12*, 744–752.
- [28] Yang M., Zhang T., Schulz P., Li Z., Li G., Kim D. H., Guo N., Berry J. J., Zhu K., Zhao Y. *Nat. Commun.*, **2016**, *7*, 12305.
- [29] Michael Saliba, Taisuke Matsui, Konrad Domanski, Ji-Youn Seo, Amita Ummadisingu, Shaik M. Zakeeruddin, Juan-Pablo Correa-Baena, Wolfgang R. Tress, Antonio Abate, Anders Hagfeldt M. G. *Science (80-.)*, **2016**, *354*, 206–210.
- [30] Saliba M., Matsui T., Seo J. Y., Domanski K., Correa-Baena J. P., Nazeeruddin M. K., Zakeeruddin S. M., Tress W., Abate A., Hagfeldt A., Grätzel M. *Energy Environ. Sci.*, **2016**, *9*, 1989–1997.

- [31] Turren-Cruz S. H., Hagfeldt A., Saliba M. *Science* (80-.), **2018**, *362*, 449–453.
- [32] Toscano C. D., Guilarte T. R. *Brain Res. Rev.*, **2005**, *49*, 529–554.
- [33] Jaishankar M., Tseten T., Anbalagan N., Mathew B. B., Beeregowda K. N. *Interdiscip. Toxicol.*, **2014**, *7*, 60–72.
- [34] Benmessaoud I. R., Mahul-Mellier A. L., Horváth E., Maco B., Spina M., Lashuel H. A., Forró L. *Toxicol. Res. (Camb.)*, **2016**, *5*, 407–419.
- [35] Finkelstein Y., Markowitz M. E., Rosen J. F. *Brain Res. Rev.*, **1998**, *27*, 168–176.
- [36] Abate A. *Joule*, **2017**, *1*, 659–664.
- [37] Li J., Cao H. L., Jiao W. Bin, Wang Q., Wei M., Cantone I., Lü J., Abate A. *Nat. Commun.*, **2020**, *11*, 11:310.
- [38] Nielsen P. K., Hemmingsen C., Friis S. U., Ladefoged J., Olgaard K. *Perit. Dial. Int.*, **1995**, *15*, 18–21.
- [39] Kieslich G., Sun S., Cheetham A. K. *Chem. Sci.*, **2014**, *5*, 4712–4715.
- [40] Sato T., Takagi S., Deledda S., Hauback B. C., Orimo S. I. *Sci. Rep.*, **2016**, *6*, 23592.
- [41] Fedorovskiy A. E., Drigo N. A., Nazeeruddin M. K. *Small Methods*, **2019**, *4*, 1900426.
- [42] Bartel C. J., Sutton C., Goldsmith B. R., Ouyang R., Musgrave C. B., Ghiringhelli L. M., Scheffler M. *Sci. Adv.*, **2019**, *5*, eaav0693.
- [43] Ke W., Stoumpos C. C., Kanatzidis M. G. *Adv. Mater.*, **2019**, *31*, 180323.
- [44] Chatterjee S., Dasgupta U., Pal A. J. *J. Phys. Chem. C*, **2017**, *121*, 20177–20187.
- [45] Yao E. P., Sun P., Huang W., Yao E. P., Yang Y., Wang M. *Nano Energy*, **2017**, *36*, 213–222.
- [46] Jahandar M., Heo J. H., Song C. E., Kong K. J., Shin W. S., Lee J. C., Im S. H., Moon S. J. *Nano Energy*, **2016**, *27*, 330–339.
- [47] Wang Z. K., Li M., Yang Y. G., Hu Y., Ma H., Gao X. Y., Liao L. S. *Adv. Mater.*, **2016**, *28*, 6695–6703.
- [48] Zhang H. yu, Li R., Liu W. wu, Zhang M., Guo M. *Int. J. Miner. Metall. Mater.*, **2019**, *26*, 387–403.
- [49] Nie R., Sumukam R. R., Reddy S. H., Banavoth M., Seok S. Il. *Energy Environ. Sci.*, **2020**, *13*, 2363–2385.
- [50] Abd Mutalib M., Ahmad Ludin N., Nik Ruzalman N. A. A., Barrioz V., Sepeai S., Mat Teridi M. A., Su'ait M. S., Ibrahim M. A., Sopian K. *Mater. Renew. Sustain. Energy*, **2018**, *7*, 7.
- [51] Xiao Z., Song Z., Yan Y. *Adv. Mater.*, **2019**, *31*, 1803792.

- [52] Gu S., Lin R., Han Q., Gao Y., Tan H., Zhu J. *Adv. Mater.*, **2020**, *32*, 1907392.
- [53] Kour R., Arya S., Verma S., Gupta J., Bandhoria P., Bharti V., Datt R., Gupta V. *Glob. Challenges*, **2019**, *3*, 1900050.
- [54] Wadi M. A. A., Chowdhury T. H., Bedja I. M., Lee J. J., Amin N., Aktharuzzaman M., Islam A. *Electron. Mater. Lett.*, **2019**, *15*, 525–546.
- [55] Liu C., Li W., Fan J., Mai Y. *J. Energy Chem.*, **2018**, *27*, 1054–1066.
- [56] Liang C., Li-wei Z., Yong-Sheng C. *Acta Phys. Sin.*, **2018**, *67*, 028801.
- [57] Scaife D. E., Weller P. F., Fisher W. G. *J. Solid State Chem.*, **1974**, *9*, 308–314.
- [58] Calabrese J., Jones N. L., Harlow R. L., Herron N., Thorn D. L., Wang Y. *J. Am. Chem. Soc.*, **1991**, *113*, 2328–2330.
- [59] Chung I., Song J. H., Im J., Androulakis J., Malliakas C. D., Li H., Freeman A. J., Kenney J. T., Kanatzidis M. G. *J. Am. Chem. Soc.*, **2012**, *134*, 8579–8587.
- [60] Lee B., Stoumpos C. C., Zhou N., Hao F., Malliakas C., Yeh C. Y., Marks T. J., Kanatzidis M. G., Chang R. P. H. *J. Am. Chem. Soc.*, **2014**, *136*, 15379–15385.
- [61] Takahashi Y., Hasegawa H., Takahashi Y., Inabe T. *J. Solid State Chem.*, **2013**, *205*, 39–43.
- [62] Mitzi D. B., Feild C. A., Harrison W. T. A., Guloy A. M. *Nature*, **1994**, *369*, 467.
- [63] Mitzi D. B., Feild C. A., Schlesinger Z., Laibowitz R. B. *J. Solid State Chem.*, **1995**, *114*, 159–163.
- [64] Liang K., Mitzi D. B., Prikas M. T. *Chem. Mater.*, **1998**, *10*, 403–411.
- [65] Chen Z., Wang J. J., Ren Y., Yu C., Shum K. *Appl. Phys. Lett.*, **2012**, *101*, 093901.
- [66] Hao F., Stoumpos C. C., Cao D. H., Chang R. P. H., Kanatzidis M. G. *Nat. Photonics*, **2014**, *8*, 489–494.
- [67] Noel N. K., Stranks S. D., Abate A., Wehrenfennig C., Guarnera S., Haghighirad A. A., Sadhanala A., Eperon G. E., Pathak S. K., Johnston M. B., Petrozza A., Herz L. M., Snaith H. J. *Energy Environ. Sci.*, **2014**, *7*, 3061–3068.
- [68] Liao W., Zhao D., Yu Y., Grice C. R., Wang C., Cimaroli A. J., Schulz P., Meng W., Zhu K., Xiong R. G., Yan Y. *Adv. Mater.*, **2016**, *28*, 9333–9340.
- [69] Yokoyama T., Cao D. H., Stoumpos C. C., Song T. Bin, Sato Y., Aramaki S., Kanatzidis M. G. *J. Phys. Chem. Lett.*, **2016**, *7*, 776–782.
- [70] Song T. Bin, Yokoyama T., Stoumpos C. C., Logsdon J., Cao D. H., Wasielewski M. R., Aramaki S., Kanatzidis M. G. *J. Am. Chem. Soc.*, **2017**, *139*, 836–842.
- [71] Yu Y., Zhao D., Grice C. R., Meng W., Wang C., Liao W., Cimaroli A. J., Zhang H.,

- Zhu K., Yan Y. *RSC Adv.*, **2016**, *6*, 90248–90254.
- [72] Jung M. C., Raga S. R., Qi Y. *RSC Adv.*, **2016**, *6*, 2819–2825.
- [73] Xi J., Wu Z., Jiao B., Dong H., Ran C., Piao C., Lei T., Song T. Bin, Ke W., Yokoyama T., Hou X., Kanatzidis M. G. *Adv. Mater.*, **2017**, *29*, 1–7.
- [74] Koh T. M., Krishnamoorthy T., Yantara N., Shi C., Leong W. L., Boix P. P., Grimsdale A. C., Mhaisalkar S. G., Mathews N. *J. Mater. Chem. A*, **2015**, *3*, 14996–15000.
- [75] Lee S. J., Shin S. S., Kim Y. C., Kim D., Ahn T. K., Noh J. H., Seo J., Seok S. Il. *J. Am. Chem. Soc.*, **2016**, *138*, 3974–3977.
- [76] Kumar M. H., Dharani S., Leong W. L., Boix P. P., Prabhakar R. R., Baikie T., Shi C., Ding H., Ramesh R., Asta M., Graetzel M., Mhaisalkar S. G., Mathews N. *Adv. Mater.*, **2014**, *26*, 7122–7127.
- [77] Zhao Z., Gu F., Li Y., Sun W., Ye S., Rao H., Liu Z., Bian Z., Huang C. *Adv. Sci.*, **2017**, *4*, 1700204.
- [78] Marshall K. P., Walker M., Walton R. I., Hatton R. A. *Nat. Energy*, **2016**, *1*, 16178.
- [79] Gupta S., Bendikov T., Hodes G., Cahen D. *ACS Energy Lett.*, **2016**, *1*, 1028–1033.
- [80] Handa T., Yamada T., Kubota H., Ise S., Miyamoto Y., Kanemitsu Y. *J. Phys. Chem. C*, **2017**, *121*, 16158–16165.
- [81] Ma L., Hao F., Stoumpos C. C., Phelan B. T., Wasielewski M. R., Kanatzidis M. G. *J. Am. Chem. Soc.*, **2016**, *138*, 14750–14755.
- [82] Li W., Li J., Li J., Fan J., Mai Y., Wang L. *J. Mater. Chem. A*, **2016**, *4*, 17104–17110.
- [83] Stoumpos C. C., Cao D. H., Clark D. J., Young J., Rondinelli J. M., Jang J. I., Hupp J. T., Kanatzidis M. G. *Chem. Mater.*, **2016**, *28*, 2852–2867.
- [84] Cao D. H., Stoumpos C. C., Yokoyama T., Logsdon J. L., Song T. Bin, Farha O. K., Wasielewski M. R., Hupp J. T., Kanatzidis M. G. *ACS Energy Lett.*, **2017**, *2*, 982–990.
- [85] Liao Y., Liu H., Zhou W., Yang D., Shang Y., Shi Z., Li B., Jiang X., Zhang L., Quan L. N., Quintero-Bermudez R., Sutherland B. R., Mi Q., Sargent E. H., Ning Z. *J. Am. Chem. Soc.*, **2017**, *139*, 6693–6699.
- [86] Stoumpos C. C., Mao L., Malliakas C. D., Kanatzidis M. G. *Inorg. Chem.*, **2017**, *56*, 56–73.
- [87] Shao S., Liu J., Portale G., Fang H. H., Blake G. R., ten Brink G. H., Koster L. J. A., Loi M. A. *Adv. Energy Mater.*, **2018**, *8*, 1702019.
- [88] Saparov B., Sun J. P., Meng W., Xiao Z., Duan H. S., Gunawan O., Shin D., Hill I. G., Yan Y., Mitzi D. B. *Chem. Mater.*, **2016**, *28*, 2315–2322.

- [89] Qiu X., Cao B., Yuan S., Chen X., Qiu Z., Jiang Y., Ye Q., Wang H., Zeng H., Liu J., Kanatzidis M. G. *Sol. Energy Mater. Sol. Cells*, **2017**, *159*, 227–234.
- [90] Lee B., Krenselewski A., Baik S. Il, Seidman D. N., Chang R. P. H. *Sustain. Energy Fuels*, **2017**, *1*, 710–724.
- [91] Du K. Z., Meng W., Wang X., Yan Y., Mitzi D. B. *Angew. Chemie - Int. Ed.*, **2017**, *56*, 8158–8162.
- [92] Slavney A. H., Hu T., Lindenberg A. M., Karunadasa H. I. *J. Am. Chem. Soc.*, **2016**, *138*, 2138–2141.
- [93] McClure E. T., Ball M. R., Windl W., Woodward P. M. *Chem. Mater.*, **2016**, *28*, 1348–1354.
- [94] Deng X. Z., Zhao Q. Q., Zhao Y. Q., Cai M. Q. *Curr. Appl. Phys.*, **2019**, *19*, 279–284.
- [95] Turkevych I., Kazaoui S., Ito E., Urano T., Yamada K., Tomiyasu H., Yamagishi H., Kondo M., Aramaki S. *ChemSusChem*, **2017**, *10*, 3754–3759.
- [96] Shao Z., Le Mercier T., Madec M. B., Pauporté T. *Mater. Lett.*, **2018**, *221*, 135–138.
- [97] Mandadapu U., Vedanayakam S. V., Thyagarajan K., Reddy M. R., Babu B. J. *Int. J. Renew. Energy Res.*, **2017**, *7*, 1604–1612.
- [98] Jokar E., Chien C. H., Tsai C. M., Fathi A., Diao E. W. G. *Adv. Mater.*, **2019**, *31*, 1804835.
- [99] Ran C., Gao W., Li J., Xi J., Li L., Dai J., Yang Y., Gao X., Dong H., Jiao B., Spanopoulos I., Malliakas C. D., Hou X., Kanatzidis M. G., Wu Z. *Joule*, **2019**, *3*, 3072–3087.
- [100] Wu T., Liu X., He X., Wang Y., Meng X., Noda T., Yang X., Han L. *Sci. China Chem.*, **2020**, *63*, 107–115.
- [101] Jiang X., Wang F., Wei Q., Li H., Shang Y., Zhou W., Wang C., Cheng P., Chen Q., Chen L., Ning Z. *Nat. Commun.*, **2020**, *11*, 1245.
- [102] Alberti A., Deretzis I., Mannino G., Smecca E., Giannazzo F., Listorti A., Colella S., Masi S., La Magna A. *Adv. Energy Mater.*, **2019**, *9*, 1803450.
- [103] Dang Y., Zhou Y., Liu X., Ju D., Xia S., Xia H., Tao X. *Angew. Chemie - Int. Ed.*, **2016**, *55*, 3447–3450.
- [104] Zhu Z., Chueh C. C., Li N., Mao C., Jen A. K. Y. *Adv. Mater.*, **2018**, *30*, 1703800.
- [105] Ke W., Stoumpos C. C., Zhu M., Mao L., Spanopoulos I., Liu J., Kontsevoi O. Y., Chen M., Sarma D., Zhang Y., Wasielewski M. R., Kanatzidis M. G. *Sci. Adv.*, **2017**, *3*, e1701293.

- [106] Ogomi Y., Morita A., Tsukamoto S., Saitho T., Fujikawa N., Shen Q., Toyoda T., Yoshino K., Pandey S. S., Ma T., Hayase S. *J. Phys. Chem. Lett.*, **2014**, *5*, 1004–1011.
- [107] Zuo F., Williams S. T., Liang P. W., Chueh C. C., Liao C. Y., Jen A. K. Y. *Adv. Mater.*, **2014**, *26*, 6454–6460.
- [108] Mosconi E., Umari P., De Angelis F. *J. Mater. Chem. A*, **2015**, *3*, 9208–9215.
- [109] Hao F., Stoumpos C. C., Chang R. P. H., Kanatzidis M. G. *J. Am. Chem. Soc.*, **2014**, *136*, 8094–8099.
- [110] Prasanna R., Gold-Parker A., Leijtens T., Conings B., Babayigit A., Boyen H. G., Toney M. F., McGehee M. D. *J. Am. Chem. Soc.*, **2017**, *139*, 11117–11124.
- [111] Mao L., Tsai H., Nie W., Ma L., Im J., Stoumpos C. C., Malliakas C. D., Hao F., Wasielewski M. R., Mohite A. D., Kanatzidis M. G. *Chem. Mater.*, **2016**, *28*, 7781–7792.
- [112] Liu H., Li X., Zeng Y., Meng L. *Comput. Mater. Sci.*, **2020**, *177*, 109576.
- [113] Yang Z., Rajagopal A., Jen A. K. Y. *Adv. Mater.*, **2017**, *29*, 1704418.
- [114] Liu M., Chen Z., Yang Y., Yip H. L., Cao Y. *J. Mater. Chem. A*, **2019**, *7*, 17324–17333.
- [115] Zhao B., Abdi-Jalebi M., Tabachnyk M., Glass H., Kamboj V. S., Nie W., Pearson A. J., Puttisong Y., Gödel K. C., Beere H. E., Ritchie D. A., Mohite A. D., Dutton S. E., Friend R. H., Sadhanala A. *Adv. Mater.*, **2017**, *29*, 1604744.
- [116] Li Y., Sun W., Yan W., Ye S., Rao H., Peng H., Zhao Z., Bian Z., Liu Z., Zhou H., Huang C. *Adv. Energy Mater.*, **2016**, *6*, 1601353.
- [117] Liu C., Fan J., Li H., Zhang C., Mai Y. *Sci. Rep.*, **2016**, *6*, 35705.
- [118] Liang J., Zhao P., Wang C., Wang Y., Hu Y., Zhu G., Ma L., Liu J., Jin Z. *J. Am. Chem. Soc.*, **2017**, *139*, 14009–14012.
- [119] Liao W., Zhao D., Yu Y., Shrestha N., Ghimire K., Grice C. R., Wang C., Xiao Y., Cimaroli A. J., Ellingson R. J., Podraza N. J., Zhu K., Xiong R. G., Yan Y. *J. Am. Chem. Soc.*, **2016**, *138*, 12360–12363.
- [120] Wang Y., Fu W., Yan J., Chen J., Yang W., Chen H. *J. Mater. Chem. A*, **2018**, *6*, 13090–13095.
- [121] Zhu L., Yuh B., Schoen S., Li X., Aldighaithir M., Richardson B. J., Alamer A., Yu Q. *Nanoscale*, **2016**, *8*, 7621–7630.
- [122] Tavakoli M. M., Zakeeruddin S. M., Grätzel M., Fan Z. *Adv. Mater.*, **2018**, *30*, 1705998.

- [123] Igual-Muñoz A. M., Castillo A., Dreessen C., Boix P. P., Bolink H. J. *ACS Appl. Energy Mater.*, **2020**, *3*, 2755–2761.
- [124] Tsai C. M., Wu H. P., Chang S. T., Huang C. F., Wang C. H., Narra S., Yang Y. W., Wang C. L., Hung C. H., Diao E. W. G. *ACS Energy Lett.*, **2016**, *1*, 1086–1093.
- [125] Lee S., Kang D. W. *ACS Appl. Mater. Interfaces*, **2017**, *9*, 22432–22439.
- [126] Yang Z., Rajagopal A., Chueh C. C., Jo S. B., Liu B., Zhao T., Jen A. K. Y. *Adv. Mater.*, **2016**, *28*, 8990–8997.
- [127] Kim G. Y., Oh S. H., Nguyen B. P., Jo W., Kim B. J., Lee D. G., Jung H. S. *J. Phys. Chem. Lett.*, **2015**, *6*, 2355–2362.
- [128] Li C., Song Z., Zhao D., Xiao C., Subedi B., Shrestha N., Junda M. M., Wang C., Jiang C. S., Al-Jassim M., Ellingson R. J., Podraza N. J., Zhu K., Yan Y. *Adv. Energy Mater.*, **2019**, *9*, 1803135.
- [129] Singh P., Ravindra N. M. *Sol. Energy Mater. Sol. Cells*, **2012**, *101*, 36–45.
- [130] Liu C., Li W., Li H., Zhang C., Fan J., Mai Y. *Nanoscale*, **2017**, *9*, 13967–13975.
- [131] Xu X., Chueh C. C., Yang Z., Rajagopal A., Xu J., Jo S. B., Jen A. K. Y. *Nano Energy*, **2017**, *34*, 392–398.
- [132] Ke W., Xiao C., Wang C., Saparov B., Duan H. S., Zhao D., Xiao Z., Schulz P., Harvey S. P., Liao W., Meng W., Yu Y., Cimaroli A. J., Jiang C. S., Zhu K., Al-Jassim M., Fang G., Mitzi D. B., Yan Y. *Adv. Mater.*, **2016**, *28*, 5214–5221.
- [133] Zhao D., Yu Y., Wang C., Liao W., Shrestha N., Grice C. R., Cimaroli A. J., Guan L., Ellingson R. J., Zhu K., Zhao X., Xiong R. G., Yan Y. *Nat. Energy*, **2017**, *2*, 17018.
- [134] Harvey S. P., Li Z., Christians J. A., Zhu K., Luther J. M., Berry J. J. *ACS Appl. Mater. Interfaces*, **2018**, *10*, 28541–28552.
- [135] Lian X., Chen J., Zhang Y., Qin M., Li J., Tian S., Yang W., Lu X., Wu G., Chen H. *Adv. Funct. Mater.*, **2019**, *29*, 1807024.
- [136] Tong J., Song Z., Kim D. H., Chen X., Chen C., Palmstrom A. F., Ndione P. F., Reese M. O., Dunfield S. P., Reid O. G., Liu J., Zhang F., Harvey S. P., Li Z., Christensen S. T., Teeter G., Zhao D., Al-Jassim M. M., Van Hest M. F. A. M., Beard M. C., Shaheen S. E., Berry J. J., Yan Y., Zhu K. *Science (80-.)*, **2019**, *364*, 475–479.
- [137] Zhou X., Zhang L., Wang X., Liu C., Chen S., Zhang M., Li X., Yi W., Xu B. *Adv. Mater.*, **2020**, *32*, 1908107.
- [138] Ulfa M., Wang P., Shao Z., Viana B., Pauporté T. *Proc SPIE*, **2018**, *10533*, 105332R–1.

- [139] Ulfa M., Wang P., Zhang J., Liu J., De Marcillac W. D., Coolen L., Peralta S., Pauporté T. *ACS Appl. Mater. Interfaces*, **2018**, *10*, 35118–35128.
- [140] Kapil G., Ripolles T. S., Hamada K., Ogomi Y., Bessho T., Kinoshita T., Chantana J., Yoshino K., Shen Q., Toyoda T., Minemoto T., Murakami T. N., Segawa H., Hayase S. *Nano Lett.*, **2018**, *18*, 3600–3607.
- [141] Minemoto T., Matsui T., Takakura H., Hamakawa Y., Negami T., Hashimoto Y., Uenoyama T., Kitagawa M. *Sol. Energy Mater. Sol. Cells*, **2001**, *67*, 83–88.
- [142] Sharbati S., Sites J. R. *IEEE J. Photovoltaics*, **2014**, *4*, 697–702.
- [143] Minemoto T., Murata M. *Sol. Energy Mater. Sol. Cells*, **2015**, *133*, 8–14.
- [144] Dong J., Shi J., Li D., Luo Y., Meng Q. *Appl. Phys. Lett.*, **2015**, *107*, 073507.
- [145] Bui T. T., Ulfa M., Maschietto F., Ottochian A., Nghiêm M. P., Ciofini I., Goubard F., Pauporté T. *Org. Electron.*, **2018**, *60*, 22–30.
- [146] Ulfa M., Pauporté T., Bui T. T., Goubard F. *J. Phys. Chem. C*, **2018**, *122*, 11651–11658.
- [147] Ulfa M., Zhu T., Goubard F., Pauporté T. *J. Mater. Chem. A*, **2018**, *6*, 13350–13358.
- [148] Magaldi D., Ulfa M., Nghiêm M. P., Sini G., Goubard F., Pauporté T., Bui T. T. *J. Mater. Sci.*, **2020**, *55*, 4820–4829.
- [149] Cui Y., Xu B., Yang B., Yao H., Li S., Hou J. *Macromolecules*, **2016**, *49*, 8126–8133.
- [150] Zhou X., Hu M., Liu C., Zhang L., Zhong X., Li X., Tian Y., Cheng C., Xu B. *Nano Energy*, **2019**, *63*, 103866.
- [151] Shao S., Cui Y., Duim H., Qiu X., Dong J., ten Brink G. H., Portale G., Chiechi R. C., Zhang S., Hou J., Loi M. A. *Adv. Mater.*, **2018**, *30*, 1803703.
- [152] Song J., Hu W., Li Z., Wang X. F., Tian W. *Sol. Energy Mater. Sol. Cells*, **2020**, *207*, 110351.
- [153] Hamada K., Tanaka R., Kamarudin M. A., Shen Q., Iikubo S., Minemoto T., Yoshino K., Toyoda T., Ma T., Kang D.-W., Hayase S. *ACS Appl. Mater. Interfaces*, **2020**, *12*, 17776–17782.
- [154] Pazoki M., Jacobsson T. J., Hagfeldt A., Boschloo G., Edvinsson T. *Phys. Rev. B*, **2016**, *93*, 144105.
- [155] Jacobsson T. J., Pazoki M., Hagfeldt A., Edvinsson T. *J. Phys. Chem. C*, **2015**, *119*, 25673–25683.
- [156] Kai W., Liang W. *Acta Phys. -Chim. Sin.*, **2015**, *31*, 285–290.
- [157] Lau C. F. J., Zhang M., Deng X., Zheng J., Bing J., Ma Q., Kim J., Hu L., Green M.

- A., Huang S., Ho-Baillie A. *ACS Energy Lett.*, **2017**, *2*, 2319–2325.
- [158] Wu M., Lin T., Chan S., Liao Y., Chang Y. *ACS Appl. Energy Mater.*, **2018**, *1*, 4849–4859.
- [159] Zhang H., Liu W., Li R., Zhang M., Guo M. *Ceram. Int.*, **2018**, *44*, 18863–18870.
- [160] Zhang H., Li R., Zhang M., Guo M. *Inorg. Chem. Front.*, **2018**, *5*, 1354–1364.
- [161] Li R., Zhang H., Han X., Huo X., Zhang M., Guo M. *ACS Appl. Mater. Interfaces*, **2020**, *12*, 10515–10526.
- [162] Zhang J., Pauporté T. *ChemPhysChem*, **2015**, *16*, 2836–2841.
- [163] Zhang H., Li R., Zhang M., Guo M. *Ceram. Int.*, **2020**, *46*, 14038–14047.
- [164] Pérez-del-Rey D., Forgács D., Hutter E. M., Savenije T. J., Nordlund D., Schulz P., Berry J. J., Sessolo M., Bolink H. J. *Adv. Mater.*, **2016**, *28*, 9839–9845.
- [165] Zhang H., Wang H., Williams S. T., Xiong D., Zhang W., Chueh C. C., Chen W., Jen A. K. Y. *Adv. Mater.*, **2017**, *29*, 1606608.
- [166] Caprioglio P., Zu F., Wol M., Stolterfoht M., Becker P., Koch N., Unold T., Rech B., Neher D. *Sustain. Energy Fuels*, **2019**, *3*, 550–563.
- [167] Kumar A., Balasubramaniam K. R., Kangsabanik J., Vikram, Alam A. *Phys. Rev. B*, **2016**, *94*, 180105.
- [168] Chan S. H., Wu M. C., Lee K. M., Chen W. C., Lin T. H., Su W. F. *J. Mater. Chem. A*, **2017**, *5*, 18044–18052.
- [169] Wu M. C., Chen W. C., Chan S. H., Su W. F. *Appl. Surf. Sci.*, **2018**, *429*, 9–15.
- [170] Xiang W., Wang Z., Kubicki D. J., Wang X., Tress W., Luo J., Zhang J., Hofstetter A., Zhang L., Emsley L., Grätzel M., Hagfeldt A. *Nat. Commun.*, **2019**, *10*, 4686.
- [171] Zhang H., Shang M. hui, Zheng X., Zeng Z., Chen R., Zhang Y., Zhang J., Zhu Y. *Electrochim. Acta*, **2017**, *254*, 165–171.
- [172] Uribe J. I., Ramirez D., Osorio-Guillén J. M., Osorio J., Jaramillo F. *J. Phys. Chem. C*, **2016**, *120*, 16393–16398.
- [173] Wu M. C., Lin T. H., Chan S. H., Su W. F. *J. Taiwan Inst. Chem. Eng.*, **2017**, *80*, 695–700.
- [174] Lau C. F. J., Deng X., Zheng J., Kim J., Zhang Z., Zhang M., Bing J., Wilkinson B., Hu L., Patterson R., Huang S., Ho-Baillie A. *J. Mater. Chem. A*, **2018**, *6*, 5580–5586.
- [175] Klug M. T., Osherov A., Haghghirad A. A., Stranks S. D., Brown P. R., Bai S., Wang J. T. W., Dang X., Bulović V., Snaith H. J., Belcher A. M. *Energy Environ. Sci.*, **2017**, *10*, 236–246.

- [176] Chen Q., Chen L., Ye F., Zhao T., Tang F., Rajagopal A., Jiang Z. *Nano Lett.*, **2017**, *17*, 3231–3237.
- [177] Liang J., Liu Z., Qiu L., Hawash Z., Meng L., Wu Z., Jiang Y., Ono L. K., Qi Y. *Adv. Energy Mater.*, **2018**, *8*, 1800504.
- [178] Jin J., Li H., Chen C., Zhang B., Xu L., Dong B., Song H., Dai Q. *ACS Appl. Mater. Interfaces*, **2017**, *9*, 42875–42882.
- [179] Sa R., Wang L., Wang J., Chen X., Chen J., Lou B. *Appl. Phys. Express*, **2019**, *12*, 082011.
- [180] Stoumpos C. C., Frazer L., Clark D. J., Kim Y. S., Rhim S. H., Freeman A. J., Ketterson J. B., Jang J. I., Kanatzidis M. G. *J. Am. Chem. Soc.*, **2015**, *137*, 6804–6819.
- [181] Krishnamoorthy T., Ding H., Yan C., Leong W. L., Baikie T., Zhang Z., Sherburne M., Li S., Asta M., Mathews N., Mhaisalkar S. G. *J. Mater. Chem. A*, **2015**, *3*, 23829–23832.
- [182] Kopacic I., Friesenbichler B., Hoefler S. F., Kunert B., Plank H., Rath T., Trimmel G. *ACS Appl. Energy Mater.*, **2018**, *1*, 343–347.
- [183] Ng C. H., Hamada K., Kapil G., Kamarudin M. A., Wang Z., Shen Q., Yoshino K., Minemoto T., Hayase S. *J. Mater. Chem. A*, **2020**, *8*, 2962–2968.
- [184] Ito N., Kamarudin M. A., Hirotani D., Zhang Y., Shen Q., Ogomi Y., Iikubo S., Minemoto T., Yoshino K., Hayase S. *J. Phys. Chem. Lett.*, **2018**, *9*, 1682–1688.
- [185] Sun P. P., Li Q. S., Feng S., Li Z. S. *Phys. Chem. Chem. Phys.*, **2016**, *18*, 14408–14418.
- [186] Yang F., Hirotani D., Kapil G., Kamarudin M. A., Ng C. H., Zhang Y., Shen Q., Hayase S. **2018**, 8585, 12745–12749.
- [187] Kim G. M., Ishii A., Öz S., Miyasaka T. *Adv. Energy Mater.*, **2020**, *10*, 1903299.
- [188] McCall K. M., Stoumpos C. C., Kostina S. S., Kanatzidis M. G., Wessels B. W. *Chem. Mater.*, **2017**, *29*, 4129–4145.
- [189] Adonin S. A., Frolova L. A., Sokolov M. N., Shilov G. V., Korchagin D. V., Fedin V. P., Aldoshin S. M., Stevenson K. J., Troshin P. A. *Adv. Energy Mater.*, **2018**, *8*, 1701140.
- [190] Boopathi K. M., Karuppuswamy P., Singh A., Hanmandlu C., Lin L., Abbas S. A., Chang C. C., Wang P. C., Li G., Chu C. W. *J. Mater. Chem. A*, **2017**, *5*, 20843–20850.
- [191] Hebig J. C., Kühn I., Flohre J., Kirchartz T. *ACS Energy Lett.*, **2016**, *1*, 309–314.
- [192] Zhang J., Shang M. H., Wang P., Huang X., Xu J., Hu Z., Zhu Y., Han L. *ACS Energy*

- Lett.*, **2016**, *1*, 535–541.
- [193] Oku T., Ohishi Y., Suzuki A. *Chem. Lett.*, **2016**, *45*, 134–136.
- [194] Shao Z., Le Mercier T., Madec M. B., Pauporté T. *Mater. Des.*, **2018**, *141*, 81–87.
- [195] Hu Y., Bai F., Liu X., Ji Q., Miao X., Qiu T., Zhang S. *ACS Energy Lett.*, **2017**, *2*, 2219–2227.
- [196] Li M., Wang Z. K., Zhuo M. P., Hu Y., Hu K. H., Ye Q. Q., Jain S. M., Yang Y. G., Gao X. Y., Liao L. S. *Adv. Mater.*, **2018**, *30*, 1800258.
- [197] Liu D., Li Q., Hu J., Sa R., Wu K. *J. Phys. Chem. C*, **2019**, *123*, 12638–12646.
- [198] Mao L., Stoumpos C. C., Kanatzidis M. G. *J. Am. Chem. Soc.*, **2019**, *141*, 1171–1190.
- [199] Mercier N. *Angew. Chemie - Int. Ed.*, **2019**, *58*, 17912–17917.
- [200] Leblanc A. *Thèse de l'Université d'Angers*, **2019**, 1–220.
- [201] Mercier N., Leblanc A., Pauporté T. Brevet International_Janv19.Pdf. 2019, p WO 2019/016476 A1.
- [202] Leblanc A., Mercier N., Allain M., Dittmer J., Pauporté T., Fernandez V., Boucher F., Kepenekian M., Katan C. *ACS Appl. Mater. Interfaces*, **2019**, *11*, 20743–20751.
- [203] Leblanc A., Mercier N., Allain M., Dittmer J., Fernandez V., Pauporté T. *Angew. Chemie - Int. Ed.*, **2017**, *56*, 16067–16072.
- [204] Ke W., Priyanka P., Vegiraju S., Stoumpos C. C., Spanopoulos I., Soe C. M. M., Marks T. J., Chen M. C., Kanatzidis M. G. *J. Am. Chem. Soc.*, **2018**, *140*, 388–393.
- [205] Ke W., Stoumpos C. C., Spanopoulos I., Mao L., Chen M., Wasielewski M. R., Kanatzidis M. G. *J. Am. Chem. Soc.*, **2017**, *139*, 14800–14806.
- [206] Spanopoulos I., Ke W., Stoumpos C. C., Schueller E. C., Kontsevoi O. Y., Seshadri R., Kanatzidis M. G. *J. Am. Chem. Soc.*, **2018**, *140*, 5728–5742.
- [207] Ke W., Spanopoulos I., Tu Q., Hadar I., Li X., Shekhawat G. S., Dravid V. P., Kanatzidis M. G. *J. Am. Chem. Soc.*, **2019**, *141*, 8627–8637.
- [208] Zheng Y., Su R., Xu Z., Luo D., Dong H., Jiao B., Wu Z., Gong Q., Zhu R. *Sci. Bull.*, **2019**, *64*, 1255–1261.
- [209] Kovalsky A., Burda C. *Semicond. Sci. Technol.*, **2016**, *31*, 073001.
- [210] Barugkin C., Beck F. J., Catchpole K. R. *J. Opt.*, **2017**, *19*, 014001.
- [211] Zhang W., Saliba M., Stranks S. D., Sun Y., Shi X., Wiesner U., Snaith H. J. Enhancement of Perovskite-Based Solar Cells Employing Core-Shell Metal Nanoparticles. *Nano Letters*. 2013, pp 4505–4510.
- [212] Carretero-Palacios S., Jiménez-Solano A., Míguez H. *ACS Energy Lett.*, **2016**, *1*, 323–

331.

- [213] Wang R., Mujahid M., Duan Y., Wang Z. K., Xue J., Yang Y. *Adv. Funct. Mater.*, **2019**, *29*, 1808843.
- [214] Tsai H., Nie W., Blancon J., Stoumpos C. C., Asadpour R., Harutyunyan B., Neukirch A. J., Verduzco R., Crochet J. J., Tretiak S., Pedesseau L., Even J., Alam M. A., Gupta G., Lou J., Ajayan P. M., Bedzyk M. J., Kanatzidis M. G., Mohite A. D. *Nature*, **2016**, *536*, 312–326.
- [215] You J., Meng L., Song T., Guo T., Yang Y. M., Chang W., Hong Z., Chen H., Zhou H., Chen Q., Liu Y., Marco N. De. **2016**, *11*, 75–82.
- [216] Arora N., Dar M. I., Hinderhofer A., Pellet N., Schreiber F., Zakeeruddin S. M., Grätzel M. *Science (80-.)*, **2017**, *358*, 768–771.
- [217] Wang Z., Lin Q., Chmiel F. P., Sakai N., Herz L. M., Snaith H. J. *Nat. Energy*, **2017**, *2*, 17135.
- [218] Bella F., Griffini G., Correa-Baena J. P., Saracco G., Grätzel M., Hagfeldt A., Turri S., Gerbaldi C. *Science (80-.)*, **2016**, *354*, 203–206.
- [219] Leijtens T., Bush K. A., Prasanna R., McGehee M. D. *Nat. Energy*, **2018**, *3*, 828–838.
- [220] Hörantner M. T., Leijtens T., Ziffer M. E., Eperon G. E., Christoforo M. G., McGehee M. D., Snaith H. J. *ACS Energy Lett.*, **2017**, *2*, 2506–2513.
- [221] Zhao D., Chen C., Wang C., Junda M. M., Song Z., Grice C. R., Yu Y., Li C., Subedi B., Podraza N. J., Zhao X., Fang G., Xiong R. G., Zhu K., Yan Y. *Nat. Energy*, **2018**, *3*, 1093–1100.
- [222] Eperon G. E., Hörantner M. T., Snaith H. J. *Nat. Rev. Chem.*, **2017**, *1*, 0095.
- [223] Chen P. Y., Qi J., Klug M. T., Dang X., Hammond P. T., Belcher A. M. *Energy Environ. Sci.*, **2014**, *7*, 3659–3665.
- [224] Li C., Zhu Z., Wang Y., Guo Q., Wang C., Zhong P., Tan Z., Yang R. *Nano Energy*, **2020**, *69*.
- [225] Binek A., Petrus M. L., Huber N., Bristow H., Hu Y., Bein T., Docampo P. *ACS Appl. Mater. Interfaces*, **2016**, *8*, 12881–12886.
- [226] Xu J., Hu Z., Huang L., Huang X., Jia X., Zhang J., Zhang J., Zhu Y. *Prog. Photovoltaics Res. Appl.*, **2017**, *25*, 1022–1033.
- [227] Chhillar P., Dhamaniya B. P., Dutta V., Pathak S. K. *ACS Omega*, **2019**, *4*, 11880–11887.

This article must be cited as:

L. Gollino, T. Pauporté, Lead-Less Halide Perovskite Solar Cells

Sol. RRL **2021**, *5*, 2000616 DOI: 10.1002/solr.202000616

WILEY-VCH

This article must be cited as:

L. Gollino, T. Pauporté, Lead-Less Halide Perovskite Solar Cells
Sol. RRL **2021**, *5*, 2000616 DOI: 10.1002/solr.202000616

WILEY-VCH

Table 1. Photovoltaic parameters of the Sn-Pb-based lead-less PSCs with their perovskite materials, deposition methods and device architectures.

This article must be cited as:

L. Gollino, T. Pauporté, Lead-Less Halide Perovskite Solar Cells

Sol. RRL **2021**, *5*, 2000616 DOI: 10.1002/solr.202000616

WILEY-VCH

Perovskite	Sn Content [%]	Deposition method	Architecture	V _{oc} [V]	J _{sc} [mA/cm ²]	FF [%]	PCE [%]	Year	Ref
CsPb _{0.9} Sn _{0.1} Br ₂	10	Two-step	FTO/c-TiO ₂ /m-TiO ₂ /perovskite/carbon	1.26	14.3	63	11.33	2017	118
MASn _{0.1} Pb _{0.9} I ₃	10	DMSO vapor-assisted	ITO/PEDOT:PSS/perovskite/PCBM/BCP/Al	0.78	19	67.1	9.95	2016	121
MAPb _{0.85} Sn _{0.15} I _{3-x} Cl _x	15	One-step	ITO/PEDOT:PSS/perovskite/PCBM/C ₆₀ -bis/Ag	0.77	19.5	67	10.1	2014	107
MAPb _{0.75} Sn _{0.25} I ₃	25	One-step	FTO/c-TiO ₂ /m-TiO ₂ /perovskite/spiro-OMeTAD/Au	0.728	15.82	64.01	7.37	2014	109
MAPb _{0.75} Sn _{0.25} I ₃	25	Two-step	FTO/PEDOT:PSS/perovskite/PCBM/BCP/Ag	0.745	23.8	78.56	13.93	2016	117
MAPb _{0.75} Sn _{0.25} I ₃ + 0.05 mg/mL C ₆₀	25	Two-step	FTO/PEDOT:PSS/perovskite/PCBM/BCP/Ag	0.736	23.5	79	13.7	2017	130
MA _{0.9} Cs _{0.1} Sn _{0.25} Pb _{0.75} I ₃	25	Thermal evaporation	ITO/MoO ₃ /m-MTDATA/perovskite/C ₆₀ /BCP/Ag	0.677	25	53	8.9	2020	123
FA _{0.7} MA _{0.3} Pb _{0.7} Sn _{0.3} I ₃	30	Two-step	ITO/PTAA/perovskite/PCBM/ZnO/Al	0.78	23.6	74	13.6	2018	120
FAPb _{0.7} Sn _{0.3} I ₃ + 0.25 MASCN	30	Two-step	ITO/PEDOT:PSS/perovskite/PEAI/PCBM/BCP/Ag	0.78	26.46	79	16.26	2019	135
MASn _{0.3} Pb _{0.7} I ₃	30	Dripping	FTO/c-TiO ₂ /m-TiO ₂ /C ₆₀ -COOH/perovskite/spiro-OMeTAD/Au	0.49	27.06	59	7.92	2020	153
FA _{0.7} MA _{0.3} Pb _{0.7} Sn _{0.3} I ₃ + 12% GABr + 0.03 mmol SnF ₂	30	Dripping	ITO/EMIC-PEDOT:PSS/perovskite/S-acetylthiocholine chloride C ₆₀ /BCP/Ag	1.02	26.61	76	20.63	2020	137
MAPb _{0.6} Sn _{0.4} I ₃	40	One-step	ITO/PEDOT:PSS/perovskite/PCBM/Al	0.767	20.5	63.1	10	2017	115
MASn _{0.5} Pb _{0.5} I ₃	50	One-step	FTO/c-TiO ₂ /m-TiO ₂ /perovskite/P3HT/Au	0.42	20.04	50	4.18	2014	106
MASn _{0.5} Pb _{0.5} I ₃	50	Two-step	ITO/PEDOT:PSS/perovskite/C ₆₀ /BCP/Ag	0.75	24.9	68.8	13.6	2016	116
MASn _{0.5} Pb _{0.5} I ₃ + 10 mol% ascorbic acid	50	Dripping	ITO/PEDOT:PSS/perovskite/PCBM/bis-C ₆₀ /Ag	0.78	25.69	70	14.01	2017	131
FA _{0.5} MA _{0.5} Sn _{0.5} Pb _{0.5} I ₃ + 10 mol% SnF ₂	50	Dripping	ITO/PEDOT:PSS/perovskite/PCBM (5 mg/mL)/C ₆₀ /PCBM/Ag	0.75	30.56	76	17.59	2018	140
FASn _{0.5} Pb _{0.5} I ₃ + 10 mol% SnF ₂	50	Dripping	ITO/PCP-Na/perovskite/C ₆₀ /BCP/Al	0.782	28.1	73	16.27	2018	151
FA _{0.5} MA _{0.5} Sn _{0.5} Pb _{0.5} I ₃ + 10 mol% SnF ₂	50	Dripping	ITO/PEDOT:PSS/perovskite/PCBM/ZnO/Ag	0.79	28.9	79.3	18.1	2019	114
(FASnI ₃) _{0.6} (MAPbI ₃) _{0.4} + 10 mol% SnF ₂	60	Dripping	ITO/PEDOT:PSS/perovskite/C ₆₀ /BCP/Ag	0.795	26.86	70.6	15.08	2016	119
MA _{0.4} FA _{0.6} Sn _{0.6} Pb _{0.4} I ₃ + 20 mol% SnF ₂	60	Dripping	ITO/PEDOT:PSS/perovskite/C ₆₀ /BCP/Ag	0.83	27.3	80	18.2	2017	110
MASn _{0.6} Pb _{0.4} I _{2.6} Br _{0.4} + 10 mol% SnF ₂	60	Dripping	ITO/PEDOT:PSS/perovskite/PCBM/Ag	0.78	20.65	75	12.1	2017	125
(FASnI ₃) _{0.6} (MAPbI ₃) _{0.34} (MAPbBr ₃) _{0.06} + 10 mol% SnF ₂	60	Dripping	ITO/PEDOT:PSS/perovskite/C ₆₀ /BCP/Ag	0.888	28.72	74.6	19.03	2019	128
(FASnI ₃) _{0.6} (MAPbI ₃) _{0.4} + 7% GuaSCN	60	Dripping	ITO/PEDOT:PSS/perovskite/C ₆₀ /BCP/Ag	0.842	30.5	80	20.2	2019	136
(FASnI ₃) _{0.6} (MAPbI ₃) _{0.4} + 10 mol% SnF ₂	60	Dripping	ITO/CuI (10 mg/mL)/PEDOT:PSS/perovskite/C ₆₀ /BCP/Cu	0.75	28.5	73.7	15.75	2020	152
MAPb _{0.38} Sn _{0.62} I ₃	62	Thermal evaporation + CVD	ITO/TiO ₂ /perovskite/spiro-OMeTAD/Au	0.796	25.5	69.2	14.04	2018	122
MASn _{0.75} Pb _{0.25} I _{3-x} Cl _x + 30 mol% SnF ₂	75	One-step	FTO/c-TiO ₂ /m-TiO ₂ /perovskite/Al ₂ O ₃ /carbon	0.366	23.01	47.8	4.03	2016	124
PEA _{0.15} FA _{0.85} SnI ₃ + SnF ₂ doping	100	Dripping	ITO/PEDOT:PSS/perovskite/ICBA/BCP/Ag	0.94	17.4	75	12.4	2020	101

This article must be cited as:

L. Gollino, T. Pauporté, Lead-Less Halide Perovskite Solar Cells
Sol. RRL **2021**, *5*, 2000616 DOI: 10.1002/solr.202000616

WILEY-VCH

Table 2. Photovoltaic parameters of the lead-less PSCs mentioned in section 3 and 4 with their perovskite materials, deposition methods and device architectures.

This article must be cited as:

L. Gollino, T. Pauporté, Lead-Less Halide Perovskite Solar Cells

Sol. RRL **2021**, *5*, 2000616 DOI: 10.1002/solr.202000616

WILEY-VCH

Perovskite	Substituent amount [%]	Deposition method	Architecture	V _{oc} [V]	J _{sc} [mA/cm ²]	FF [%]	PCE [%]	Year	Ref
MAPb _{0.995} Ag _{0.005} I ₃	0.5	Dripping	ITO/NiOx/perovskite/PCBM/Ag	1.1	20.6	81	18.4	2017	176
CsPb _{0.995} Mn _{0.005} 1.01Br _{1.99}	0.5	Two-step	FTO/TiO ₂ /perovskite/carbon	0.99	13.15	57	7.36	2018	177
MAPb _{0.99} Sb _{0.01} I ₃	1	Not precised	FTO/c-TiO ₂ /m-TiO ₂ /perovskite/spiro-OMeTAD/Au	0.985	21.82	69.2	15.6	2016	192
MAPb _{0.99} Ca _{0.01} I ₃	1	One-step	FTO/TiO ₂ /perovskite/spiro-OMeTAD/Au	0.98	19.1	68.4	12.9	2017	173
MAPbCol ₃ (Pb:Co ratio of 63:1)	~1	One-step	ITO/PEDOT:PSS/perovskite/Ca-BCP/Al-Ag	1.05	21.1	77.7	17.2	2017	175
MAPb _{0.99} Sr _{0.01} I ₃	1	Not precised	FTO/TiO ₂ /perovskite/spiro-OMeTAD/Ag	0.9	18.9	62.6	10.6	2018	158
MAPb _{0.99} Ba _{0.01} I ₃	1	One-step	FTO/TiO ₂ /perovskite/spiro-OMeTAD/Au	0.98	19.6	67.8	13	2018	169
CsPb _{0.98} Sr _{0.02} 2I ₂ Br	2	Vapor-assisted	FTO/c-TiO ₂ /m-TiO ₂ /perovskite/P3HT/Au	1.043	15.3	69.9	11.2	2017	157
MAPb _{0.97} Sb _{0.03} I ₃	3	One-step	FTO/c-TiO ₂ /m-TiO ₂ /perovskite/spiro-OMeTAD/Au	0.843	19.2	56	9.07	2016	193
MAPb _{0.97} Ba _{0.03} I ₃	3	One-step	FTO/TiO ₂ /perovskite/spiro-OMeTAD/Au	0.99	20.4	69.6	14.9	2017	168
MA(PbI ₂) _{0.97} (ZnCl ₂) _{0.03}	3	Dripping	FTO/TiO ₂ /perovskite/spiro-OMeTAD/Au	1.09	22.04	75.76	18.2	2017	178
FA _{0.87} MA _{0.13} Pb _{0.97} Ge _{0.03} (I _{0.9} Br _{0.1}) ₃	3	Dripping	FTO/TiO ₂ /SnO ₂ /perovskite/spiro-OMeTAD/Au	1.14	24.98	77	22.09	2020	187
CsPb _{0.96} Bi _{0.04} I ₃	4	One-step	FTO/TiO ₂ /perovskite/CuI/Au	0.97	18.76	72.59	13.21	2017	195
MA(PbI ₂) _{0.95} (CuBr ₂) _{0.05}	5	Dripping	ITO/PEDOT:PSS/perovskite/PCBM/LiF/Al	0.961	21.51	82.6	17.09	2016	46
MASr _{0.05} Pb _{0.95} 1.95Cl _{0.05}	5	Two-step	ITO/c-TiO ₂ /m-TiO ₂ /perovskite/spiro-OMeTAD/Au	1.11	21.08	71	16.3	2017	45
CsPb _{0.95} Ca _{0.05} I ₃	5	Vapor-assisted	FTO/c-TiO ₂ /m-TiO ₂ /perovskite/P3HT/Au/MgF ₂	0.95	17.9	80	13.5	2019	174
MAPb _{0.95} Sr _{0.05} 1.95Cl _{0.05}	5	Two-step	FTO/TiO ₂ nanorod arrays/perovskite/spiro-OMeTAD/Au	1.02	19.96	75	16.08	2020	161
MAPb _{0.92} Sb _{0.08} I ₃	8	Two-step	ITO/NiOx/perovskite/PCBM/Al	1.13	17.4	65	12.8	2017	44
MASr _{0.1} Pb _{0.9} I ₃	10	One-step	FTO/c-TiO ₂ /m-TiO ₂ /perovskite/spiro-OMeTAD/Ag	0.87	4.32	53	1.97	2015	156
MAPb _{0.9} Sr _{0.1} 2.9Cl _{0.1}	10	Two-step	FTO/c-TiO ₂ /m-TiO ₂ /perovskite/spiro-OMeTAD/Au	1.08	19.45	74	15.64	2018	159
MAPb _{0.9} Sn _{0.1} I ₃	10	Two-step	FTO/c-TiO ₂ /m-TiO ₂ /perovskite/spiro-OMeTAD/Au	1.06	20.32	72	15.52	2018	160
MAPb _{0.9} Sn _{0.05} Cu _{0.05} 1.9Br _{0.1}	10	Dripping	FTO/TiO ₂ /perovskite/MoO ₃ /Ag	1.08	23.97	81	21.08	2018	196
MAPb _{0.85} In _{0.15} 1.85Cl _{0.15}	15	One-step	ITO/PEDOT:PSS/perovskite/PCBM/Bphen/Ag	1.03	21.9	78	17.55	2016	47
CsPb _{0.8} Ge _{0.2} 2I ₂ Br	20	Dripping	FTO/SnO ₂ /perovskite/P3HT/spiro-OMeTAD/Au	1.27	12.15	70.1	10.8	2018	186
CsPb _{0.8} Ba _{0.2} 2I ₂ Br	20	One-step	FTO/c-TiO ₂ /m-TiO ₂ /perovskite/spiro-OMeTAD/Au	14	1.28	78.2	14	2019	170
MAPbI ₃ :Sr ₂₊ (2% doping)	/	One-step	FTO/PEDOT:PSS/perovskite/IPH/Ba-Ag	≈0.95	≈18.5	≈85	≈15	2016	164
MAPbI ₂ Br(SrCl ₂) _{0.1} (doping)	/	One-step	FTO/c-TiO ₂ /m-TiO ₂ /perovskite/m-Al ₂ O ₃ /carbon	1.05	20.2	75	15.9	2017	165
Rb _{0.05} (Cs _{0.05} (MA _{0.17} FA _{0.83}) _{0.95}) _{0.95} Pb(I _{0.83} Br _{0.17}) ₃ (2% Sr doping)	/	Dripping	ITO/PTAA/perovskite/C ₆₀ /BCP/Cu	1.18	23.2	74	20.3	2019	166



Figure 1. Schematic of the different structures of direct mesoscopic, direct normal planar and inverted planar PSCs.

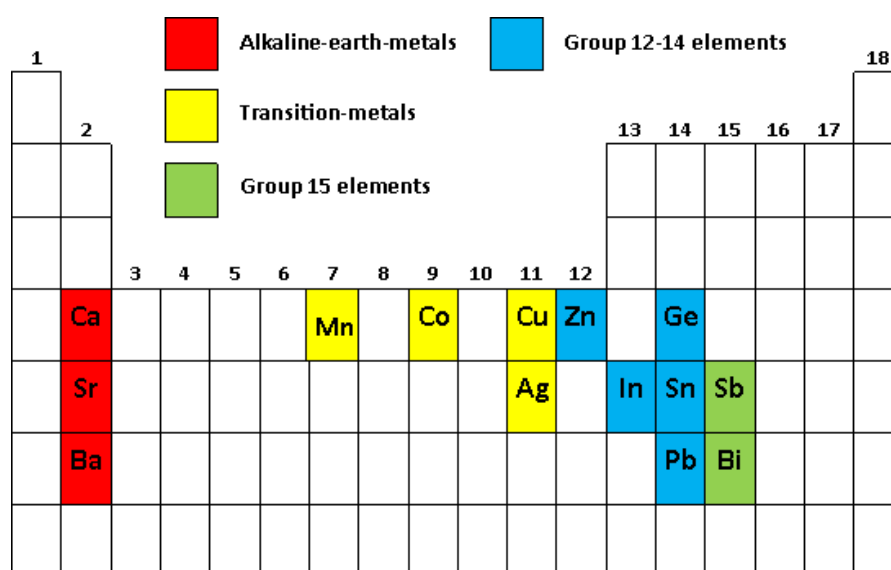


Figure 2. Mendeleev periodic table highlighting elements reported in this review to substitute Pb in lead-less PSCs.

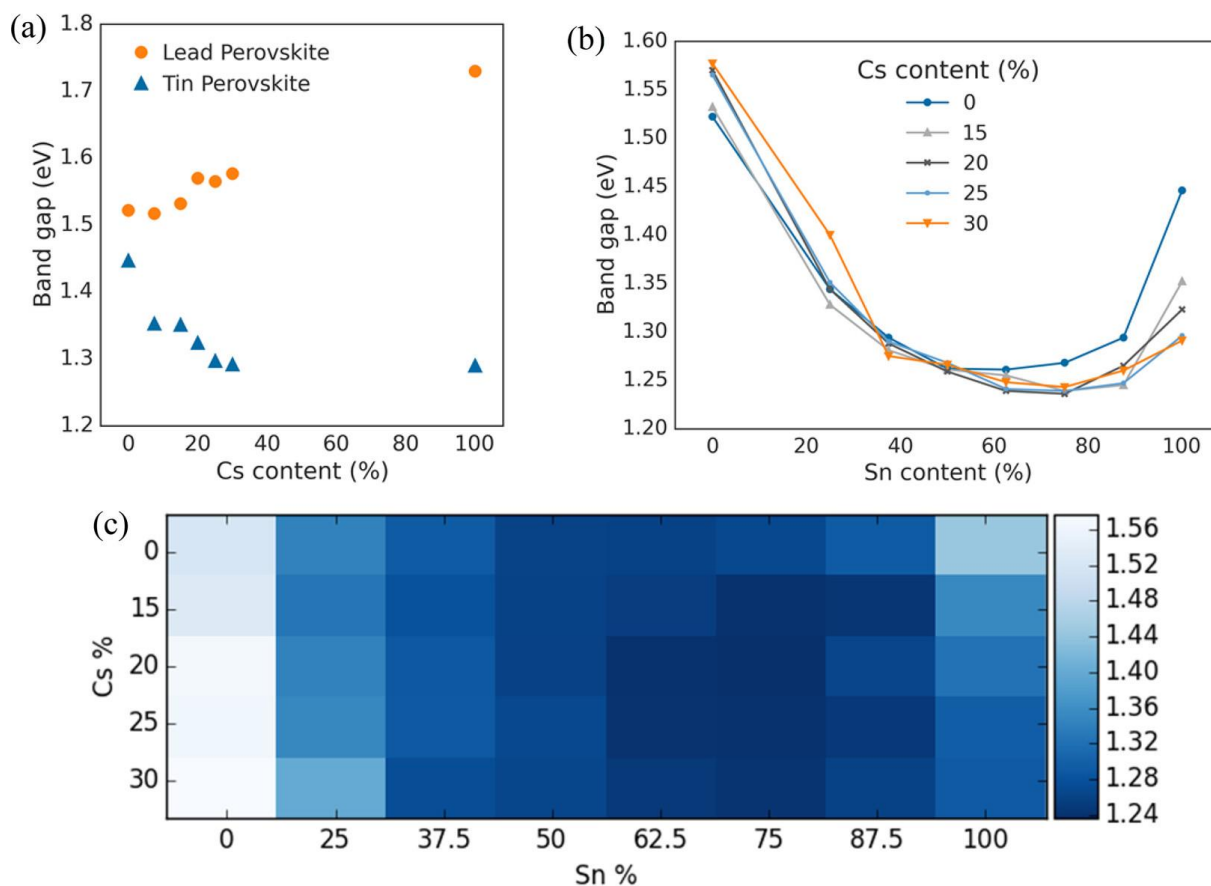


Figure 3. (a) Optical band gap of lead- and tin-based perovskites $\text{FA}_{1-x}\text{Cs}_x\text{MI}_3$ ($M = \text{Sn}, \text{Pb}$) as a function of cesium content. (b) Band gap of five series of tin-lead mixed perovskites, corresponding to cesium fractions of 0, 15, 20, 25, and 30%. (c) 2-dimensional map of band gap (in eV) across the formamidinium-cesium and tin-lead compositional space studied. Reproduced with permission.^[110] 2020, Journal of the American Chemical Society.

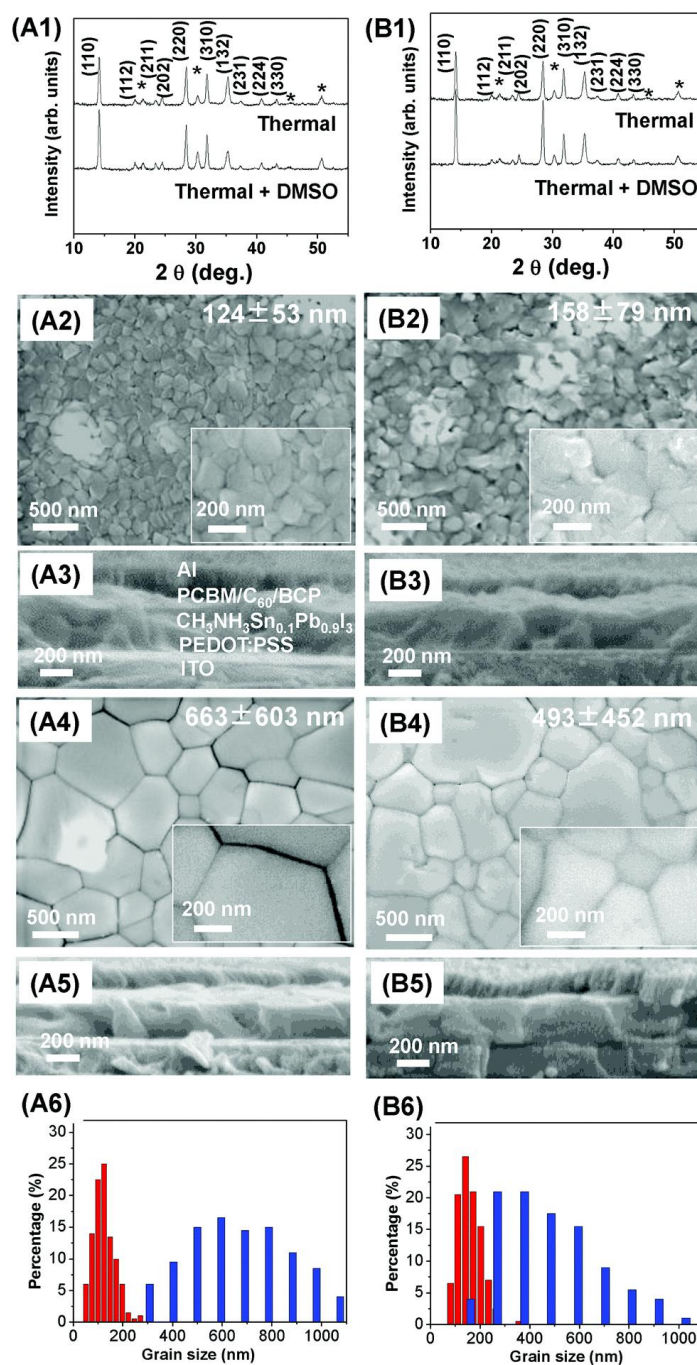


Figure 4. XRD patterns (A1 and B1), top-view (A2 and B2, A4 and B4) and cross-sectional view (A3 and B3, A5 and B5) SEM images, and grain size distribution (A6 and B6) of the $\text{CH}_3\text{NH}_3\text{Sn}_{0.1}\text{Pb}_{0.9}\text{I}_3$ (A) and $\text{CH}_3\text{NH}_3\text{Sn}_{0.25}\text{Pb}_{0.75}\text{I}_3$ (B) films after the only thermal annealing (A2, 3 and B2, 3) and thermal plus DMSO vapor-assisted thermal annealing (A4, 5 and B4, 5). (C) Schematics of possible role of DMSO during vapor-assisted annealing treatment. Reproduced with permission.^[121] 2020, Nanoscale.

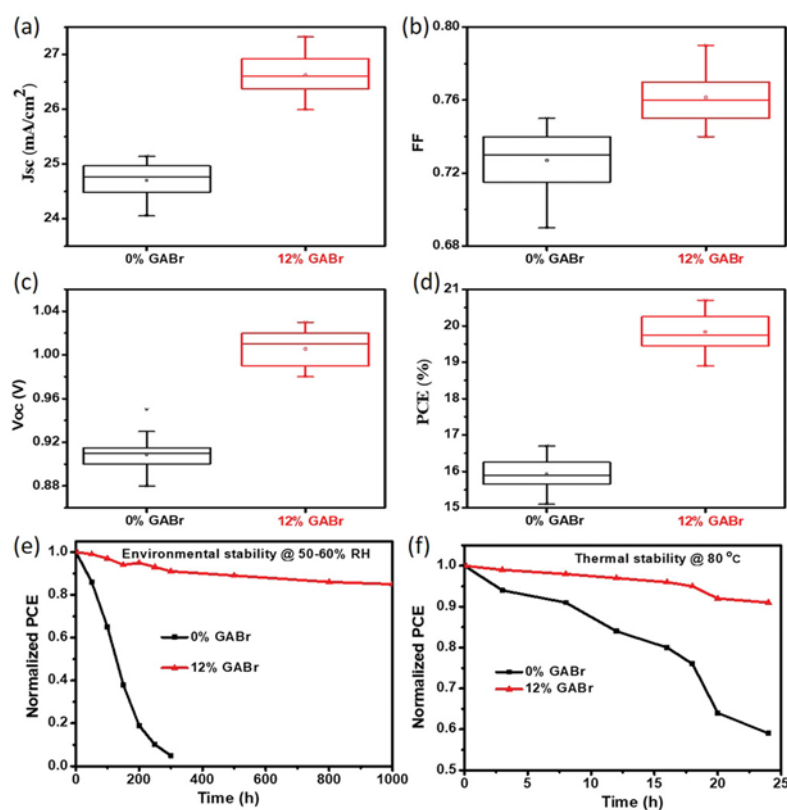


Figure 5. a–d) The photovoltaic parameters J_{sc} (a), FF (b), V_{oc} (c), and PCE (d) for 20 independent devices from the $FA_{0.7}MA_{0.3}Pb_{0.7}Sn_{0.3}I_3$ without and with GABr-based PSCs under forward voltage scan, respectively. e) The environmental and f) thermal stability test of the $FA_{0.7}MA_{0.3}Pb_{0.7}Sn_{0.3}I_3$ without and with 12% GABr-based PSCs without encapsulation. Note environmental stability was recorded at room temperature (50–60% humidity), and thermal stability was followed at 80 °C in air (50–60% humidity). Reproduced with permission.^[137] 2020, Advanced Materials.

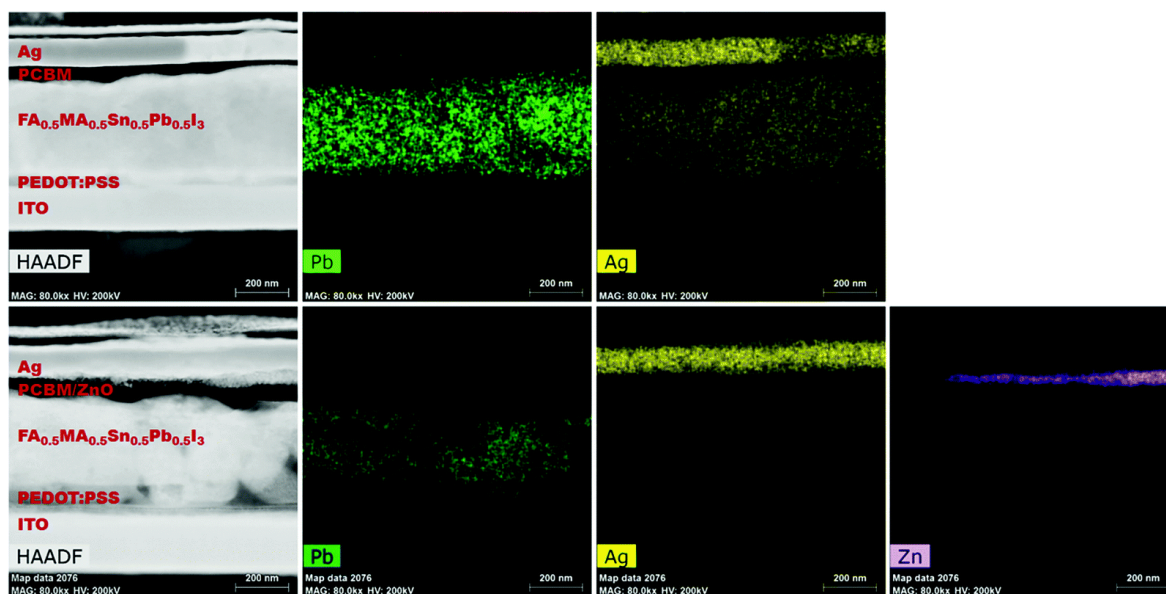


Figure 6. STEM images of the solar cells without (top) and with (bottom) ZnO and elemental distribution of Pb, Ag and Zn in the whole device, as measured using an EDS to illustrate the suppression of Ag diffusion within the perovskite film by the ZnO layer. Reproduced with permission.^[114] 2020, Journal of Materials Chemistry A.

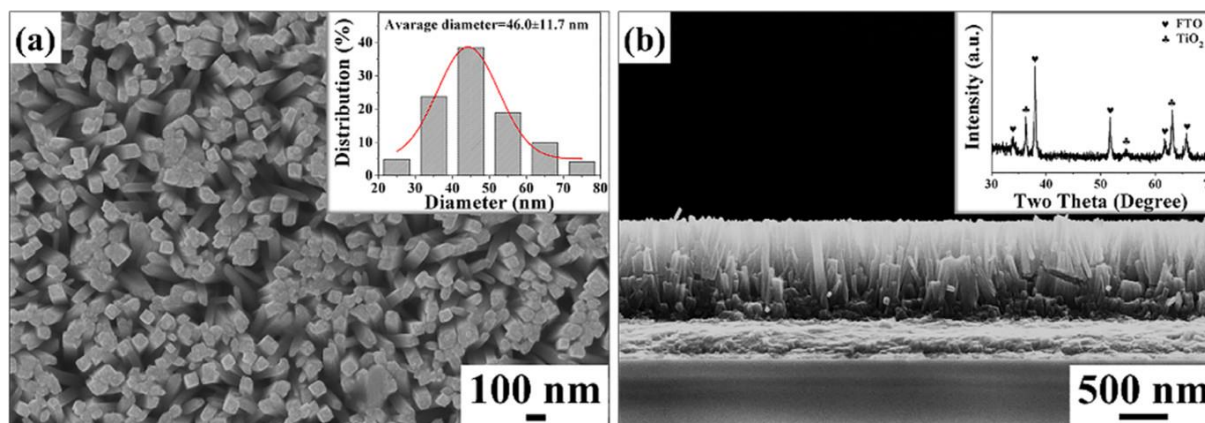


Figure 7. (a) Top-view and (b) cross-sectional SEM images of the optimal TNRAs. The inset images show the statistical distribution histogram of the diameter (a) and XRD pattern of the TNRAs (b). Reproduced with permission.^[161] 2020, ACS Applied Materials and Interfaces.

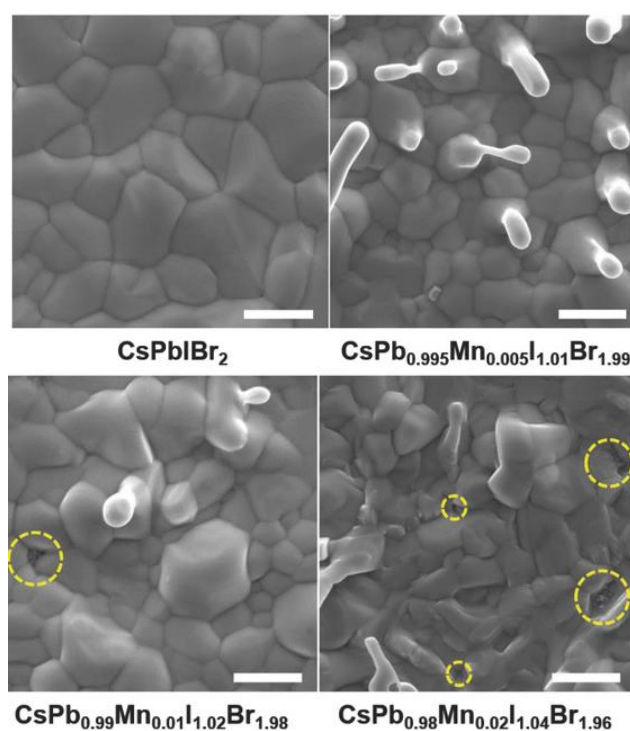


Figure 8. SEM images of CsPbIBr_2 and $\text{CsPb}_{1-x}\text{Mn}_x\text{I}_{1+2x}\text{Br}_{2-2x}$ ($x = 0.005, 0.01, \text{ and } 0.02$) films, respectively. All the scale bars are $1 \mu\text{m}$. The areas marked by yellow dash circles are pinholes. Reproduced with permission.^[177] 2020, Advanced Energy Materials.

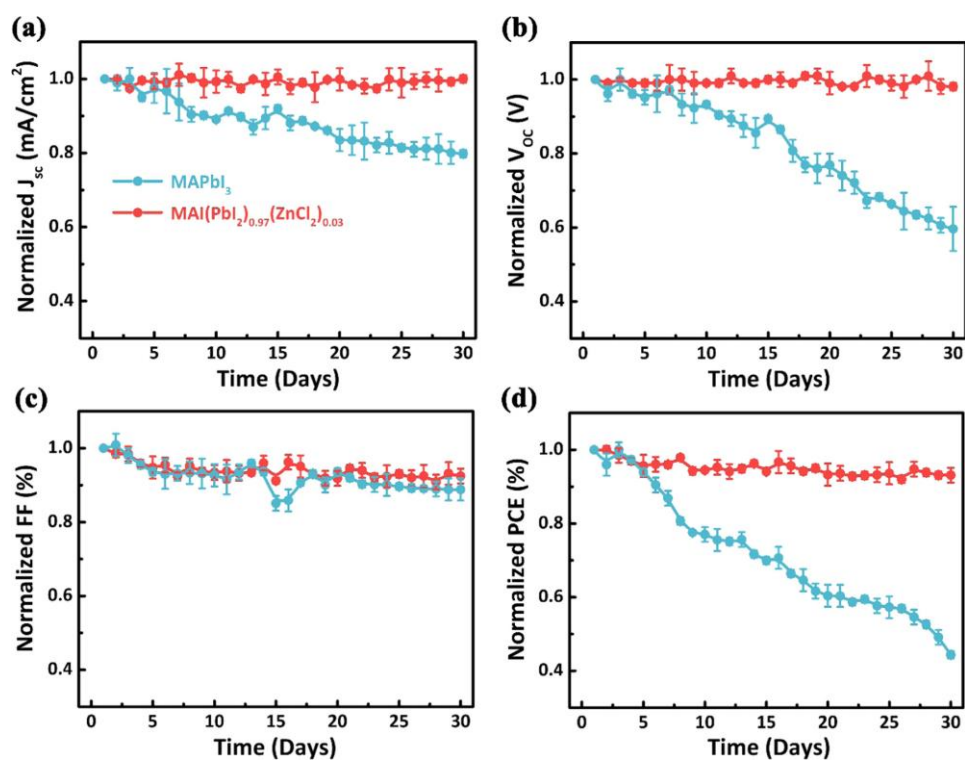


Figure 9. Normalized J_{sc} , V_{oc} , FF, and PCE for the MAPbI₃ and MAI(PbI₂)_{0.97}(ZnCl₂)_{0.03} PSCs stored in an ambient environment of 25–28°C with 30–55% humidity without any encapsulation. Reproduced with permission.^[178] 2020, ACS Applied Materials and Interfaces.

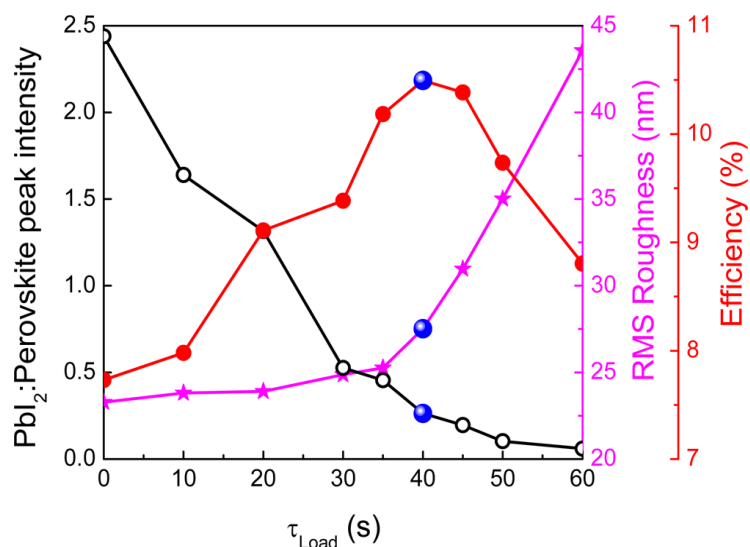


Figure 10. Optimization of τ_{load} on the basis of PbI₂ conversion and film roughness. The blue data points denote the values for optimized conversion and roughness. Solar cell efficiencies corresponding to each loading time are also included in the plot. Reproduced with permission.^[44] 2020, The Journal of Physical Chemistry C.

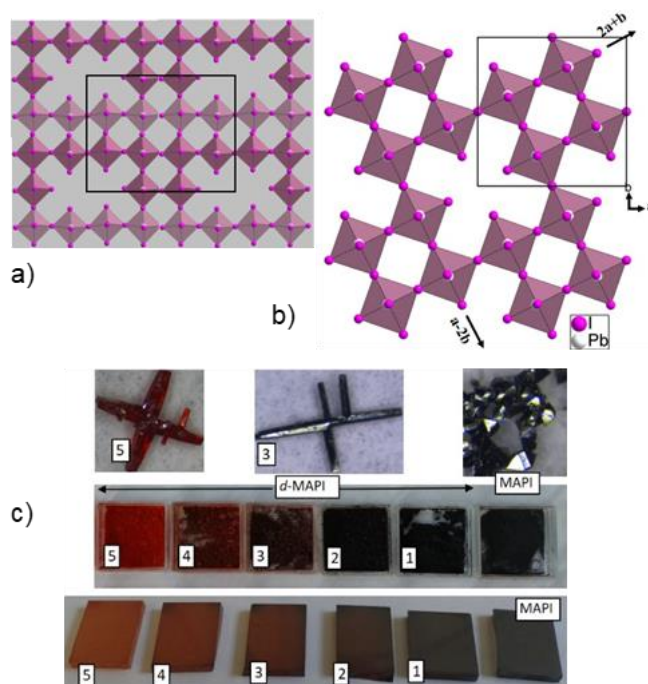


Figure 11. a) Hypothetical d-MAPI network $\text{Pb}_{10}\text{I}_{34}$ (or $\text{Pb}_{0.83}\text{I}_{2.83}$) consisting of $\langle 100 \rangle$ Pb_2I_7 layers connected together by PbI_6 octahedra. b) The deficient perovskite network obtained from the X-ray study of the prepared d-MAPI $(\text{MA})_{0.55}(\text{HEA})_{0.63}\text{Pb}_{0.82}\text{I}_{2.82}$ crystal (the small amounts of Pb^{2+} and Γ in $(0\ 0\ z)$ are not shown). c) Single crystals, powders, and thin films of $(\text{MA})_{1-2.48x}(\text{HEA})_{3.48x}[\text{Pb}_{1-x}\text{I}_{3-x}]$ ($x=0.10$ (1), 0.13 (2), 0.16 (3), 0.19 (4), and 0.20 (5)). Reproduced with permission.^[203] 2020, Angewandten Chemie.

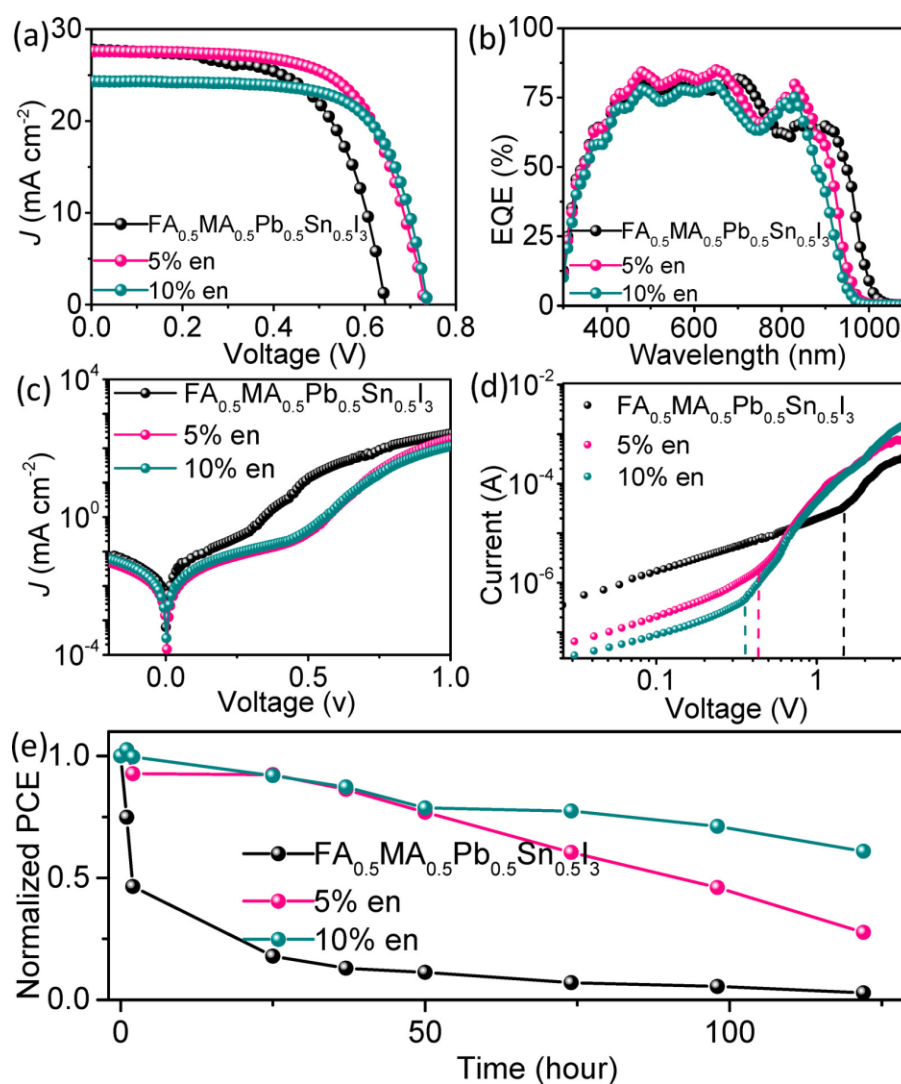


Figure 12. (a) J - V , (b) EQE, and (c) dark J - V curves of the representative solar cells using $\text{FA}_{0.5}\text{MA}_{0.5}\text{Pb}_{0.5}\text{Sn}_{0.5}\text{I}_3$, {5% en} $\text{FA}_{0.5}\text{MA}_{0.5}\text{Pb}_{0.5}\text{Sn}_{0.5}\text{I}_3$, and {10% en} $\text{FA}_{0.5}\text{MA}_{0.5}\text{Pb}_{0.5}\text{Sn}_{0.5}\text{I}_3$ absorbers. (d) Dark J - V curves of the hole-only devices using various absorbers. (e) Comparison of the stability of representative unencapsulated solar cells using various absorbers measured in ambient air with a 10–30% relative humidity at room temperature. The cells were stored in ambient air and in the dark. Reproduced with permission.^[207] 2020, Journal of the American Chemical Society.

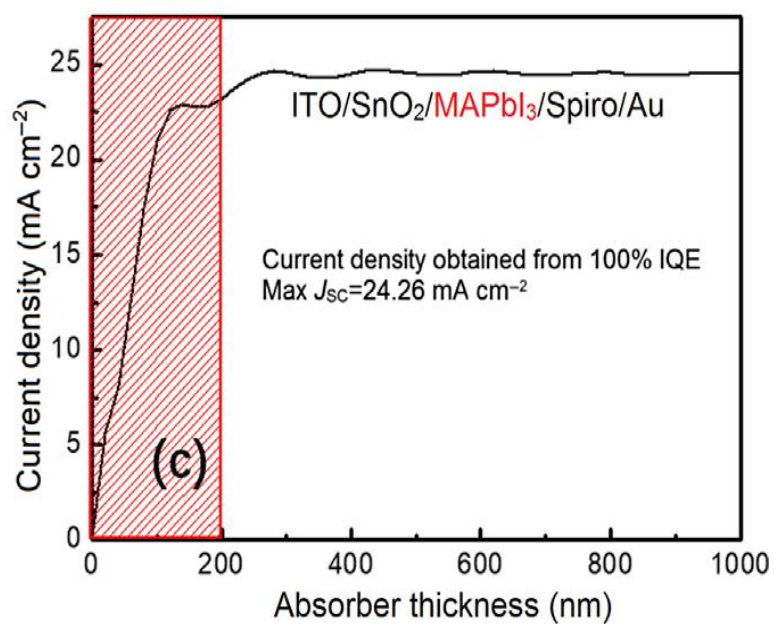


Figure 13. Calculated perovskite absorber thickness vs. short circuit current density. Reproduced with permission.^[208] 2020, Science Bulletin.

This article must be cited as:

L. Gollino, T. Pauporté, Lead-Less Halide Perovskite Solar Cells

Sol. RRL **2021**, *5*, 2000616 DOI: 10.1002/solr.202000616

WILEY-VCH



Thierry Pauporté

Prof. Thierry Pauporté is a director of research at the Centre National de la Recherche Scientifique (CNRS) in France and he works at Chimie-Paristech, PSL Université. He is graduated in Chemistry from the École Normale Supérieure de Lyon (ENS-L). He received his Ph.D. in physical chemistry from Montpellier II University, France, in 1995. His research interests include oxide and perovskite semiconductors, the functionalizing of the materials surfaces and he works on the integration of films and structures in efficient devices. The applications studied include perovskite solar cells, dye-sensitized solar cells, nanosensors, photodetectors, photocatalysis, wettability and fouling.



Liam Gollino

Liam Gollino is a PhD student under the supervision of Prof. Thierry Pauporté at the Centre National de la Recherche Scientifique (CNRS) in France and works at Chimie-Paristech, PSL Université. He is graduated in Physics and Chemistry from the École Nationale Supérieure de Chimie, Biologie et Physique (ENSCBP), France. Previously to his PhD, he studied organic solar cells at CEEC in Jena, Germany in the group of Prof. Harald HOPPE. He also worked on perovskite solar cells at INES in Le Bourget-du-Lac, France. His PhD research mainly focus on the development of a new family of lead-deficient perovskite solar cells.

Supporting Information

Lead-Less Halide Perovskite Solar Cells

Liam Gollino and Thierry Pauporté*

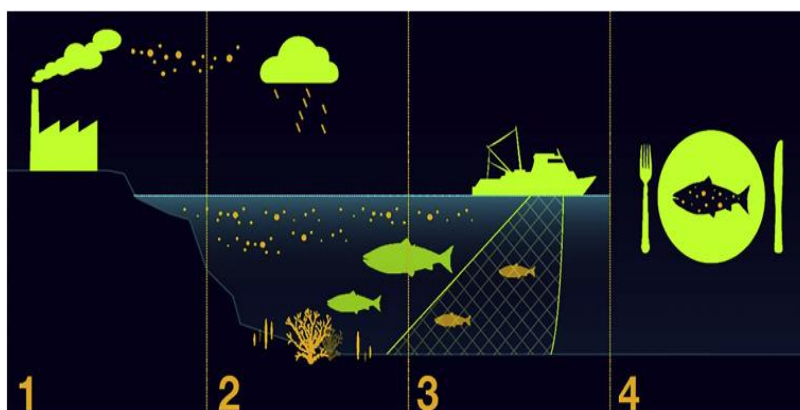


Figure S1. Heavy metals transfer chain in the environment (1) Industrial activities release metals in the environment. (2) Water transports metals into plants, consumed by small fishes. (3) Larger fishes consume small contaminated fishes. (4) Humans consume contaminated fishes. Heavy metals accumulate up the food chain; thus, more in top human than in any species lower down in the chain. Reproduced with permission.^[36] 2020, US Environmental Protection Agency.

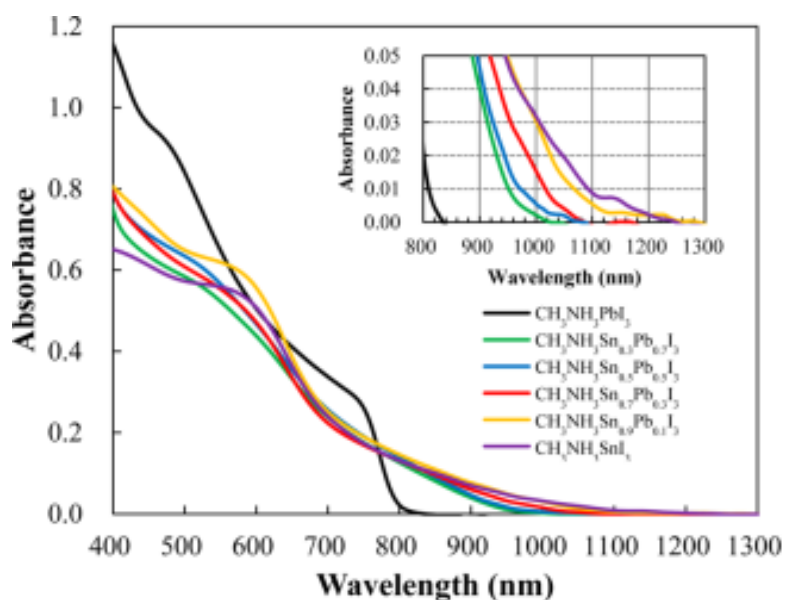


Figure S2. Electronic absorption spectra of $\text{MASn}_x\text{Pb}_{(1-x)}\text{I}_3$ perovskite. Reproduced with permission.^[106] 2020, The Journal of Physical Chemistry Letters.

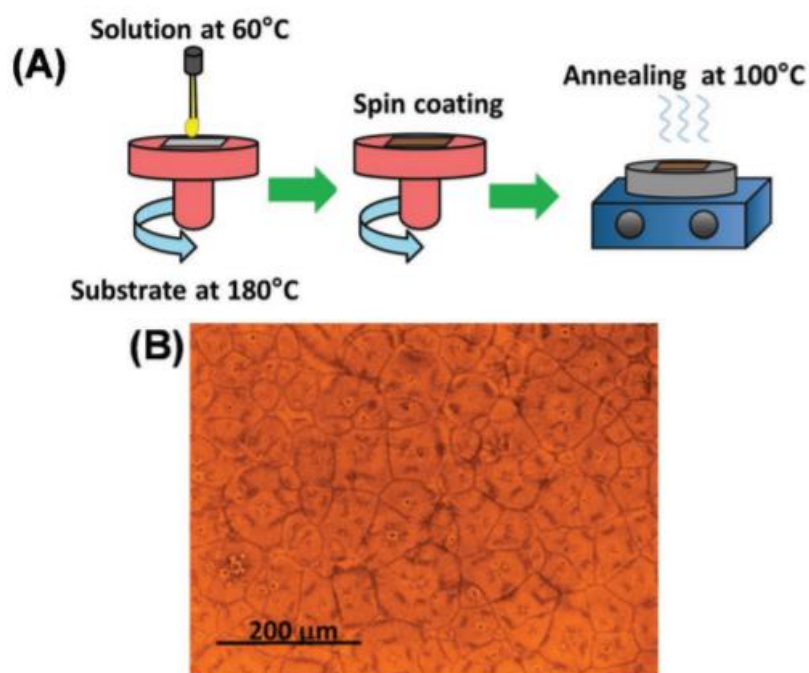


Figure S3. (a) Graphical representation of the one-step/hot casting method used to fabricate the $\text{MAPb}_{1-x}\text{Sn}_x$ perovskite layer and (b) the optical microscope image of the micron-sized grains obtained via this method. Reproduced with permission.^[115] 2020, *Advanced Materials*.

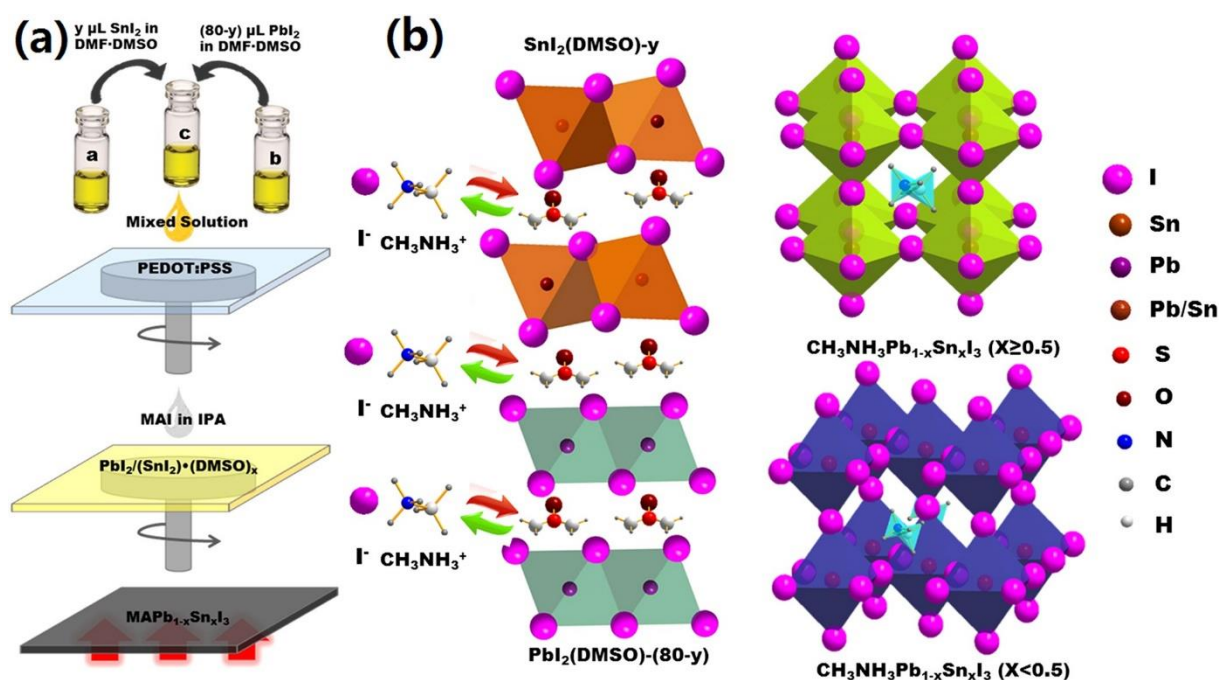


Figure S4. (a) Schematic of prepared process of $\text{CH}_3\text{NH}_3\text{Pb}_{(1-x)}\text{Sn}_x\text{I}_3$ ($0 \leq x \leq 1$) thin films; (b) Schematic of formation mechanism in $\text{CH}_3\text{NH}_3\text{Pb}_{(1-x)}\text{Sn}_x\text{I}_3$ ($0 \leq x \leq 1$) thin films and the corresponding crystal structure. Reproduced with permission.^[117] 2020, *Scientific Reports*.

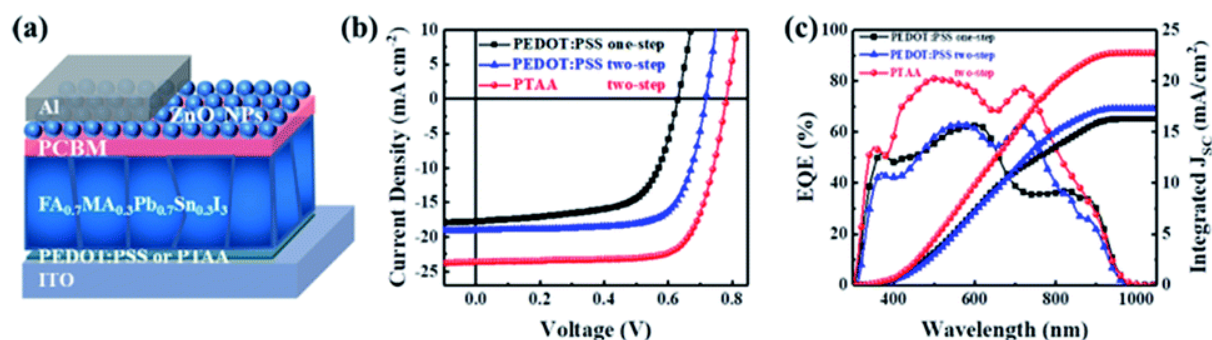


Figure S5. The structure (a), J–V characteristics (b) and EQE curves (c) of the best devices based on perovskite films processed via various methods on different substrates. Reproduced with permission.^[120] 2020, Journal of Materials Chemistry A.

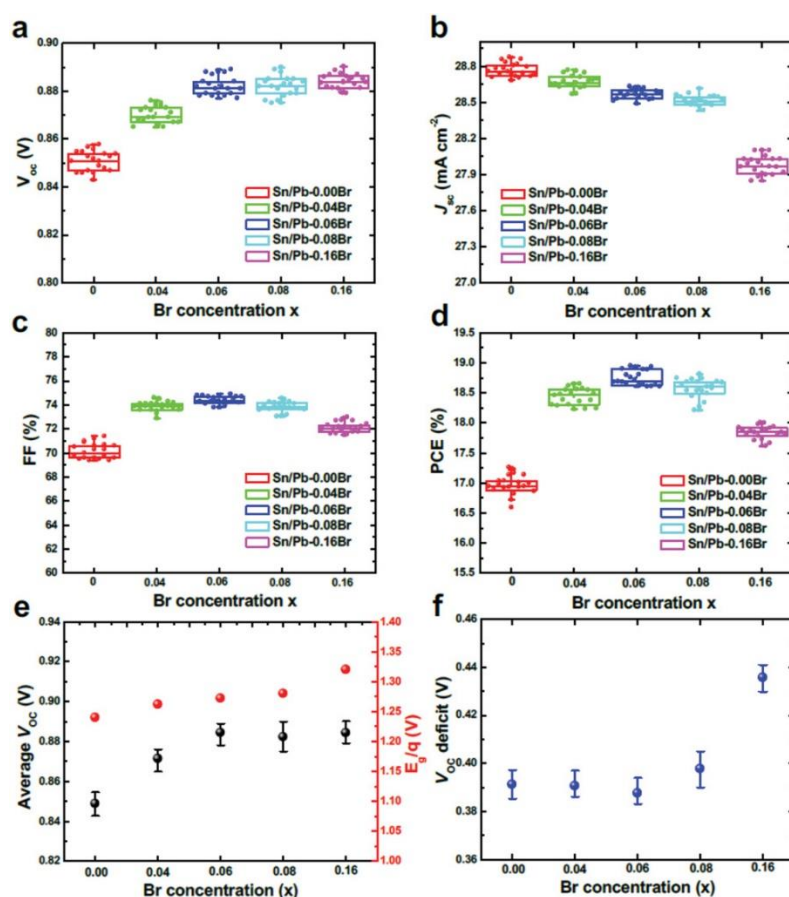


Figure S6. Statistics of all main photovoltaic parameters of Sn/Pb-xBr PSCs with x varying from 0 to 0.16 under a $100 \text{ mW}\cdot\text{cm}^{-2}$ AM1.5G solar irradiation under forward voltage scan: a) V_{oc} , b) J_{sc} , c) FF, and d) PCE. 15–20 devices for Br concentration were fabricated and measured. e) Average V_{oc} versus Br concentration and E_g/q versus Br concentration. f) calculated V_{oc} deficit versus Br concentration. Reproduced with permission.^[128] 2020, Advanced Energy Materials.

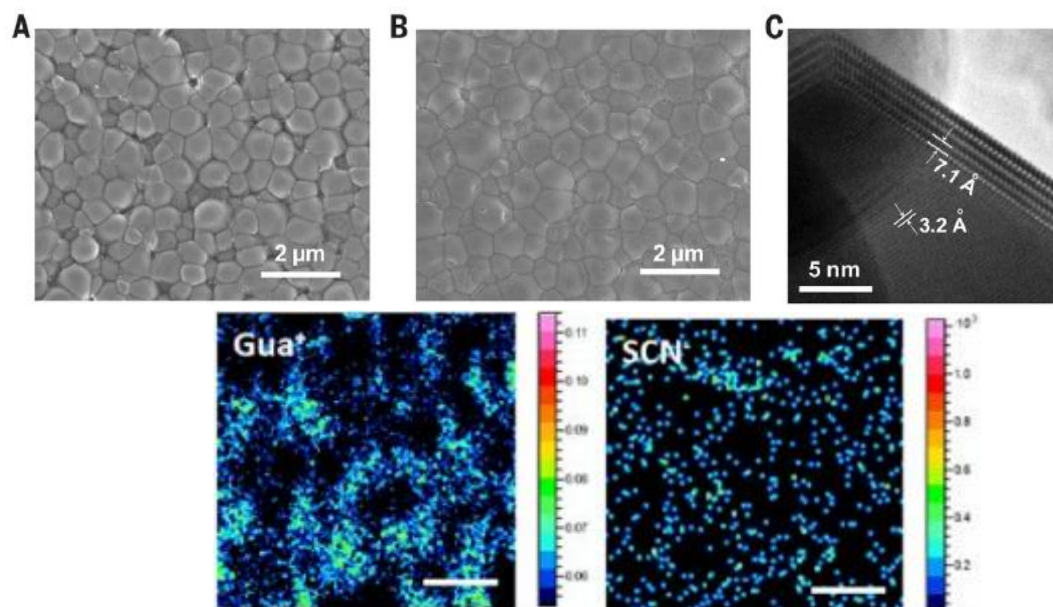


Figure S7. SEM images of perovskite films prepared (A) without and (B) with 7% GuaSCN additive. (C) HRTEM image of the grain boundary region of perovskite prepared with 7% GuaSCN additive. TOF-SIMS 2D images of element distribution: Pb, I, Gua, and SCN. The scale bar is 2 μm . Note the Gua and SCN signals were collected in different measurements as a different SIMS polarity was required to image each species. Reproduced with permission.^[136] 2020, Science.

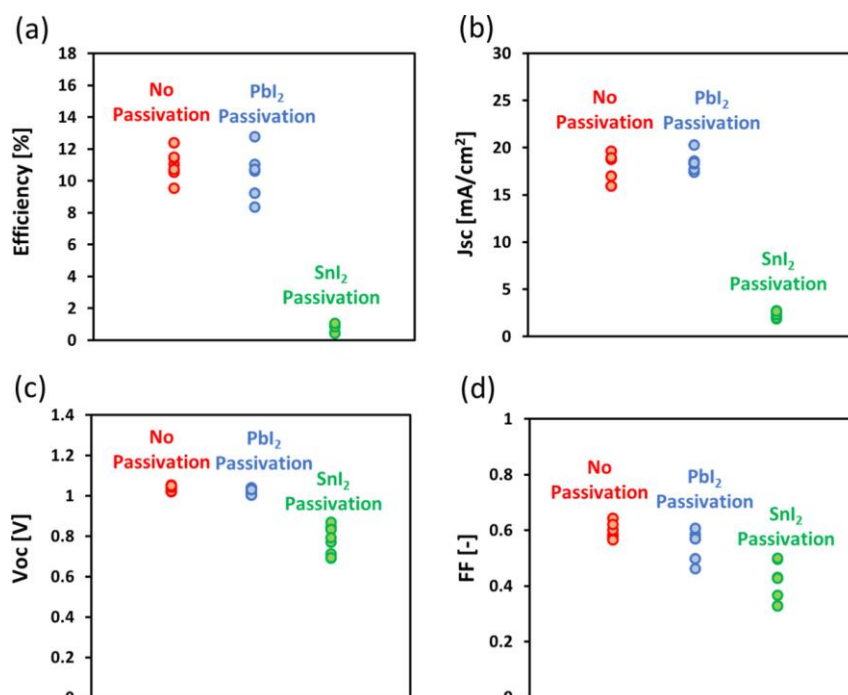


Figure S8. Photovoltaic performance distribution of PSCs with and without a passivation layer (a) power conversion efficiency, (b) J_{sc} , (c) V_{oc} , and (d) FF. Reproduced with permission.^[153] 2020, ACS Applied Materials & Interfaces.

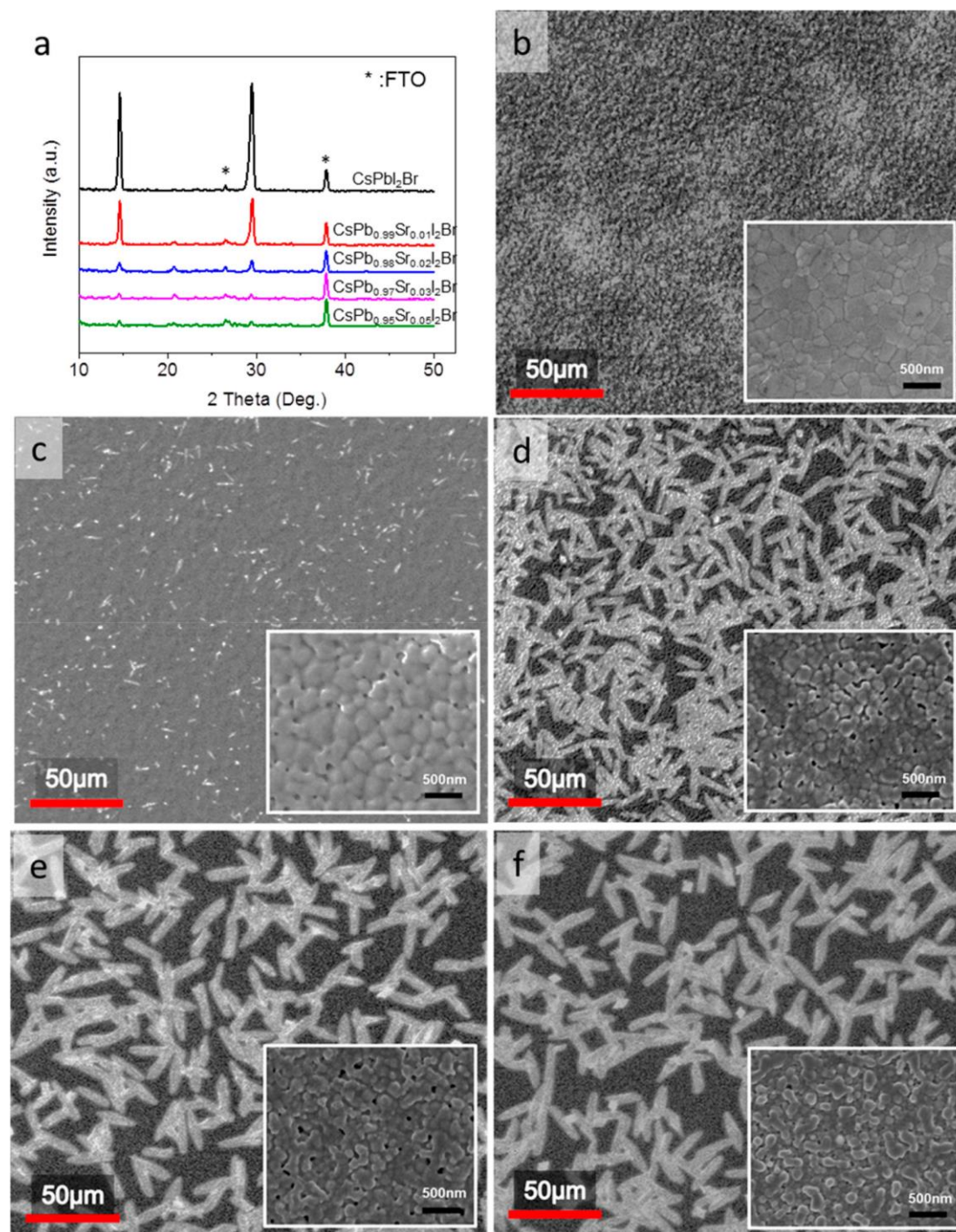


Figure S9. (a) XRD patterns of low-temperature-processed $\text{CsPb}_{1-x}\text{Sr}_x\text{I}_2\text{Br}$ films. SEM images of (b) CsPbI_2Br , (c) $\text{CsPb}_{0.99}\text{Sr}_{0.01}\text{I}_2\text{Br}$, (d) $\text{CsPb}_{0.98}\text{Sr}_{0.02}\text{I}_2\text{Br}$, (e) $\text{CsPb}_{0.97}\text{Sr}_{0.03}\text{I}_2\text{Br}$, and (f) $\text{CsPb}_{0.95}\text{Sr}_{0.05}\text{I}_2\text{Br}$. The inset SEM images are taken in the darker region. Reproduced with permission.^[157] 2020, ACS Energy Letters.

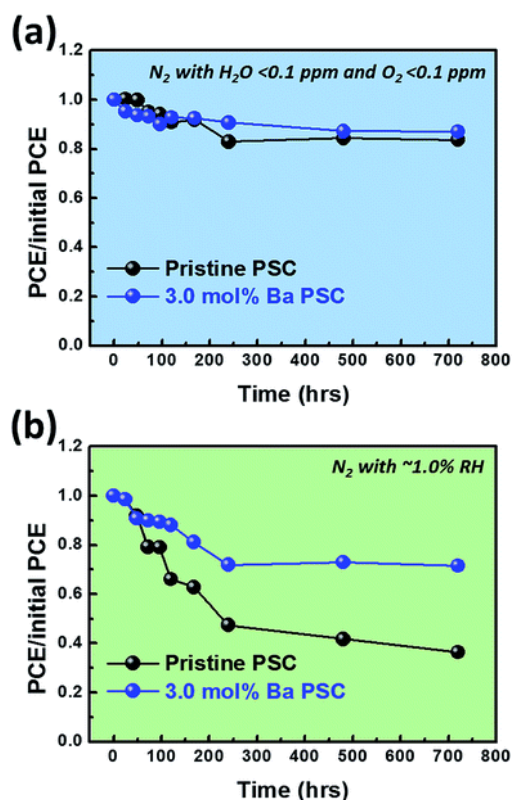


Figure S10. The stability of PSCs with pristine and 3.0 mol% Ba²⁺-doped perovskite films when stored in (a) the glovebox system with the integrated gas purification system and (b) the glovebox system without the integrated gas purification system. Reproduced with permission.^[168] 2020, Journal of Materials Chemistry A.

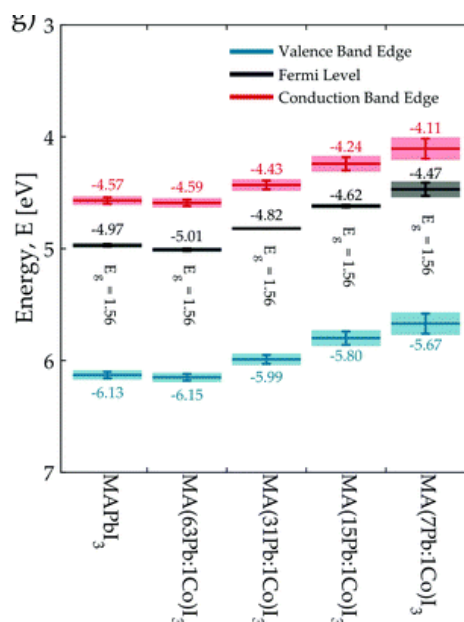


Figure S11. Energy levels of the MA(Pb:Co)I₃ materials relative to the vacuum level. The Fermi and valence band edge (VBE) energies were determined directly from ultraviolet photoelectron spectroscopy and the conduction band edge (CBE) energies were inferred using the band gap values determined from the edge of the external quantum efficiency (EQE) spectra. Reproduced with permission.^[175] 2020, Energy & Environmental Science.

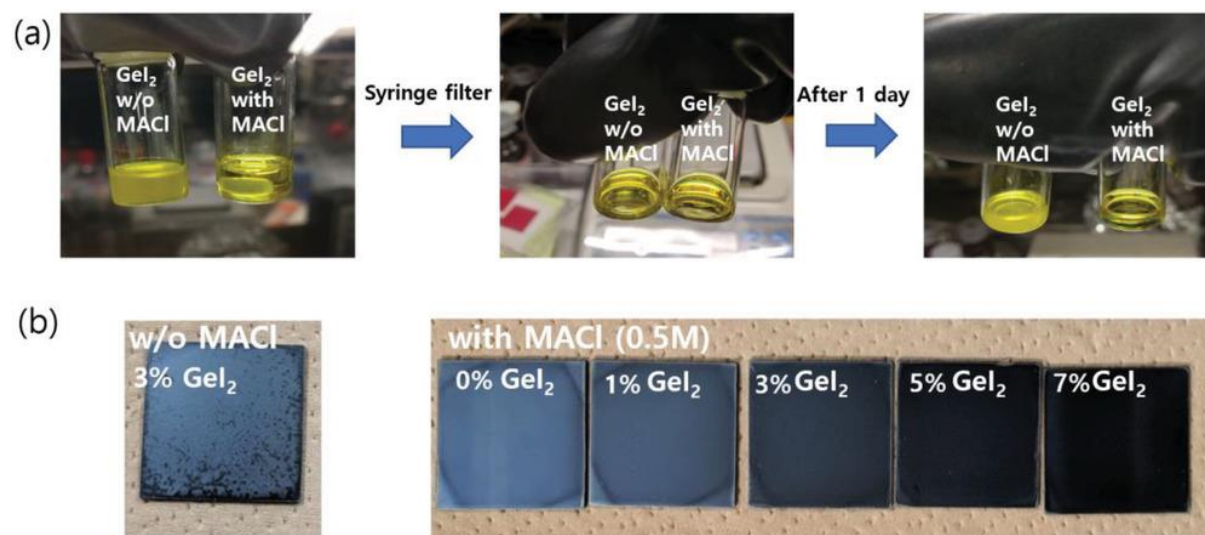


Figure S12. a) GeI₂-containing DMF/DMSO organic-inorganic perovskite (3% GeI₂, FA_{0.83}MA_{0.17}Pb_{0.97}Ge_{0.03}(I_{0.9}Br_{0.1})₃) inks with and without MACI (0.5M). b) The photographs of MACI-contained or non-contained perovskite films of FA_{0.83}MA_{0.17}Ge_xPb_{1-x}(I_{0.9}Br_{0.1})₃ with various concentration of GeI₂ ($x = 0-0.07$). Reproduced with permission.^[187] 2020, Advanced Energy Materials.

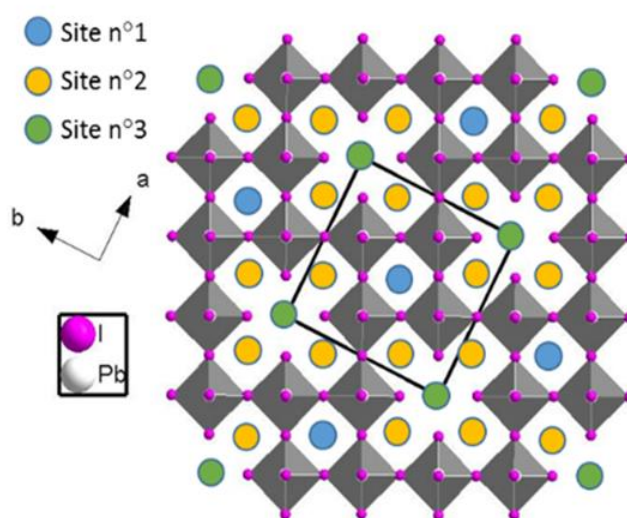


Figure S13. View along the *c* axis of the tetragonal unit cell (black square) of a hypothetical structure of d- α -FAPI with $x = 0.20$ (resulting formula of (HEA or TEA, FA)_{1.2}[Pb_{0.8}I_{2.8}]). The organic cations are located on the three different crystallographic sites n°1, n°2, and n°3 (blue, yellow, and green circles, respectively). Reproduced with permission.^[202] 2020, ACS Applied Materials & Interfaces.

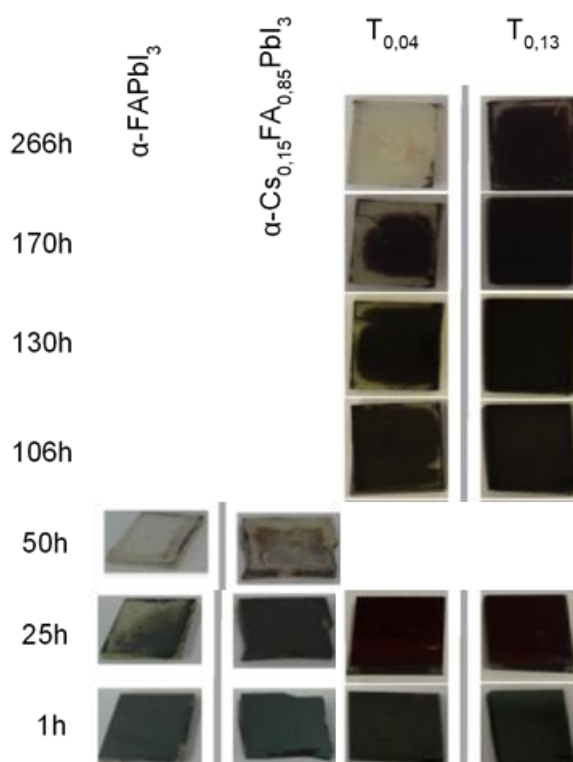


Figure S14. Stability test (ambient conditions: 25 °C, 75–90% RH) of α -FAPbI₃, α -Cs_{0.15}FA_{0.85}PbI₃, T_{0.04}, and T_{0.13} thin films. The XRD patterns and the pictures were realized in the 1–50 h and 1–266 h ranges for α -FAPbI₃, α -Cs_{0.15}FA_{0.85}PbI₃ and T_{0.04}, T_{0.13}, respectively. Reproduced with permission.^[202] 2020, ACS Applied Energy & Materials.

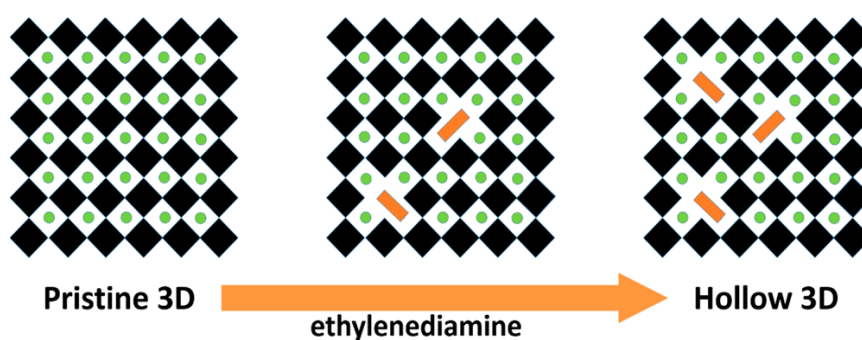
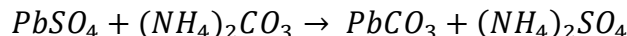


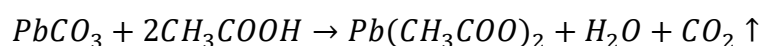
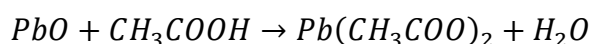
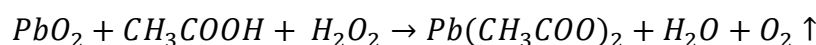
Figure S15. Schematic illustration of the structure of the 3D pristine MAPbI₃ perovskite and its transformation from a dense proper perovskite structure to a hollow 3D structure with increasing amount of en. Black cubes: [PbI₆] octahedra, green spheres: MA cations, orange rectangles: ethylenediammonium (en) cations. Reproduced with permission.^[206] 2020, Journal of the American Chemical Society.

A. Recycling of lead in PSCs.

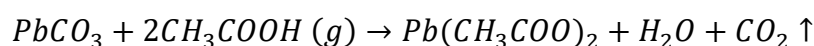
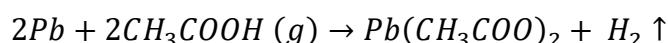
One of the first report was in 2014, in which Chen and co-workers reported the use of PbI_2 recycled from car batteries to make PSCs with an efficiency close to the ones using commercial PbI_2 [223]. This year, a study reporting the use of lead acetate ($Pb(Ac)_2$) recovered from lead-acid batteries to fabricate efficient PSCs was published in 2020 by Li et al. [224]. During the charging/discharging process of a lead-acid battery, concentrated sulfuric acid provides the exchange ions. This acid leads to the formation of lead sulphate ($PbSO_4$) in lead mud. At the end of the process, Pb and $PbSO_4$ are found at the anode material and PbO_2 and $PbSO_4$ at the cathode material. The authors recycled these materials to produce lead acetate. The recycling process is shown in Figure S16. First, $(NH_4)_2CO_3$ was used to recover lead from $PbSO_4$ according to the equation:



Once this done, the materials obtained with the cathode product were calcined & the resulting products were added in a saturated solution of CH_3COOH and H_2O_2 to obtain $Pb(Ac)_2$ according to the reaction equations:



For the anode, products reacted with CH_3COOH steam to form $Pb(Ac)_2$. The corresponding equations are:



Lead acetate once recovered, it was mixed with MAI to form the precursor solution and fabricate FTO/PEDOT:PSS/MAPbIBr/PCBM/TIPD/Al PSCs. Different $\text{Pb}(\text{Ac})_2$ were used to form perovskite films: commercial one, recovered from anode and from cathode. The highest efficiency was reached by devices based on cathode-recycled lead acetate with a value of 17.86% mainly due to bigger perovskite grains. As a comparison, commercial lead acetate lead to a PCE of 15.69% while anode-recycled $\text{Pb}(\text{Ac})_2$ reached a PCE of 14.72%. This study is interesting regarding the dependence of research groups on companies producing extremely pure chemical compounds as it shows a way out of this dependency. Furthermore, being able to fabricate high-efficiency PSCs with recycled lead is extremely promising for an even more green energy source. It is easy to imagine PSCs fabricated with lead recycled from other PSCs, driving this technology to a path where lead will no longer be an issue. Based on this thought, different groups published articles on the recycle of lead within PSCs ^[225,226]. In 2019, Chhillar et al. developed different methods to recycle the degraded perovskite film ^[227]. Their goal was to recycle directly the degraded film onto the substrate to re-use directly in devices. To do so, they tested a single-step method with acetate or chloride and a sequential deposition route. The chloride method was found to deteriorate badly the film, forming a recovered film without the same optoelectronic properties as the original film. The sequential route enhanced too much the crystallization of PbI_2 , making impossible the formation of MAPbI_3 . The acetate technique, on the opposite allowed the formation of a perovskite film with quite similar optoelectronic properties despite a decreased absorbance. However, an interesting increased PL signal with a slight blue-shift was observed. The films obtained with each recycling method were not tested in devices but the results for the single-step acetate method is encouraging for in-situ recycle of lead in PSCs.

This article must be cited as:

L. Gollino, T. Pauporté, Lead-Less Halide Perovskite Solar Cells
Sol. RRL **2021**, *5*, 2000616 DOI: 10.1002/solr.202000616

WILEY-VCH



Figure S16. Schematic diagram of lead recovery from a lead-acid battery. Reproduced with permission ^[224]. 2020, Journal of the American Chemical Society.